POROUS ALUMINA CERAMICS IN DRUG DELIVERY: PROCESSING CONCERNS AND PERCOLATION MODELS

by

SCOTT RUGGLES ELLIS

A thesis submitted in partial fulfillment of the

requirements for the degree of

Doctor of Philosophy

(Pharmacy)

at the

UNIVERSITY OF WISCONSIN - MADISON

1990

Pharm
AW
ELSS

POROUS ALUMINA CERAMICS IN DRUG DELIVERY: PROCESSING CONCERNS AND PERCOLATION MODELS

Scott Ruggles Ellis
Under the supervison of Professor George Zografi
at the University of Wisconsin - Madison

ABSTRACT

Aluminum oxide (Al_2O_3), a widely-used ceramic biomaterial, was investigated as a potential material for use in fabricating porous devices for control of drug release. Morphological and transport properties of porous Al_2O_3 disks were characterized by the statistical modeling technique of percolation theory.

Processing studies were performed to determine the variables controlling the final porosities of sintered disks. Disks were fabricated using monodisperse and polydisperse Al_2O_3 powders and fired at various times and temperatures. The polydispersity of the ceramic powder had the greatest influence on the total volume shrinkage and final porosity of a disk. Final porosity was higher, and shrinkage was lower, if the polydisperse powder was used. The temperature (above 1450°C) at which a polydisperse disk was sintered was found to have the greatest influence on its final porosity.

Percolation theory models were successfully used to obtain the critical percolation threshold ($\emptyset_c$) for a group of ceramic disks of increasing total porosities. The volume fraction accessible of the total pore structure ($\emptyset^A$) and volume fraction effective for transport of benzoic acid through a disk ($\emptyset^E$) were experimentally determined and used to estimate $\emptyset_c$. Values of $\emptyset_c$ were 0.129 ± 0.00 from $\emptyset^A$ fit, and 0.169 ± 0.02 from $\emptyset^E$ fit, indicating that diffusion through the pores of a disk did not utilize the entire accessible pore

structure. The pore structure available for diffusion followed the tetrakaidecahedral lattice approximation (coordination number = 14). Disks made with artificially large pores exhibited finite-size scaling behavior in the experimental volume fraction effective near $\emptyset_c$.

George Zografi

Professor George Zografi, Major Professor

DEDICATION

To my parents.

ACKNOWLEDGEMENTS

This research was partially funded by a two-year Advanced Predoctoral Fellowship awarded by the Pharmaceutical Manufacturer's Association Foundation, Washington, DC, from January 1988 to December 1989.

I would like to thank Dr. James Wright for helping me to undertake and complete this work in an area that was new to both myself and the field of Pharmaceutics.

Finally, I would like to thank Professor George Zografi for his understanding and patience in guiding me through the last year-and-a-half of my graduate school work.

TABLE OF CONTENTS

LIST OF FIGURES

LIST OF TABLES

LIST OF PERCOLATION THEORY SYMBOLS

Symbol	Meaning	Page
$P(x)$	Probability of a site or bond x being present in a lattice	23
z	Coordination number of a unit cell of a lattice	25
$R(x)$	Radius of cluster x below the percolation threshold	25
$\emptyset_c$	Critical percolation threshold	27
$\emptyset$	Total dimensional porosity (total void space)	30
m	Universal exponent (= 1.4 in three dimensions)	30
ξ	Correlation length	31
ν	Correlation length exponent (= 0.9 in three dimensions)	31
$\emptyset^A$	Accessible volume fraction	31
β	Accessible lattice exponent (= 0.4 in three dimensions)	31
$\emptyset^I$	Isolated volume fraction	32
$\emptyset^B$	Backbone volume fraction	32
$\emptyset^D$	Dead-end volume fraction	32
γ_B	Backbone lattice exponent (= 0.9 in three dimensions)	32
$\emptyset^E$	Effective volume fraction for transport	34
μ	Effective conductivity exponent (= 2.0 in three dimensions)	34
D_B	Bulk diffusivity	35
D_{aq}	Aqueous diffusivity	35
L	Linear system thickness for transport	35
t	Time	35
$\emptyset^S$	Surface volume fraction	38
Σ	Effective electrical conductivity	41
σ	Volume fraction conductor (analogous to $\emptyset$)	41
δ	Ratio of $\emptyset^S$ to $\emptyset^I$	148

I. INTRODUCTION

A. Objective and Scheme of the Research

The intent of the work described in this thesis was to demonstrate the usefulness of porous ceramic devices made from aluminum oxide (alumina, or Al_2O_3) as implantable sustained release carriers for drugs of small molecular dimension. To this end, two important concerns regarding the properties of these devices were addressed: 1. That they could be reproducibly manufactured to achieve certain desired porosities; and 2. that a simple modeling technique, percolation theory, could be utilized to describe their microstructures and release characteristics. These two subjects constituted the bulk of the research to be summarized here.

The structure of this Introduction may be summarized as follows. First, those portions of the broad field of ceramic materials needed to understand the procedures used in the manufacture of porous alumina devices will be discussed, and some pertinent properties of the alumina matrix germane to later topics will be given. Next, the percolation theory method used to model the properties of the devices will be discussed in detail. A review of issues important to the use of ceramic materials in the physiological environment will then be presented, as will some intended applications of alumina drug delivery devices.

B. Ceramic Materials

1. DEFINITION

A ceramic is commonly defined as any nonmetallic ionic material composed primarily of inorganic constituents[1]. Examples of ceramics include aluminum oxide, magnesium oxide (MgO), silicon dioxide (SiO_2), and silicon carbide (SiC). These primary ceramic compounds may be combined in different proportions to form a variety of materials such as

porcelains, clays, and cements.

Each ceramic material possesses a unique microstructure that depends on the atomic composition of the material and how it was processed. This microstructure will be discussed next, and its dependence on processing considered afterward.

2. THE CERAMIC MICROSTRUCTURE

a) Crystal Structures

The microstructure of a polycrystalline ceramic material consists of discrete regions of solid, that can be interlaced by a random network of voids, or pores. The solid may be either crystalline or amorphous (glassy) in structure. All ceramic materials can assume crystalline structures, but some (such as SiO_2) may be forced into a glassy state under certain conditions. Since Al_2O_3 does not form a glass, this state will not be considered here.

The fundamental building block of a crystal is the unit cell[2], which is the smallest structure that contains all spatial and compositional information regarding the three-dimensional arrangement of the atoms making up the crystal (in the same manner as a monomeric unit of a polymer chain describes a polymer). The structure of this unit cell depends on the packing abilities of its constituent atoms, which in turn depend on such atomic properties as the coordination number of the cation and the radii of the constituent ions. Unit cells are commonly either cubic or hexagonal, although other shapes are possible. Names have been assigned to most unit cell structures, such as the body-centered cubic (BCC) and hexagonal close-packed (HCP) cells shown in Figures 1.1(a) and 1.1(b)[3]. A crystal may be constructed by three-dimensional stacking of copies of its unit cell.

The stability of the crystal lattice (the network of atomic bonds in the structure) reflects

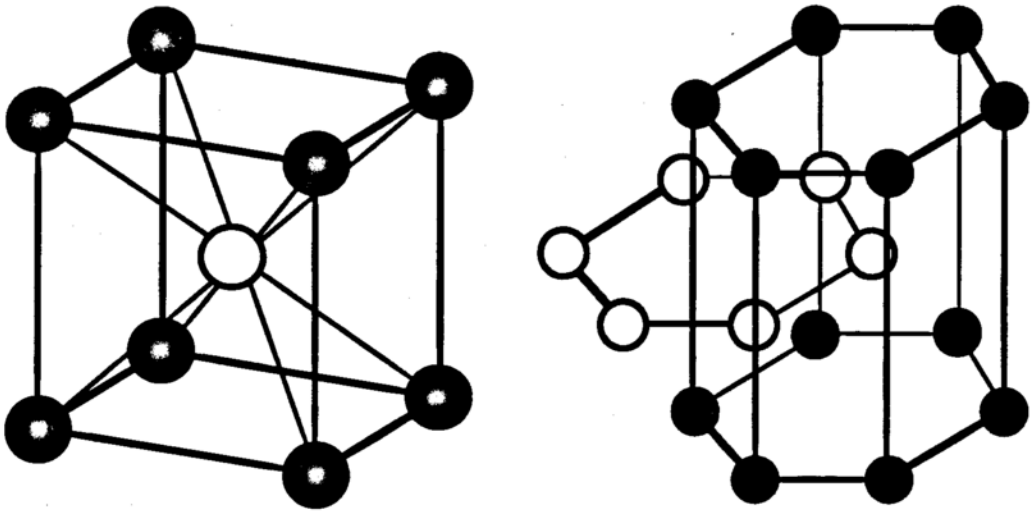

(a) (b)

Figure 1.1. (a) Body-centered cubic, (b) Hexagonal close-packed unit cells.

the number of defects it contains, where a defect is defined as an irregularity that exists within or at the boundary of the single crystal. Crystals will contain an equilibrium number of defects due to entropy effects. A defect may be classified as point, line, plane, or bulk[4], depending on its extent and nature. Point and line defects have dimensions on the atomic scale, and are difficult to observe directly. Impurities and vacancies are considered to be point defects; for example, substitution or removal of a lattice atom can disrupt the packing arrangement in the vicinity of that atom. Point defects are thermodynamic in nature, since their occurrence depends on such quantities as the solubility of an impurity in the lattice (for instance, the solubility of potassium ions in a sodium chloride lattice).

Dislocations, or mismatches between groups of atoms within the crystal, are mechanical line defects that extend a relatively short distance into the structure. A dislocation originates at a plane or a bulk defect. Point and line defects have the ability to migrate toward each other or toward plane or bulk defects. For example, coalescence of vacancies may result in the formation of very small inclusions, or micropores, within the lattice. Migration of dislocations within a crystal results in the formation of additional plane defects, which will be considered next.

b) Grains and Voids

A single crystal in a larger overall structure is called a grain. Crystals with different orientations border on each other at the plane defects known as grain boundaries. Grain boundaries may result from the coalescence of so many dislocations and vacancies in a region within a crystal that the crystal splits into two grains, one with the original crystal orientation and one with a slightly altered orientation. The grain boundary between two crystals possesses an interfacial free energy, γ, which is less than the surface free energy of an exposed crystal face[5]. This boundary energy is what binds the ceramic together.

The boundaries of a grain may be either straight, concave, or convex[6] with respect to the grain center. Hexagonal grains have straight sides, while grains with fewer than six sides are convex and grains with more than six sides are concave. Different grains have different free energies, as determined by their boundaries; thus, the potential exists for grains to grow or shrink in response to free energy gradients between them. An analogy is often drawn between this structure and the structure of bubbles in a soap film.

The potential for migration of atoms across a grain boundary is given by[7]:

$$\Delta G = \gamma V_m \left(\frac{1}{r_1} + \frac{1}{r_2}\right) ; \qquad (1.1)$$

where ΔG is the free energy to be gained or lost in movement across the boundary, γ is the interfacial energy (assumed to be independent of r_1 and r_2), V_m is the molar volume of the grain, and r_1 and r_2 are the radii of curvature of the boundary. (Note that r_1 and r_2 may be either positive or negative.) Jumping of molecules from a smaller (convex) grain to a larger (concave) one gives the boundary between them the appearance of movement toward the center of the smaller grain; hence, this process is often termed grain boundary migration. During this process, large grains will grow to be even larger, while small grains will shrink and may even disappear entirely. Elimination of micropores can result during this process.

While equation (1.1) governs interaction between two grains, the rate of atom jumping between them depends on temperature and follows a typical Arrhenius relationship as given by[8]:

$$U = U_0 \exp\left(-\frac{\Delta G_U}{R T}\right) ; \qquad (1.2)$$

where U represents the ability of an atom to jump across the boundary, ΔG_U is the free

energy of activation of this jump, U_0 is a pre-exponential factor, and T is the temperature. The activation energy required to cause significant jumping of atoms across a grain boundary in a ceramic is very large, so high temperatures must be used to initiate grain boundary migration in these materials.

The voids that comprise the three-dimensional pore space between grains are called bulk defects. These cavities have sizes the same order of magnitude as the grains themselves, or larger. Presence or absence of these defects is normally a result of the manner in which the material was fabricated, rather than a property of the crystal, although under some circumstances grains may pull away from each other and create voids. The void network can consist of both isolated voids, which are completely surrounded by grains, as well as systems of voids that stretch through the structure.

The size and shape of the grain structure dictate the shape of the pore network. Curvature of the grain surfaces bounding a pore gives it a bulbous appearance, much like a snake that has swallowed several irregularly-sized eggs at random intervals. The narrow spaces, or throats, of this network control the rate at which fluid can invade or escape the pore space, but the large voids, or bulbs, control the length of time required to fill or empty this space with fluid. The radii of the throats and bulbs are functions of the manufacturing process, to be discussed next.

The spatial arrangement of grains in the microstructure also determines the average size and tortuosity of the pore space. Since arrangement of grains is effectively random, the path of a pore between them is random also,with no axial distance in the pore being greater than the typical grain diameter. Thus, the pore space is extremely tortuous.

The pore space may be described most accurately using a so-called nodes-links-blobs model[9], where the nodes are pore junctions, the blobs are pore bulbs, and the links are pore throats. Unfortunately, models such as this are frequently too complex to be

practically applied, because they often require detailed knowledge of pore dimensions that is very difficult to obtain. The most useful models are those that rely mainly on observation of the bulk properties of the material in order to predict its pore volume and structure. Percolation theory, a method of this type, will be considered shortly. However, the manner in which the microstructure may be manipulated will first be discussed.

c) Manipulation of the Microstructure

Ceramic processing is a broad topic which concerns formation of a finished ceramic device from a powder precursor. The objective of processing is to successfully manipulate grain growth in, and void space of, the final microstructure in order to control the properties of the final material. An important aspect of the work described in this thesis was the design of a processing scheme, utilizing the microstructural considerations described above, that could be followed to fabricate reproducibly model ceramic objects for use in studies of molecular transport. Preserving the pore structure and volume in the object were the primary concerns of this scheme. The ways in which processing can affect this structure, pertinent to this work, may now be briefly discussed, and particular procedures used in this work will be mentioned where appropriate. More general treatments of ceramic processing may be found elsewhere[10,11,12].

Particle Size and Mixing[13,14]

Processing of a ceramic begins by manipulating the properties of the powder used in its formation. A ceramic powder is made up of small discrete particles that are themselves composed of arrangements of crystal grains. The size of these particles, or alternatively their range of sizes, influences the properties of the final device. Powders may be classified as either monodisperse (consisting of particles of a single size) or polydisperse

(containing a range of particle sizes). These two types of powder typically exhibit much different processing behavior in regards to grain growth and void elimination.

Control of particle size, and elimination of polydispersity, is achieved primarily by powder milling, in which larger particles are broken apart by impact, which is then followed by separation according to size. Particle sizing was not performed in this study, since powders were used as received because polydispersity was needed to retain porosity in the final device.

The degree of polydispersity of a powder affects the ease with which its particles can be packed together, although this does not necessarily affect the density of the resulting packing. A monodisperse powder with very small particle size and one with very large particle size can, theoretically, exhibit equivalent packing uniformity within a given volume if all possible packing sites in this volume are filled. The total surface area of contact in a bed of large particles is much less than that in a bed of small particles, however, and the voids between larger particles are of larger size than those between smaller particles. A larger total contact area between particles is desirable because it facilitates grain boundary migration during heating. The surface energy of a small particle is greater than that of a large particle, as reflected in equation (1.1), so the tendency for grain growth as a means of lowering the energy of the system will be facilitated in a compact made from small particles.

Conversely, a polydisperse powder does not pack uniformly or efficiently, but a high total area of contact between its particles, as well as less void space, is theoretically possible because smaller particles in the powder can occupy the voids between larger particles. However, all possible packing sites are rarely occupied in a real system, especially in a polydisperse powder bed, which results in nonuniform bed density that is detrimental to later processing steps.

Most commercial ceramics are required to be as dense as possible, since the strength of the final product decreases as its total void space increases. Eliminating void space by efficient packing of the powder is the most convenient means of controlling final porosity, since the void space becomes more difficult to remove with each processing step. Powders that are small and monodisperse, or at least polydisperse over a very narrow size range, are thus most often used in ceramic manufacturing, since the highest packing densities may be achieved with such powders. Packing efficiency was not an important concern in the work described in this thesis, since a large void space was desired in the fabricated objects. Nonetheless, the processing behavior of a monodisperse powder was investigated in this work to compare it to the observed properties of the polydisperse powder used for the bulk of this research.

After sizing, the ceramic powder is mixed with other additives necessary for processing. The objective of the mixing step is to completely disperse these additives. This study compared two different mixing techniques, wet mixing and dry ball milling, to demonstrate how mixing of the powder mass affected both the behavior of the powder during processing and also the properties of the final product. The mixture used in this work consisted primarily of Al_2O_3 powder and a powdered polymer binder (poly(vinylpyrrolidone), or PVP), which will be discussed in the next section.

Wet mixing, or wet granulation, is used as a means of partially solubilizing the polymer binder in order to facilitate both its diffusion through the powder mass and coating of the ceramic material[15]. In wet mixing, the powder is formed into a slurry by adding deionized water, mixed, and later dried. The disadvantage of this method is that a large number of agglomerates is formed when the slurry is dried; however, these are very soft and may be broken up easily without altering the initial ceramic particle size.

The ball milling technique as generally used is basically powder mixing combined in

tandem with the particle size reduction process already discussed Mixing is achieved through rotation of a mill and impact of balls into the powders contained in the mill. In this work, ball milling was used only to mix the powders, not for particle size reduction; however, some size reduction may have occurred, as will be discussed in Chapter III.

Powder Compaction[16]

Packing of a powder may be controlled by compaction, which in this case involves applying external pressure to the powder mass to force its discrete particles closer together. The influence of pressure on the density of the packed bed is shown in Figure 1.2. Powder compaction results in increased contact area between particles, and a corresponding decrease in the total void space of the bed.

The density of a polydisperse powder compact is a stronger function of applied pressure than is the density of a monodisperse compact, because monodisperse particles can assume their final packing arrangements under lower pressure than can polydisperse particles. In either case, the desired result of compaction is to eliminate as much of the void volume as possible to increase the final strength. Although not an issue in the present study, at some point a compromise will have to be found between the required strength of a ceramic drug delivery device and its desired total porosity. The mean pore radius decreases with increasing pressure, but the minimum attainable void space is a function of particle size and polydispersity only.

A polymer binder is usually added to the powder to lubricate the ceramic particles during pressing and to bind the formed compact together after pressure is released. The polymer can account for up to 20% by weight of the total powder mass after addition. The polymer is assumed to be well-dispersed throughout the powder by mixing. Adding the polymer does not significantly alter the microstructure of the packed bed, as long as the

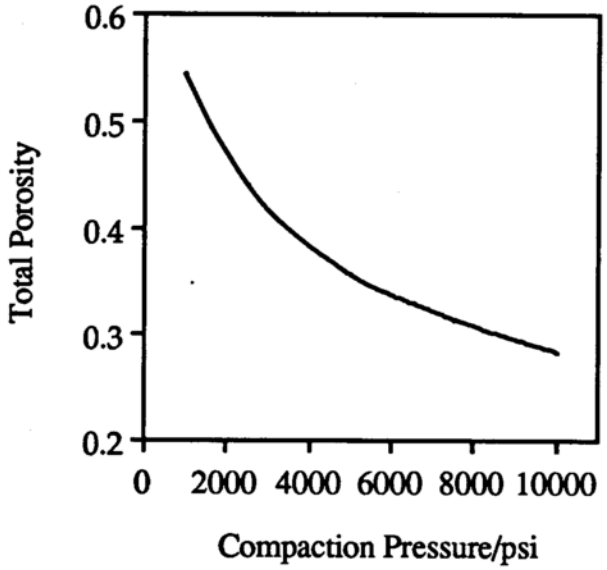

Figure 1.2. Influence of compaction pressure on compact density.
(Data from this work; listed in Table 3.2(a) in Chapter III.)

polymer is completely dispersed. Clumps of polymer can form during mixing, however, resulting in large voids in the microstructure after heating. Even though ceramic particles have some affinity for one another (through van der Waals attraction), it is very difficult to hold a compact together without some form of binder being present.

Powder compaction is achieved in this study by uniaxial pressing, in which all pressure is applied to one surface of the powder mass. This method is useful for creating small compacts, but it results in nonuniform density profiles as shown in Figure 1.3. This density variation cannot be eliminated regardless of the magnitude of the compaction pressure, but as this pressure becomes larger the densities of the discrete regions increase and the differences between them become smaller.

Burn-Out[10]

It is usually desirable to remove the organic binder before the final heating process is performed. The step of burn-out is used to vaporize and drive off the binder and any other volatile impurities (including water) from the body of the compact by heating. The rate of impurity volatilization is the chief concern of the burn-out process, since if the compact is heated too quickly vapor pockets will form in the body. The pressure in these pockets will increase until the vapor inside them literally explodes through the microstructure to escape, leaving large voids that cannot be removed. Heating must proceed at a rate that allows only small amounts of material to vaporize at a time, so that this vapor can diffuse out of the microstructure without disrupting it. The time required for burn-out increases, and the allowable rate of heating decreases, the denser the compact.

The heating rate can be increased near the end of the burn-out process, since binder removal opens more pore space for diffusion. The total void space in the compact increases slightly as a result of this step. Of course, controlling the rate of burn-out is less

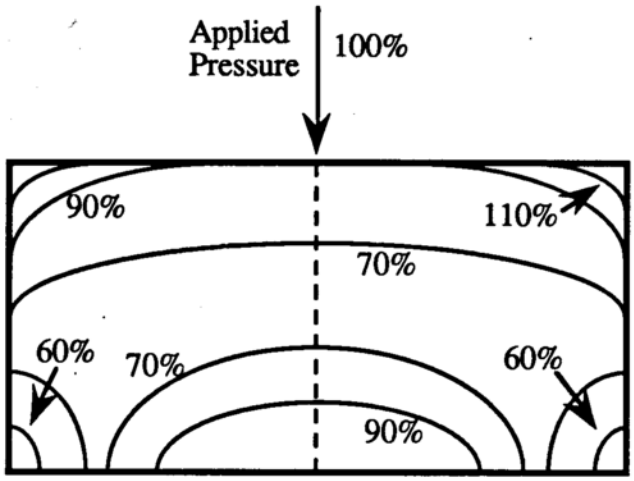

Figure 1.3. Density profiles in a ceramic compact due to uniaxial pressing[17]. Contours reflect percent of applied compaction pressure seen by the compact at that location. Note that pressure magnification occurs in the upper corners as a result of expansion of the material in the center.

a concern for compacts of higher initial porosity.

After burn-out has been completed, the compact consists only of particles of ceramic material loosely held together by attractive surface forces. These particles must be forced to grow together to impart strength to the compact, which is the purpose of sintering.

Sintering and Densification[10,18]

Sintering is a process of material flow between grains, caused by applying heat to the ceramic compact, used to achieve some desired final strength in the finished product. It works by facilitating defect migration as described above, such that new grains are formed and old grains either grow or disappear. The parallel process of densification occurs as growing grains fill the surrounding void volume, and typically results in shrinkage of the compact. Usually, the term "sintering" refers to both processes taken together, and will be used in this manner in this chapter. Also, the term "firing" is often used to refer to the overall heating process, and will be used as such here.

The driving force for sintering is the decrease in surface energy of a grain resulting from boundary migration. This process results in coalescence of those grains in the compact whose surfaces were initially in contact, and adherence of others through the strong interfacial energy of the boundary between them. A drawback of the densification process that often occurs during firing is that shrinkage of the compact can occur as grains grow and pores disappear. Figure 1.4 and Table 1.1 summarize the routes by which diffusion may occur during sintering; as will be discussed in Chapter III, surface diffusion and boundary diffusion appear to be the mechanisms governing sintering in this work. One or more of these mechanisms may occur during sintering. Mechanisms 4 and 5 are the only processes that result in shrinkage and elimination of porosity[19], implying that the sintering process does not necessarily result in densification.

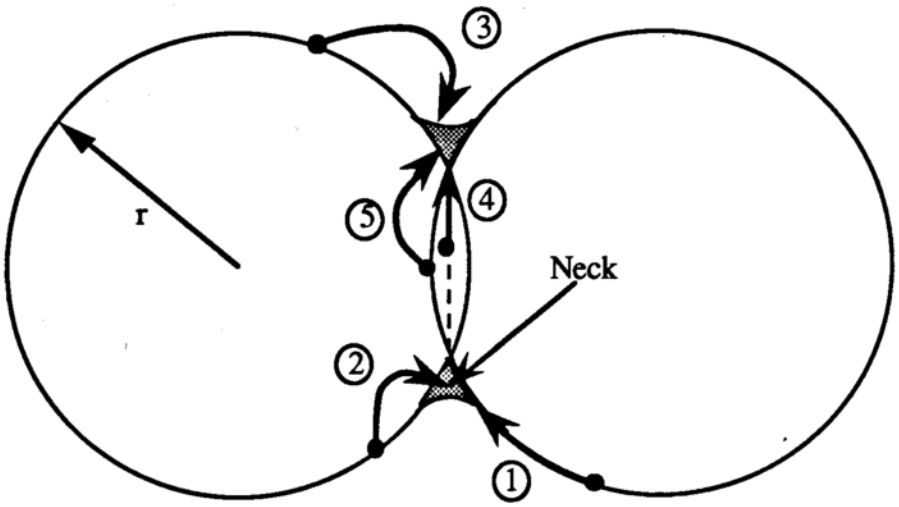

Figure 1.4. Diffusional processes occurring during sintering[19]. The shaded area (neck) indicates the region of grain coalescence. (See Table 1.1 for meanings of numbers shown.)

Table 1.1. Mechanisms of material flow during sintering[19].

Mechanism	Transport Path	Matter Source	Matter Sink
1	Surface Diffusion	Surface	Neck
2	Lattice Diffusion	Surface	Neck
3	Vapor Transport	Surface	Neck
4	Boundary Diffusion	Grain Boundary	Neck
5	Lattice Diffusion	Grain Boundary	Neck

As is the case with most diffusional processes, defect migration depends primarily on heat for its source of energy as given by equation (1.2) above. The final appearance of the microstructure is thus affected by the temperature used to sinter the compact, with grain boundary mobility increasing as this temperature increases[20]. The influence of temperature on densification depends on many factors, but may be roughly described as shown in Figure 1.5.

Most compacts exhibit an "initiation temperature" below which no noticeable sintering occurs; this temperature depends on the properties of the powder and its packing arrangement, and can vary even between different powder batches from the same manufacturer. The temperature used in most sintering processes depends on previously observed densification behavior of the material, and is usually about two-thirds the melting point of the ceramic. Pressureless firing with heating in an ambient atmosphere is the method employed in this work. Air is not expected to affect the ceramic microstructure in this method.

Along with temperature, the length of time this temperature is applied will affect the final structure. The effect of time on the densification process is described as[19]:

$$\frac{\Delta V}{V_0} = \alpha\, r^{-6/5}\, t^{2/5} \;; \qquad (1.3)$$

where ΔV is the volume shrinkage of the compact, t is the time at constant sintering temperature, r is average radius of the particles in the compact, and α is a lumped constant. Equation (1.3) describes densification mechanism #5 listed in Table 1.1; namely, lattice diffusion from the particle grain boundary to the neck region. The radius and time exponents of $-6/5$ and $2/5$, respectively, depend on the particular process described by the equation. The behavior of equation (1.3) for constant radius is summarized in Figure 1.6.

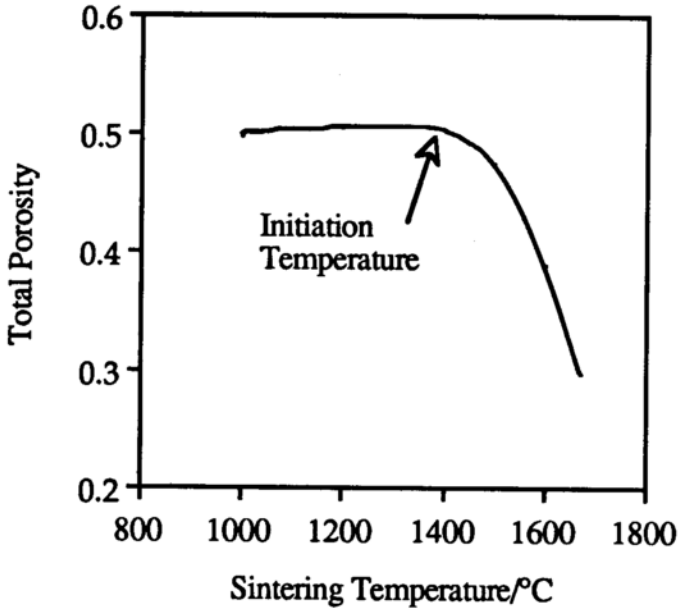

Figure 1.5. Dependence of final porosity on sintering temperature.
(Data from this work; listed in Table 3.6(a) in Chapter III.)

Note also from equation (1.3) that the sintering rate is inversely proportional to the particle size. Sintering to a desired final state may thus be achieved more rapidly if small particles are used. Equation (1.3) can be experimentally verified in many ceramic materials.

The rate at which the sintering temperature is reached is relatively unimportant, except with regards to build-up of thermal stresses. Slow rates of heating are advantageous, since they reduce the potential for cracking due to steep temperature gradients in the compact.

Densification may or may not occur during sintering, depending on the initial density of the ceramic compact. Voids that are smaller than the surrounding grains will be filled by coalescence of these grains, resulting in apparent shrinkage of the grain structure. Conversely, grains will not grow to fill large voids; in fact these voids will sometimes expand as the grains around them fill smaller voids[21]. Compacts with higher density have fewer and smaller voids, so there is less dead space in these compacts for grains to fill during sintering. Since narrowly polydisperse powders can be formed into higher density compacts than can monodisperse powders[22], some polydispersity can be beneficial to control shrinkage. Compacts made from very small monodisperse powders generally exhibit the greatest volume shrinkage if made as discussed in this section. Shrinkage minimization is typically a goal of the sintering process, since a ceramic product is often made in its final form before sintering.

Although they are attractive from the standpoint of shrinkage, polydisperse powders are made up of a wide variety of grain sizes. Large voids in the compact can result if such a powder is improperly processed, causing density variations through its structure. These regions may shrink to different extents, or alternatively may not shrink at all, if the voids are too large. The compact shown in Figure 1.3 is a good example of a compact that will shrink nonuniformly due to density variations in the interior. Whereas large voids resulting from random packing of a polydisperse powder can be detrimental to the strength of the

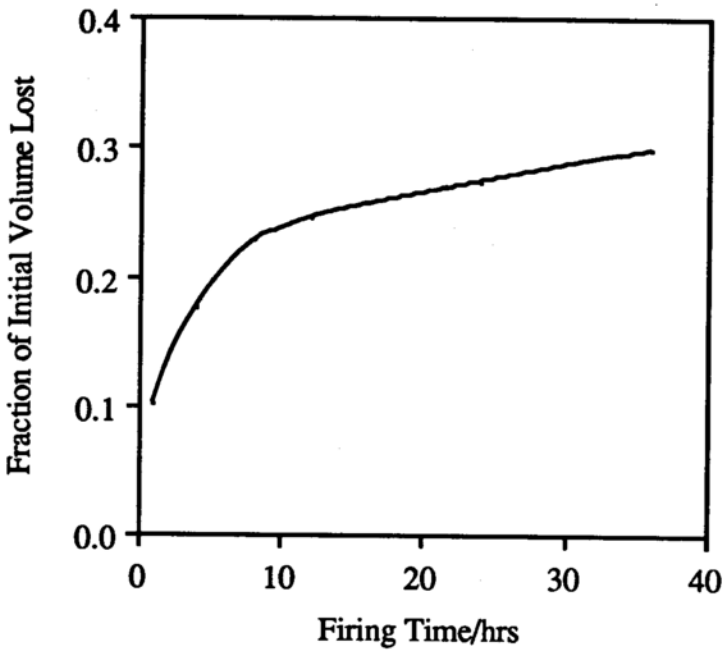

Figure 1.6. The effect of sintering time on volume loss during firing. (Data from this work; listed in Table 3.7 in Chapter III.)

final product, it was used to advantage in this work since including large voids before sintering is a way by which porosity may be maintained and shrinkage reduced[23].

Small amounts (less than 1% by weight) of other ceramic materials are often added to the primary ceramic powder before compacting to influence certain aspects of grain boundary migration during sintering. Different additives have different effects, but most act by forming impurities on the surfaces of the grains and in the boundaries between them that either retard or accelerate the motion of these boundaries, thus altering the rate of sintering. For example, MgO is used to control size and growth of alumina grains during sintering in this study[24,25], to ensure that growth of individual grains does not occur to such an extent as to eliminate portions of the void space. The process of grain growth in which some grains grow very large at the expense of small grains is called secondary recrystallization; this phenomenon is undesirable because it disrupts the uniformity of the microstructure.

The microstructure having now been discussed, the properties of Al_2O_3 pertinent to this work are summarized next.

d) Structure and Physicochemical Properties of Aluminum Oxide

Aluminum oxide typically exists as an ionic crystal[13], the conformation of which varies depending on the technique used in its chemical synthesis. The thermodynamically stable phase under the experimental conditions used in this work α-alumina, or corundum, which possesses the hexagonal close-packed form shown in Figure 1.1(b). A value of 3.985 g/cm^3 has been reported for the maximum density of the corundum lattice[26]; a value of 4.0 g/cm^3 is used here, primarily for purposes of illustration.

Important properties of Al_2O_3 are summarized in Table 1.2. A quantity which may be noted for use in later discussion of biocompatibility is the dielectric constant (K), which

Table 1.2. Some physical and chemical properties of α-alumina at 25°C.

Property	Value	Ref.
Dielectric constant	9.39	26
Electrical resistivity	10^{12} ohm cm	12
Compression strength	30,000 $^{kg}/_{cm^2}$	26
Melting point	2050 °C	12
log(equilibrium constant)	277.201	27

indicates the ability of alumina to act as an insulator. The lower the dielectric constant of a material, the better are its insulating properties, with a vacuum being the perfect insulator (K = 1). For comparison[28], the dielectric constant of water is 78.54. A review of the forms and properties of alumina may be found elsewhere[29]. The reaction used to determine the equilibrium constant is as follows[29]:

$$Al_2O_3\ (c) \rightarrow 2\ Al\ (s) + {}^3/_2\ O_2\ (g).$$

The surface energy of alumina is not given in Table 1.2, since like other ceramic materials it is too high to measure accurately. The actual energy of the bare surface is not an issue, however, except during sintering. At room temperature, if the crystal surface is exposed it will very rapidly adsorb a layer of water and hydroxide ions, thereby reducing the apparent surface energy of the crystal to nearly that of water. This adsorbed layer of water is stripped away by the temperatures used in sintering, thus promoting contact between adjacent grains.

With an understanding of the ceramic microstructure, it is straightforward to show how and why percolation theory can be applied to such a system. This is the subject of the next section.

C. Percolation Theory Analysis

1. Percolation Theory

Percolation theory is a statistical technique used to model the behavior of random systems or processes. Its derivation involves modeling of the random walk of an "ant" through contiguous areas of a lattice. Ideally, simple power law relationships, which can be used to describe the overall behavior of the ant and not the individual steps that it takes,

may be developed from the random walk. A complete development of percolation theory may be found elsewhere[30,31]; those points that are pertinent to the modeling procedure used in this work will be considered next.

a) The Lattice Percolation Model

The first concept in the percolation theory model is the definition of a lattice. The lattice may be of any dimension. Representative two- and three-dimensional lattices appear in Figures 1.7(a) and 1.7(b). Note that the lattices shown are constructed from squares and cubes, in analogy to the unit cells of real crystals discussed previously.

Using Figure 1.7(a), a site may be defined as either the center of a square, or alternatively the corner of a square. For convenience, if the corners are chosen as sites, then the bonds between them may be defined as the sides that join adjacent sites. An ant traveling through this lattice may either hop between adjacent sites, or may walk the bonds between sites.

If some sites are removed at random, there will exist a probability P that a given site (x) is present; this probability is referred to as P(x). The ant is then restricted to jumps between those sites that are actually present. This is referred to as a site model for the random walk; the ant does not use the bonds between sites in this model. On the other hand, if all sites are assumed to be occupied but some of the bonds are removed at random (again, with probability P(x)), the ant can sit on any site but is restricted in the bonds available for movement. This is the bond model for the random walk. Percolation in a real system may follow either model, or can be a combination of the two[32].

In the lattices shown in Figure 1.7, each unit cell has a number of nearest neighbors that is equal to the number of sides of that cell. For instance, a unit cell in the two-dimensional square lattice has four nearest neighbors, while the three-dimensional cubic

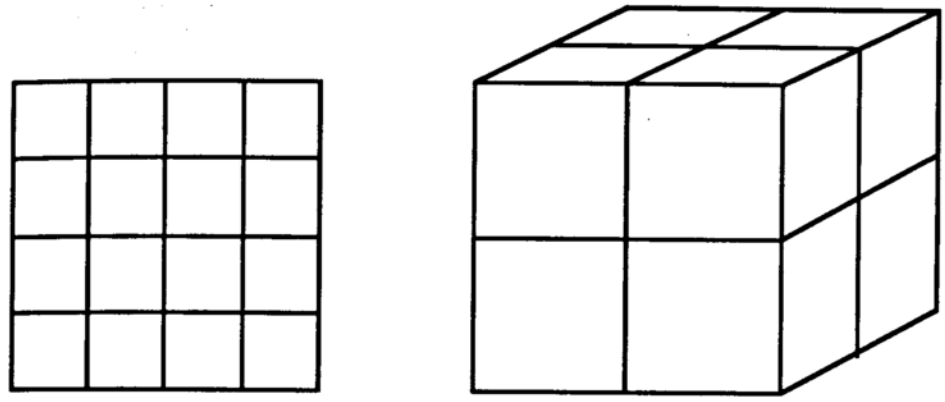

(a) Square Lattice (b) Cubic Lattice

Figure 1.7. (a) 2-dimensional square lattice, (b) 3-dimensional cubic lattice.

lattice has unit cells with six nearest neighbors. The number of sites (occupied or not) adjacent to a central site will be equal to this number of nearest neighbors, and the possible bonds that a single site may possess is also equal to this number. In percolation theory, the number of nearest neighbors of a unit cell is known as the coordination number (z) of the lattice. The magnitude of z reflects the complexity of the lattice.

There are two assumptions that form the basis of the percolation model. One, as mentioned, is that the system of sites and/or bonds is statistically random. The other is that the lattice is infinite in length, such that the ant will need an infinite number of hops to cross it. This assumption is needed in order to force certain properties of the lattice to converge to definite values, since these properties will possess a range of values in a finite system. For instance, on a square lattice of four unit cells, the probability that enough sites will be occupied for the ant to hop from the bottom to the top of the lattice may either be $P(x) = 3/9$, $P(x) = 4/9$, or $P(x) = 5/9$, as shown in Figure 1.8. In an infinite lattice, these probabilities converge to a single number that can be more easily modeled. Unfortunately, the use of this assumption results in deviation from the theory in finite systems, which must be corrected for as will be shown shortly. No real lattice is truly infinite, but may be approximated as such if its structure meets certain criteria.

An associated group of occupied (or unoccupied) sites in a lattice is called a cluster. (Bond clusters may be defined analogously.) A finite, or isolated, cluster is bounded on all sides by sites of the opposite property. The ant can hop about in such a cluster indefinitely, but can never escape the cluster. A cluster is assigned a certain radius R(x) depending on the average number of possible steps an ant would require to cross it. An infinite, or sample-spanning, cluster stretches through the infinite lattice, such that it is possible for the ant to find a complete path from one side of the lattice to the other. The radius of such a cluster is thus infinite. Clusters which meet only one side of the lattice are considered

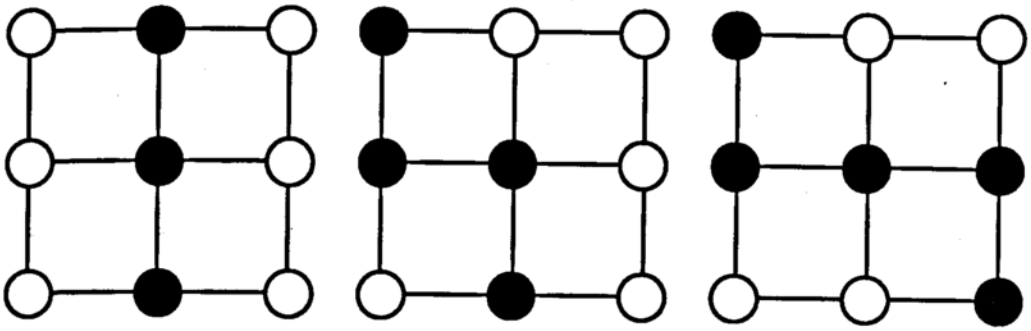

P(x) = 3/9 P(x) = 4/9 P(x) = 5/9

Figure 1.8. Different probabilities of occupied sites crossing a lattice in a finite system.

finite. A summary of the types of clusters that may be found in a percolation lattice is shown in Figure 1.9.

An infinite lattice possesses a definite point at which one cluster becomes large enough to span the lattice. Below this point, all clusters have finite radii, but grow and coalesce as this point is approached. This point, a discontinuity at which the cluster radius becomes infinite, is known as the critical percolation threshold of the lattice. Above this point, the total lattice volume taken up by sample spanning clusters increases, and the volume of finite clusters decreases.

The critical percolation threshold depends on the coordination number of the lattice. Some representative two- and three-dimensional lattice coordination numbers and their thresholds appear in Table 1.3[33]. A relationship between the critical percolation threshold and the coordination number in three dimensions may be obtained by fitting these values, as follows:

$$\emptyset_c = \frac{1}{1 + 0.356\, z}\ ; \qquad (1.4)$$

where $\emptyset_c$ is the critical percolation threshold and z is the coordination number of the lattice. It is important to note that the critical percolation threshold decreases as the lattice becomes more complex.

The nodes-links-blobs model may be used to describe the void space in a real lattice, with the nodes as sites, and the links and blobs as bonds of varying thickness. Pores may be considered as clusters of these voids. The critical percolation threshold for such a system is that total porosity at which one pore becomes long enough to span the lattice, thus (theoretically) allowing a molecule to travel from one side of the lattice to the other. Increasing the total porosity above the threshold produces more pathways for molecules to

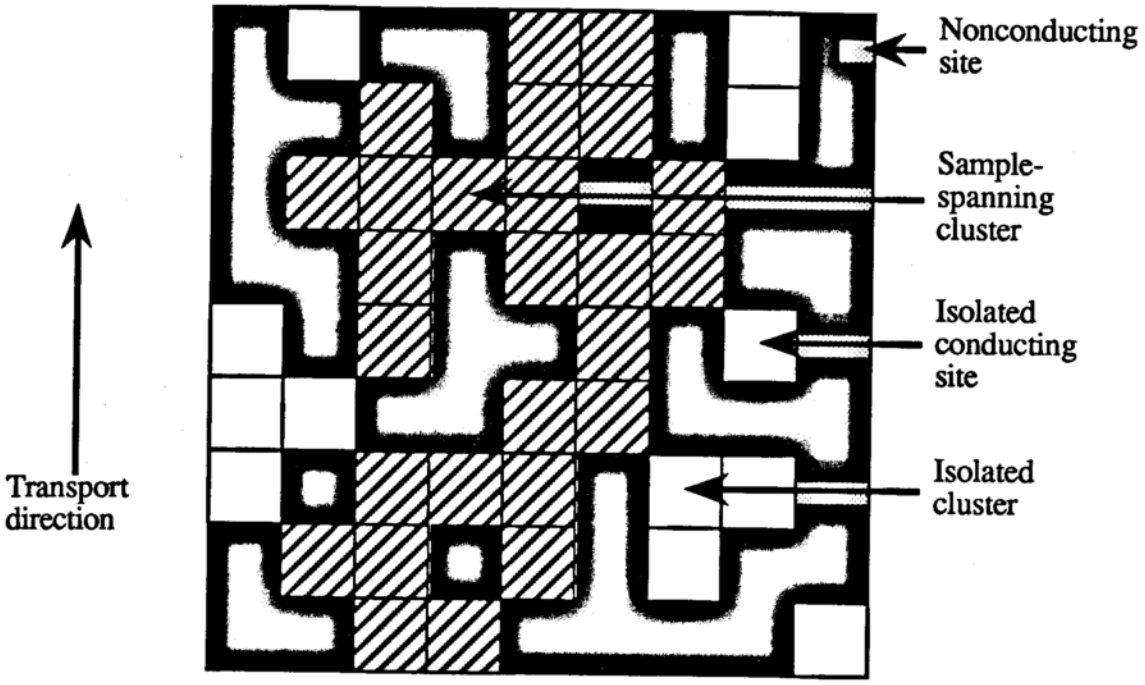

Figure 1.9. Different types of clusters on a two-dimensional square lattice.

Table 1.3. Lattice coordination numbers and percolation thresholds obtained by computer simulation.

Unit cell	Dimension	Coordination number (z)	Percolation threshold ($Ø_c$)
Triangle	2	3	0.697
Square	2	4	0.591
Hexagon	2	6	0.5
Random polygon	2	6 (average)	0.5
Diamond	3	4	0.425
Cube	3	6	0.320
Tetrakaidecahedron	3	14	0.175
Random polyhedron	3	15.54 (average)	0.16

travel through the lattice. The site model, in which only a spanning cluster of nodes is important, is the one of interest here, so the bond model will not be considered further. Power laws have been developed to describe the various pore structures that contribute to site transport in a lattice, and will be considered next.

b) Scaling Relationships

The percolation threshold represents a discontinuity in the properties of a lattice. The behaviors of percolation properties near such a discontinuity may be described by a power law[34] of the form $(y-y_0)^{\alpha}$, where y is an independent property, y_0 is some initial, or critical, state of that property, and α is a critical exponent obtained in the power law expansion. The power law represents the fluctuation of a property about some mean value, and its expansion describes the terms, or moments, which govern this fluctuation.

A scaling law is based on the power law expansion, and relates some property that is a function of y to the magnitude of the deviation $y-y_0$. Different properties are affected differently by this deviation as a result of the critical exponent α used in the expression. α is often called a universal exponent, because (except in special cases) it only depends on the dimensionality of the system and not on y or y_0.

The average cluster radius $\langle R \rangle$ of an infinite lattice diverges as the critical percolation threshold is approached from below (both quantities become discontinuous) as follows[35]:

$$\lim_{\emptyset \to \emptyset_c} \left[\frac{\langle R \rangle^2}{(\emptyset_c - \emptyset)^m} \right] \to \infty \; ; \qquad (1.5)$$

where $\emptyset$ is the total porosity of the lattice, and m is a universal exponent equal to 1.4. To describe cluster properties above $\emptyset_c$ a different representative length than R must be used, since R disappears at $\emptyset_c$ as shown in equation (1.5). This new length, the correlation

length ξ, may be defined[34] as the difference by which the degree of percolation on a lattice with total porosity $\emptyset > \emptyset_c$ differs from the degree of percolation on the same lattice with total porosity $\emptyset_c$. As this difference grows, the magnitude of ξ decreases as given by equation (1.6):

$$\xi \propto (\emptyset - \emptyset_c)^{-\nu} \; ; \tag{1.6}$$

where ν is a correlation length exponent equal to 0.9 in three dimensions. The value of ξ diverges as $\emptyset$ approaches $\emptyset_c$ from above. The expression shown in equation (1.6) is an example of a scaling relationship.

In systems such as used in this work, the correlation length reflects the degree to which the pore structure influences the movement of molecules through the lattice. At very high porosities, the pore structure becomes less important to transport, but near the threshold transport is controlled by this structure. ξ thus achieves limiting values at $\emptyset = 1$, at which the pore structure has no influence on transport, and $\emptyset = \emptyset_c$, where the pore structure has infinite control over transport.

The correlation length scaling relationship given in equation (1.6) can be used to obtain other scaling expressions more useful in describing the pore structure near the threshold. For instance, a pore may be isolated, as defined previously, or it may be accessible to the outside. These types of pores were shown previously in Figure 1.9. An accessible pore is analogous to a sample-spanning cluster, and may be defined[33] by this scaling relationship:

$$\emptyset^A \propto (\emptyset - \emptyset_c)^{\beta} \, , \emptyset > \emptyset_c \; ; \tag{1.7a}$$

where $\emptyset^A$ is the accessible volume fraction of the lattice, and β is a scaling exponent

referred to as the strength of the infinite network. β usually takes on the value 0.4 in three dimensions. Since β is less than one, $\emptyset^A$ will go to zero as $\emptyset$ approaches $\emptyset_c$ from above. $\emptyset^A$ is defined as being identically equal to zero at and below $\emptyset_c$ as shown:

$$\emptyset^A \equiv 0 \, , \emptyset \leq \emptyset_c \; . \tag{1.7b}$$

The total porosity is then simply the sum of the accessible and isolated volume fractions as follows[36]:

$$\emptyset = \emptyset^A + \emptyset^I \; ; \tag{1.8}$$

where $\emptyset^I$ is the isolated porosity. Note that for $\emptyset \leq \emptyset_c$, the total porosity becomes equal to the isolated porosity.

The accessible porosity may be broken down into backbone ($\emptyset^B$) and dead-end ($\emptyset^D$) volume fractions, as shown in Figure 1.10 and given by the following[36]:

$$\emptyset^A = \emptyset^B + \emptyset^D \, , \emptyset > \emptyset_c \, . \tag{1.9}$$

Below the percolation threshold, $\emptyset^A = \emptyset^B = \emptyset^D = 0$ by definition. A backbone pore is that fraction of an accessible pore that forms a continuous pathway across the lattice, but does not include the dead-ends of the accessible pore structure. Since the backbone pore space represents a contiguous, definable structure, it may also be represented[33] by a scaling law such as:

$$\emptyset^B \propto (\emptyset - \emptyset_c)^{\gamma_B} \, , \emptyset > \emptyset_c \; ; \tag{1.10}$$

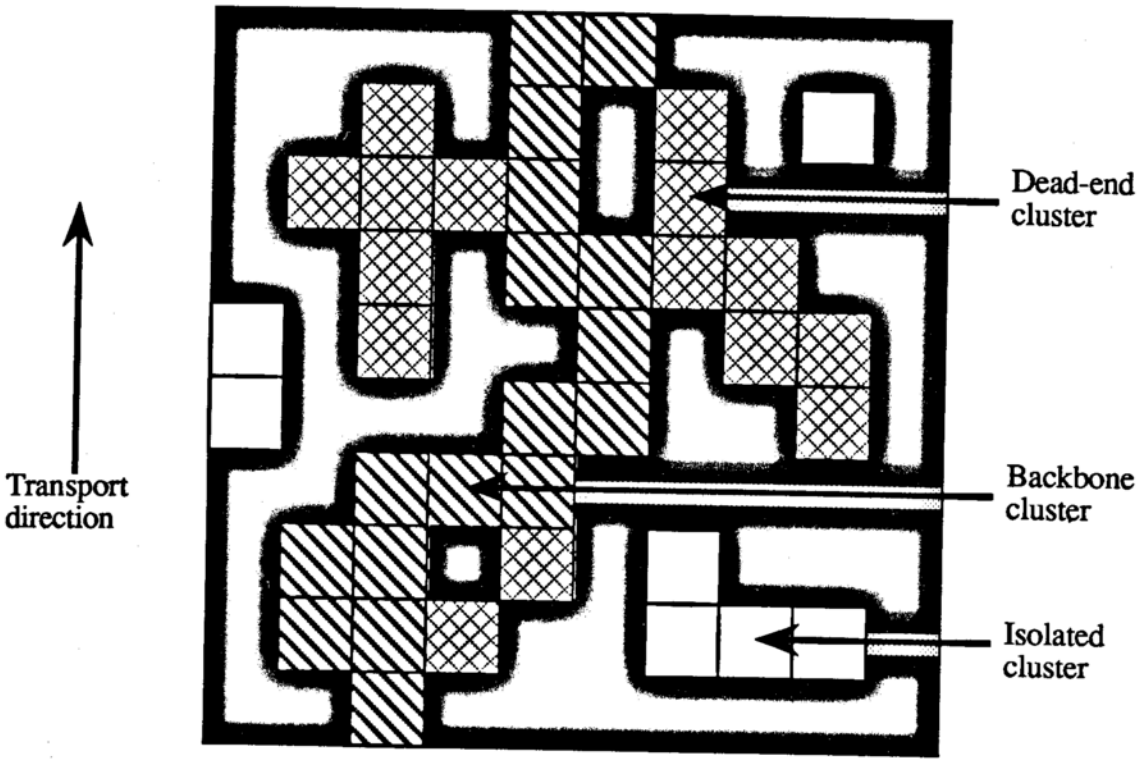

Figure 1.10. Backbone and dead-end pore clusters on a two-dimensional square lattice.

where γ_B is the backbone lattice exponent, equal to 0.9 in three dimensions[33]. Since γ_B is less than one, $\emptyset^B$ will go to zero at the threshold in the same manner as $\emptyset^A$. Scaling expressions cannot be defined for $\emptyset^D$ or $\emptyset^I$.

The above parameters $\emptyset^A$, $\emptyset^I$, $\emptyset^B$, and $\emptyset^D$, taken together, may completely describe the morphological characteristics of the lattice. However, these quantities do not adequately describe the observed transport of a molecule through the lattice near the percolation threshold, since such transport would be expected to fall to zero as $\emptyset_c$ is approached rather than becoming discontinuous. A scaling relationship is available[37] that relates the fraction of the pore structure actually used in steady-state transport of a molecule through this lattice to the total porosity of the lattice, as follows:

$$\emptyset^E \propto (\emptyset - \emptyset_c)^{\mu} , \emptyset \geq \emptyset_c \ ; \qquad (1.11a)$$

where $\emptyset^E$ is the volume fraction of the pore space that is effectively used for molecular transport, and μ is the conductivity exponent (equal to 2.0 in three dimensions). Note that $\emptyset^E$ will disappear at the threshold since the exponent μ is greater than one, so below $\emptyset_c$ the value of $\emptyset^E$ is defined as zero:

$$\emptyset^E \equiv 0 , \emptyset < \emptyset_c \ . \qquad (1.11b)$$

$\emptyset^E$ is related to the correlation length as follows:

$$\emptyset^E = \xi^{-\mu/\nu} , \emptyset \geq \emptyset_c \ . \qquad (1.12)$$

The effective volume fraction is a reflection of the dependence of the diffusivity of a

molecule in the lattice on the total porosity of that lattice. The ratio of the bulk diffusivity of a molecule in the lattice to its aqueous diffusivity may be taken as $\emptyset^E$, as shown[33]:

$$\emptyset^E = \frac{D_B}{D_{aq}} \; ; \tag{1.13}$$

which is valid as long as the molecule is dilute as compared to the total pore volume. This restriction is followed as long as the mean free path of the random walk of the molecule is smaller than the pore diameter, so that Knudsen diffusion does not occur. The value of $\emptyset^E$ is thus seen to depend on the size and other transport properties of the molecule used to obtain this value, which is not the case with the morphological parameters described previously. Rather, the volume fraction effective may only approximate the backbone volume fraction only if an infinitely small molecule is used to obtain D_B.

Equation (1.11a) is only strictly valid near the percolation threshold. As the total porosity increases, molecular transport approaches the more generally-applied relationship of equation (1.14) for estimating bulk diffusivity[31]:

$$L^2 = D_B \, t \; ; \tag{1.14}$$

where L is the system thickness and t is the time required to cross the system. Divergence of this equation as the percolation threshold is approached justifies the need for equation (1.11a) near $\emptyset_c$.

Figure 1.11 summarizes the trends of the five volume fractions as functions of the total porosity of the lattice. Because μ is greater than one and β and γ_B are less than one, $\emptyset^E$ will be less than $\emptyset^A$ and $\emptyset^B$ except at $\emptyset = \emptyset_c$ and $\emptyset = 1$. The following general relationships are seen to hold between the various volume fractions:

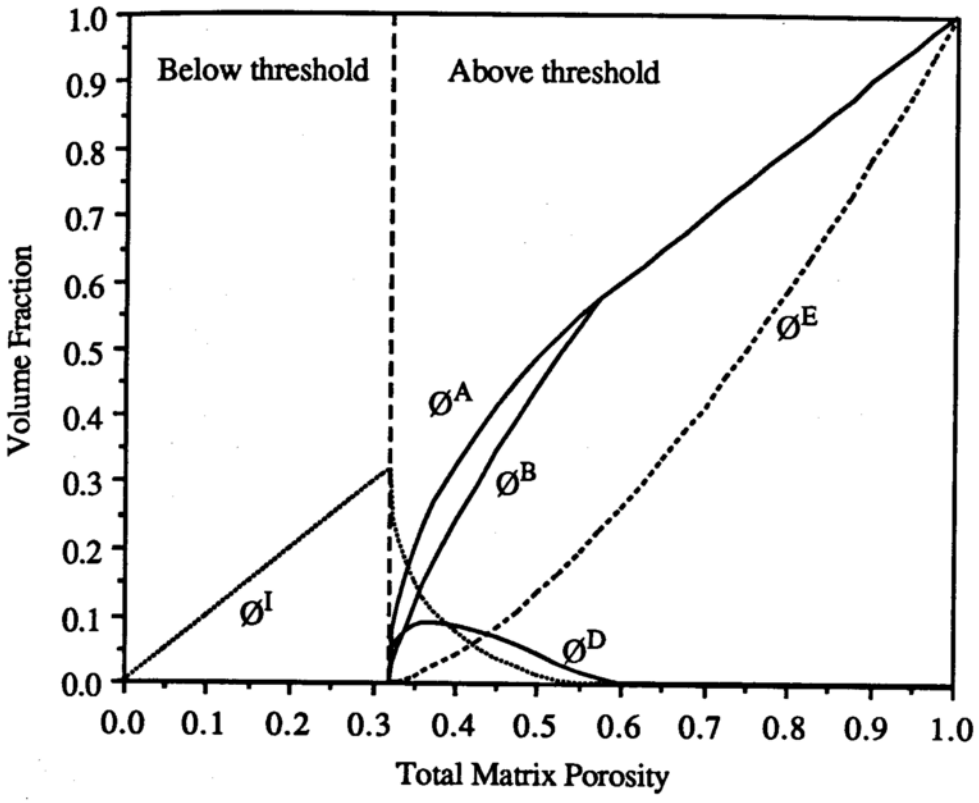

Figure 1.11. Trends in the values of various volume fractions as functions of total porosity, three-dimensional cubic lattice[33].

$Ø^I$ = volume fraction isolated;
$Ø^A$ = volume fraction accessible;
$Ø^B$ = backbone volume fraction;
$Ø^D$ = dead-end volume fraction;
$Ø^E$ = volume fraction effective.

$$\emptyset^D \leq \emptyset^B \leq \emptyset^A \ ;$$

$$\emptyset^E \leq \emptyset^B \ .$$

Since $\emptyset^E$ and $\emptyset^B$ depend on transport and morphology, respectively, it is not rigorously correct to equate their values.

The infinite lattice assumption holds as long as the volume of a given pore is negligible with respect to the system size. When this requirement breaks down, the concepts discussed above must be modified to account for deviations due to the finite size of the system. This branch of percolation, called finite-size scaling, will be discussed next.

c) Finite Systems

The cluster radius, which becomes infinite in an infinite system, will approach the linear thickness of the lattice in a finite system. Thus, the correlation length will achieve its maximum not at infinity but at a scaled system length as given[38]:

$$\xi \propto L^{-1/\nu} \ , \emptyset = \emptyset_c \ ; \qquad (1.15)$$

where L is the linear thickness of the system (in number of sites). The quantities shown in Figure 1.11 will thus not fall to zero at $\emptyset_c$ in a finite system, but will instead converge to finite minima.

Of particular importance in the study of finite size effects is the manner in which the volume fraction effective scales at the threshold, since this quantity will not become zero at $\emptyset_c$ of an infinite lattice but will decay at a much slower rate below this threshold. Scaling of $\emptyset^E$ is assumed to follow[39]:

$$\emptyset^E \propto L^{-\mu/\nu} \Phi\left[(\emptyset - \emptyset_c) L^{1/\nu}\right] ; \qquad (1.16)$$

where $\Phi(\emptyset,L)$ is a function that is finite and positive for $\emptyset < \emptyset_c$. It is the object of some studies of finite-size scaling to determine this function Φ.

Finite-size scaling behavior is often used to estimate the values of the scaling exponents[40]. For instance, varying $\emptyset$ and L and knowing $\emptyset_c$ for the infinite lattice allows μ and ν to be estimated by first measuring $\emptyset^E$ and then plotting the result versus $L(\emptyset-\emptyset_c)$. L may be varied in a real system by increasing the pore diameter (d) until the accepted criterion for the onset of finite-size effects, $^d/_L > {}^1/_{50}$, is met[41]. A particular way to perform this manipulation will be discussed shortly.

An effect that will occur in any real system, even one which can be approximated as infinite, is that of the contribution of surface porosity to the apparent value of $\emptyset^A$ obtained experimentally. The surface porosity $\emptyset^S$ may be defined as the fraction of pores that is accessible to the surface, but does not interact with any sample-spanning cluster that is included in the volume fraction accessible as defined by percolation theory. Surface porosity is depicted in Figure 1.12. $\emptyset^S = 0$ in the idealized cases discussed thus far.

In analogy to equation (1.8) above, $\emptyset$ may be redefined to include surface porosity as follows:

$$\emptyset = \emptyset^A + \emptyset^I + \emptyset^S ; \qquad (1.17)$$

where $\emptyset^I$ is the true volume fraction isolated that may be experimentally observed for a lattice with surface pores.

Below $\emptyset_c$ the surface volume fraction may be solved for directly, as given by:

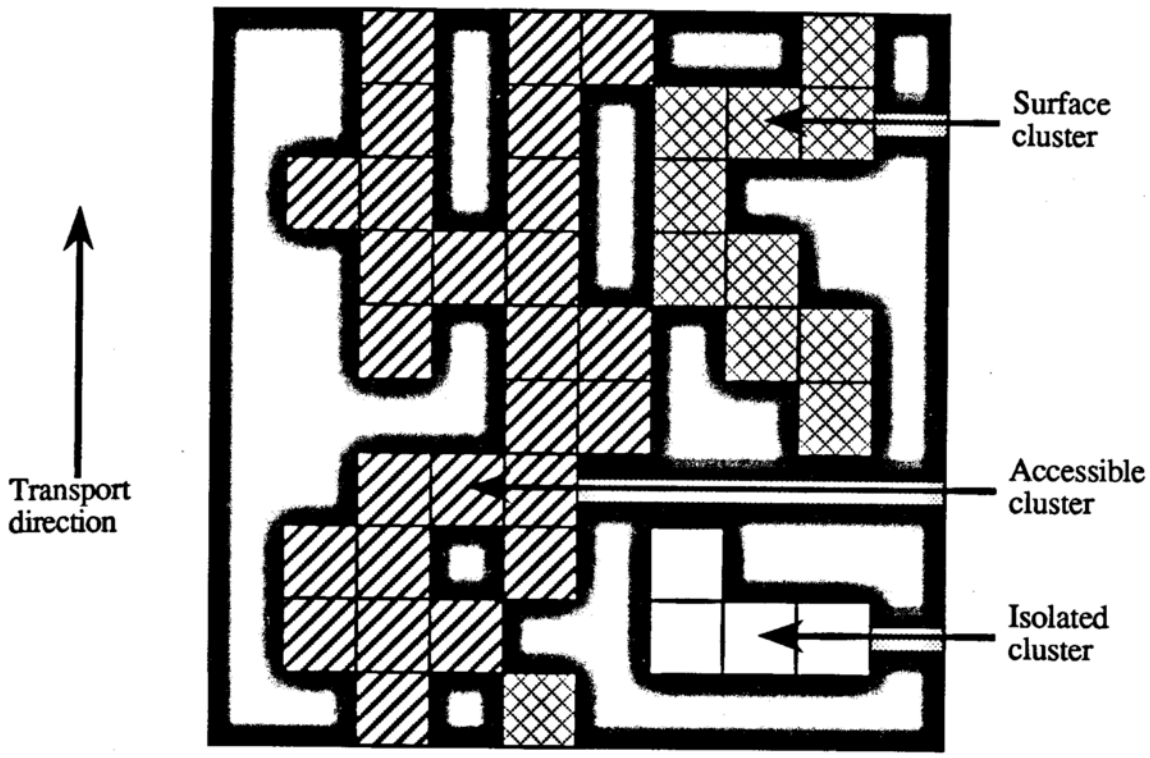

Figure 1.12. Accessible, isolated, and surface clusters on the two-dimensional square lattice.

$$\emptyset^S = \emptyset - \emptyset^I \, , \emptyset < \emptyset_c \; ; \qquad (1.18)$$

which shows that $\emptyset^S$ is a linear function of $\emptyset$ and $\emptyset^I$ in that region. $\emptyset^S$ may thus be obtained by experiment when $\emptyset \leq \emptyset_c$. Since the surface porosity above the threshold will not, in general, be known, it can be difficult to obtain an explicit value for the volume fraction accessible by experiment.

d) Investigation of Percolation Parameters

Relatively little experimental work exists regarding the verification of percolation theory. Rather, most studies of percolation are carried out through computer simulations of very large lattices with varying coordination numbers, since it is much easier to change certain properties of the lattices and observe their effects on a computer than in reality. Computer simulations are applied primarily because the complicated morphologies of lattices with high coordination numbers make exact analytical solutions of their percolation behavior impossible. Analytical solutions are currently limited to simple systems such as the one-dimensional lattice, the two-dimensional triangular lattice, and a special structure known as the Bethe lattice[42].

The Monte Carlo simulation is the computer modeling technique of choice for percolation problems[43]. This method uses a random number generator to build a lattice and remove certain of its sites or bonds, and then studies the connectedness of the resulting arrangement. The porosity of such a generated lattice may be easily varied. Finite size scaling may also be studied in this manner by manipulating the system size. Most percolation theory literature concerns the use of the Monte Carlo approach to verify the equations given previously, and also to obtain critical exponents and percolation thresholds. The thresholds given in Table 1.2 were obtained by this method.

Experimental work in verifying percolation theory has primarily dealt with conductivity measurements in porous systems. A method[44] of varying the conductivity has involved dispersion of a conducting powder in a nonconducting powder, sintering, and then observing the conductivity as a function of volume fraction conductor (σ). The effective conductivity as a function of the amount of conductor present is modeled as:

$$\Sigma \propto (\sigma - \sigma_c)^{\mu} \; ; \tag{1.18}$$

of which equation (1.11a) is a variation. Here, Σ is the effective conductivity of the lattice and σ_c is the conduction threshold. One set of studies has involved the measurement of Σ in porous alumina ceramics saturated with electrolyte[45,46]; its results will be compared to this work in Chapter V.

Work performed in our laboratory has investigated the percolative transport properties of poly(vinyl stearate) matrices in which a model drug molecule has been dispersed[47], and also of model disks of hydroxyapatite and calcium phosphate ceramics[48]. Percolation theory was shown to be a valid modeling technique in both systems.

Experimentally, some morphological percolation parameters may be determined by a detailed analysis of the total pore space of the ceramic device, while the volume fraction effective can be estimated by observing the transport of a model molecule through the device.

2. Modeling of Porous Alumina Ceramics

In keeping with work already performed in this laboratory, the extremely complicated pore morphology of a sintered alumina device makes it an ideal candidate for study using percolation theory. First of all, other work has shown that the average structure of a mass

of grains in a ceramic or a metal may be approximated by the fourteen-sided polyhedron, known as a tetrakaidecahedron[49]. This object has a coordination number of 14 and a site percolation threshold (obtained through Monte Carlo simulation of transport) of approximately 0.17. Using this approximation to the true lattice structure, it is possible to verify whether or not the devices made in this laboratory possess transport characteristics similar to those of computer models through comparison of experimental and simulated values of $\emptyset_c$. The value of D_B is obtained experimentally by applying a membrane transport model to diffusion through the alumina matrix, as will be described in the next chapter.

Almost no previous experimental work exists that addresses whether or not the morphological percolation parameters $\emptyset^A$ and $\emptyset^I$ disappear at the value of $\emptyset_c$ predicted through simulation. The effect of surface porosity is expected to make verification of the scaling relationship for volume fraction accessible very difficult, although the critical percolation threshold needed in equation (1.7a) can be obtained directly from volume fraction isolated data.

Finally, it is possible to experimentally observe finite-size scaling by making the pores in the matrix artificially large, thereby forcing the d/L ratio mentioned previously to be greater than $1/50$. In such a system, anomalously high diffusion should be observed at the value of $\emptyset_c$ obtained for an infinite lattice, and the function Φ should be obtainable from this high diffusivity.

The background given in the previous sections is important in that it may now be applied to explaining what may be obtained from the study of this system. Such a concern is the subject of the remainder of this chapter.

D. Ceramics in Drug Delivery

Investigation of ceramic materials as potential carriers of drug molecules is a new area of research. It is important to describe the reasons for study of these materials in detail, which is the intent of this section. A review of the topic of biocompatibility of implant materials will be given first, and then a more specific treatment of the *in vivo* behavior of porous ceramics will be discussed.

1. BIOCOMPATIBILITY

a) Biomaterials

A biomaterial is commonly defined as any material, organic or inorganic, that may be used in a physiological environment without adversely affecting its surroundings[50]. This definition is often further restricted to those materials that are used to replace a tissue or modify its function in order to repair a physiological defect by mimicking the role of the original tissue.

Aside from whether or not a biomaterial successfully approximates the properties of the original tissue, the most important aspect of such a material may be its biocompatibility. However, no standard definition exists as to what properties a material must possess for it to be classified as "biocompatible". In general, a material is considered biocompatible if it does not cause a significant foreign-body reaction when introduced to a biological tissue[51]. This is not to say that there is no response of the immune system to the material, but rather that such a response does not result in either the destructive modification of tissues local to the implant or in a compromise of the normal functional ability of the host.

In general, a biocompatible material is said to be either "bioinert" or "bioactive". A bioinert material may be used *in vivo* without stimulating any significant tissue response other than the typical response to an injury; thus, the immune system should not recognize

such a material as being foreign. Note that a bioinert material cannot elicit any synergistic response from the tissue, either; it should perform no function other than to provide support. Such materials, therefore, find wide application in prosthetic device technology, since (ideally) a structural implant such as a hip replacement prosthesis should not provoke an immune response in the patient. Aluminum oxide, and some other ceramics, are good examples of this type of material[52].

In comparison, a bioactive material will usually induce some desired response from the tissue in which it is introduced. This response must not be detrimental to the tissue or the overall organism, but rather should aid in integration of the material by the tissue and/or in healing of the original injury. An ideal bioactive material would be one which could be used to actually replace or improve the function of an impaired tissue, but no such material has as of yet been developed.

What properties a material must possess in order for it to be bioinert or bioactive are not clearly understood, although the more general differences between biocompatible materials and those that are not have been simpler to determine. These general properties, especially as applied to ceramics, will be the subject of the remainder of this section.

b) Surface Considerations

The observable behavior of a biomaterial is governed by the properties of its surface. Most ceramics possess reactive surfaces due to a deficiency of electrons in the surface faces of the crystal lattice. Such a "clean" surface possesses a slightly higher energy relative to the interior[53], and is electronegative with respect to an aqueous solution. From a free energy standpoint, it is highly favorable for adsorption of hydroxide ions and water to take place at this surface due to its high reactivity[54], with the result that a neutralizing water layer is typically observed to accumulate at the surface. This layer of water may act to

"hide" the reactive ceramic surface, thus preventing it from exerting any effect on the surrounding tissue.

Along with surface energy, the morphology, or microscopic roughness (on the order of angstroms), of the ceramic surface will affect the response of the tissue to the implant. Rough surfaces are generally more bioactive than smooth surfaces, but it has not yet been determined whether this behavior is due to the tendency of these surfaces to be more porous, thereby allowing greater bulk transport of ions, or if there is another less obvious mechanism involved. Since minimizing interfacial energy per unit area between the ceramic and the aqueous medium in contact with it is more difficult with a rough surface than a smooth surface[55], a macromolecule adsorbing to a rough high–energy surface must change its conformation more than would be required for adsorption to the equivalent smooth surface (if the rough surface is of sufficiently high energy to force this change). Therefore, molecules that act as signals for the inflammatory response may lose efficacy through such a conformation change, with the end result that the immune response will not occur to as great an extent as might otherwise be expected[54]. The effects of surface morphology on the response to implant systems are only beginning to be characterized.

Besides the surface properties of the ceramic itself, the response of the tissue to the implanted device should be briefly discussed. Such is the subject of the remainder of this section.

c) Tissue Considerations

The effect of an implanted biocompatible material on the tissue surrounding it varies between individuals, but some generalization as to expected tissue response may be made. In order for a given biomaterial to be useful, it must not have the potential to be rejected by the body. Thus, this material must not be recognized by the immune system as foreign, or

at least it must not trigger an adverse response by this system. Such a requirement for biocompatibility is referred to as the "self/nonself" behavior of a biomaterial, where a material is considered "self" if the immune system, in response to the injury caused by implantation, initiates repair without even noticing the presence of the implant. Clearly, this is an ideal property for a biomaterial to possess, but few materials exhibit such behavior. Conversely, most materials are quickly recognized by the body as "nonself" and rejected.

It is important to separate the subject of immune system response from that of inflammatory response, since the latter will always occur regardless of the biocompatibility of the implant. The immune response refers to a systemic response usually accompanied by a series of events that ultimately compromise the health of the patient (i.e. result in trauma). The inflammatory response, on the other hand, acts locally to the wound, rather than systemically, and aids in healing and tissue repair[56]. A local immune response may occur only insofar as to involve any immune cells in the immediate vicinity of the wound; however, no new cells are signalled for an increase in the response.

After insertion of an implant into a pre–formed cavity, a fluid–filled space between tissue and implant will exist. During repair of the injury due to implantation, fibroblasts will deposit collagen in this space and eventually form a dense fibrous coat around the implant, regardless of the type of tissue involved. This coat possesses low mechanical strength, so little force is required to loosen or dislodge the implant from its seat. Such loosening can impair bone growth around the implant (if such growth occurs), making adherence of bone to the implant surface difficult or even impossible[57].

A material that initially appears to be biocompatible may, over time, adversely affect the tissue surrounding it through slow release of toxic ions, via pitting and corrosion, into this tissue. The toxicity of their constituent metal ions precludes many ceramics from being

used as biomaterials, such that those which do not cause a toxic response are the exception rather than the rule. While most metals that comprise ceramic materials are naturally present in the body to some extent, there is generally some concentration of a given metal above which a toxic effect begins to take place. If the ions released by a ceramic were evenly distributed throughout the body, their concentration would not usually be high enough to exert an effect. However, these ions will either build up in the tissue adjacent to the implant, or they will reach the general circulation and concentrate in certain tissues. This results in a toxic level of metal being reached much more rapidly than would be expected using a one–compartment model for the body. There are many pathological conditions associated with metal ion toxicity.

Aluminum oxide has been called the most bioinert of all implant materials[58]. It is extremely resistant to corrosion, and does not appear to release aluminum ions into the surrounding tissue. Its *in vivo* behavior and applications will be considered next.

2. The Investigation of Ceramics

a) Background

The broad program of which this research was a part involves investigation of porous ceramic materials as alternatives to more popular polymeric delivery systems, which are the most widely investigated for drug delivery applications. Although polymeric materials possess several advantages in terms of flexibility, ease of manufacture, and versatility, ceramic materials can offer some advantages due to their very high tensile strength and good biocompatibility.

Oxide ceramics are employed extensively as structural materials in the human body[59], so a precedent exists for their use in the physiological environment. Physiological responses to different ceramic materials are thus well known from much clinical study of

ceramic implants. The high tensile strength of an oxide ceramic makes it attractive for such uses as bone and tooth replacements. Applications such as these require oxide ceramics that are very dense, since porosity will decrease the strength of the device.

Conversely, the *in vivo* behavior of porous ceramics has only recently begun to be investigated, and so is less well understood. Porous ceramics exhibit behavior *in vivo* that is much different from that shown by dense ceramics. Bone tissue has been demonstrated[60] to actually grow, by an unknown mechanism, into very large pores (> 100 μm diameter) in some ceramics, implying that a porous ceramic may take a more active role in the reaction of the surrounding tissue to the material. A porous delivery device may be able to take advantage of this effect, perhaps as a way to anchor the device to the tissue in which it is implanted. Since such a device would require large pores, it is the intent of the finite-size scaling study described previously to show that release from this device could also be successfully modeled using percolation theory. It would be important for such a device to be designed with properties that would inhibit growth of bone into all the pores of the device, thus inhibiting transport.

As noted previously, a fibrous tissue capsule can be formed around a dense ceramic implant by fibroblasts, which may occur because the surface of such an implant is typically highly polished. Such a capsule would be detrimental to the ability of a ceramic device to release a drug. However, recent research has shown that such a response does not occur if the ceramic material contains large pores. It is unknown why formation of a tissue capsule is not observed with a porous implant, but it is possible that migration of fibroblasts over the device surface is hindered by the pore structure. Whether or not a tissue coat would form around an oxide ceramic containing small pores (about 1 μm in diameter) such as made in the majority of this research is unclear, since the surfaces of these devices are very rough, and surface roughness may also play a part in formation of a tissue coat.

A particular disadvantage of an implant made from aluminum oxide is that, since Al_2O_3 is bioinert, once its usefulness has ended it must be surgically removed from the body. The phosphate ceramics hydroxyapatite and tricalcium phosphate have been studied in our laboratory as potential drug release devices that may avoid this problem. These materials are examples of bioactive ceramics. The phosphate groups in these materials promote dissolution by the same mechanisms that control bone resorption, so devices made from these materials will be resorbed by the body over time. Although phosphate ceramics are not nearly as strong as oxides, that a phosphate-based device does not have to be surgically removed after it has released its entire drug load makes such a device extremely attractive for use in or near hard tissues.

Even with this one major disadvantage, the bioinertness of Al_2O_3 is what makes it attractive as a material for construction of porous delivery devices. Why the alumina matrix is bioinert is not definitely known, but it is thought that three properties are primarily responsible for this behavior. First, the alumina molecule does not dissociate to any noticeable degree at physiological pH or temperature, as given by its dissociation constant in Table 1.2. This stability directly results both in good corrosion resistance of the ceramic, and also in no build-up of aluminum ions in the surrounding tissue. Second, the low conductivity of the alumina crystal, as reflected in its low dielectric constant, implies that there is little tendency for a potential gradient to form between the implant and its surroundings. The generation of such a potential difference has been postulated to be a possible initiator of the immune response. Third, the layer of water molecules bound to the alumina matrix shields the surrounding tissue from the high-energy ceramic surface and decreases the apparent surface tension of the material, such that no potential exists for the material to disrupt its surroundings. These points also illustrate the advantages that an oxide ceramic has over a polymeric material, since most polymers have been observed to

provoke some form of immune response.

Limited precedent does exist for the use of ceramics as drug delivery devices. For example, ceramic carriers have been used to deliver sustained doses of antibiotics to farm animals; however, they have not yet been applied (as far as is known) in a similar capacity in humans. Thus, many applications and forms may be imagined for a ceramic release device[61]; the three that were envisioned when this research was undertaken will be summarized next.

b) Intended Applications of Alumina Ceramics

The model ceramic matrix made in this work has the general appearance and dimensions of a disk. This shape was chosen primarily for the convenience with which it could be manufactured, but also because it was assumed that finite size effects would not be significant at the thickness used. Also, the concentration gradient of benzoic acid, the model drug molecule used in this study, across a matrix of this shape could be described using a membrane transport model, as will be discussed in the next chapter. (It was assumed that no partitioning of benzoic acid into the matrix occurred at steady-state.)

The transport mechanism through the ceramic disk is equivalent to that in a reservoir release device. In such an application, solid drug is first packed into a pre-formed porous ceramic holder, such as a hollow cylinder, which is then sealed shut and implanted. Fluid enters the reservoir through the pores of the ceramic and solubilizes the drug, which then diffuses out of the device as a saturated solution. Release of the drug, which will depend on both the porosity of the matrix and the saturation concentration of the drug, may then be modeled using percolation theory. It is thought that the release mechanism of a drug can be manipulated by varying the pore structure of the device. Alumina reservoir devices are intended for use in or near areas of hard tissue, so as to ensure that no damage to soft tissue

occurs due to the presence of a hard foreign body.

Although it is not possible to do so before final processing of the matrix, drug molecules may be dispersed in the pores of a ceramic by first permeating the matrix with a solution of drug and then drying in some manner, perhaps by lyophilization. The pore structure of the matrix and the solubility of the drug will again dictate the release behavior of the device. This type of device may benefit from a large pore structure, since it will aid in drug dispersion and also may possibly promote anchoring of the matrix to hard tissue.

Finally, ceramic matrices may be used to immobilize enzymes and/or act as filters for convective transport processes such as dialysis. Phosphate ceramics may be especially suited for immobilizing enzymes, since it may be possible to bind some enzymes to exposed phosphate groups on pore surfaces in these materials.

This section completes the presentation of background information needed to understand the motivation for this study and the manner in which it was performed. Chapter II next summarizes the experimental procedures and equipment used in this work.

II. MATERIALS AND EXPERIMENTAL METHODS

The experiments that were performed in this work fall into two general categories, in terms of both order and subject. The first category pertains to manufacturing and characterizing ceramic disks for use in percolation theory investigations, whereas the second concerns the procedures used in obtaining these parameters. Processing of ceramics must be considered first, so that the evaluation of percolation quantities may be understood more thoroughly later.

A. Ceramic Processing

1. MATERIALS

The ceramic disks made in this investigation were composed of aluminum oxide (99.8%, lot #00521PM, Aldrich Chemical Co., Milwaukee, WI), along with 0.5% by weight magnesium oxide (99.5%, lot #H11G, Morton Thiokol Inc., Alfa Products, Danvers, MA) which was added to inhibit grain growth in the compact during sintering. Also, poly(vinyl pyrrolidone) (PVP) (lot #G707, GAF Corp., Wayne, NJ) of average molecular weight 10,000 daltons was used as a binder to hold the ceramic compacts together before sintering. Typical dry powder batches weighed 100 grams total, so if a powder mixture was to contain 10% ($^{w}/_{w}$) PVP and 0.5% ($^{w}/_{w}$) MgO, it would consist of 10 grams PVP, 0.45 grams MgO, and 89.55 grams Al_2O_3. Note ($^{w}/_{w}$) denotes the ratio of weight of the particular component to weight of the total powder mixture. The size and shape of a typical disk made in this work are shown in Figure 2.1.

The Aldrich alumina powder used in this investigation was polydisperse, with a nominal diameter range (given by Aldrich) of 1-10 μm. To judge the relative processing properties of this powder as compared to a more monodisperse powder, a sample of 99.7%

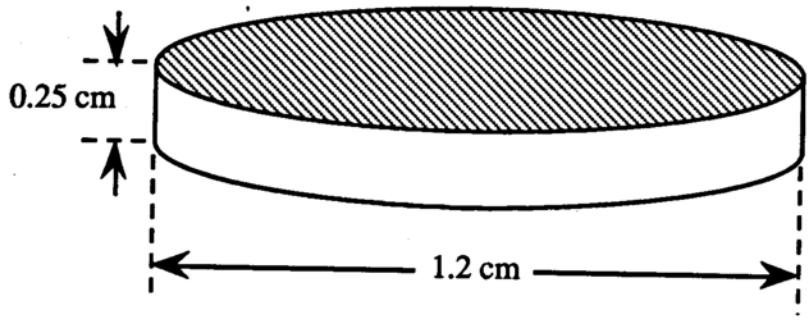

Figure 2.1. Appearance of an alumina disk as made in this research.

purity, 0.5 μm diameter, monodisperse Realox alumina powder, lot #XA-1000, was obtained from Alcoa Chemicals Inc. (Pittsburgh, PA) and its densification behavior was compared with that of samples of Aldrich alumina. Both of these powders were processed in the manner to be discussed next.

The first portion of this work involved varying several processing conditions in order to determine how these factors influenced the final porosities of the manufactured disks. The values investigated for the most important of these parameters may be summarized as follows:

1. Compaction pressures: 1000, 2500, 5000, 7500, and 10,000 psig;
2. Sintering times: 1, 2, 4, 8, 12, 24, and 36 hours;
3. Sintering temperatures: 1450, 1500, 1550, 1600, and 1670°C;
4. % ($^{w}/_{w}$) PVP used: 5, 10, 15, and 20%.

The results of these studies will be discussed in Chapter III.

2. Ceramic Disk Fabrication

a) Powder Mixing

Al_2O_3, MgO, and PVP powders were each weighed out to the nearest 0.01 gram on a Sartorius electronic top loading laboratory balance model L420D, and were then combined with a large steel spatula on a piece of parchment paper. It was not necessary to dry the ceramic powders additionally prior to dry-mixing.

Two different methods were employed for final mixing of the powder mass in order to gauge the effect of the powder mixing technique on final disk porosity. In the first method, the powders were formed into a wet slurry in a shallow Pyrex petri dish by addition of enough distilled deionized water (Sybron-Barnstead, Boston MA) to completely wet the mixture, which was then stirred for five minutes using a small rubber policeman. The

slurry was covered and allowed to settle for 24 hours, stirred again, and then placed in a Precision Scientific Co. model 10 vacuum oven (#31545) (fitted with a Precision model DD-20 vacuum pump) and dried at 12.28 psig vacuum and 65°C for one hour. The temperature in the oven was then raised to 110°C for one hour, after which time the powder cake was removed and broken up. More complete drying was achieved by returning the broken-up powder cake to the oven at 12.28 psig vacuum and 110°C for a half hour longer. The dried chunks of powder cake were then pulverized in a porcelain mortar and pestle and stored in an airtight glass jar until use.

The second method of mixing the powders was ball-milling. Only Aldrich powder batches were ball-milled. In this procedure, the powders were poured into a U.S. Stoneware 0.30 gallon porcelain mill jar containing twelve $^{13}/_{16}$" long x $^{13}/_{16}$" diameter U.S. Stoneware porcelain cylinders for size reduction. The jar was then sealed, mounted on a Lortone model QT66 rotary tumbler, and tumbled at approximately 60 rpm for 24 hours. The tumbler was stopped every four hours to scrape away the powder that had adhered to the sides of the jar. Heating of the contents of the crucible was not observed to occur during tumbling. Water was not used in this method.

The powder mixture was removed from the crucible after tumbling, poured into a glass petri dish, dried following the same procedure as given above, and stored in an airtight glass jar until use. The processing parameters listed above were studied with powders mixed using both methods, but percolation parameters were determined using disks made with wet-mixed powders only since disks made in this manner were found to be easier to handle and more resistant to breakage.

b) Powder Compaction

The next step in disk manufacture was compression of the dried powder mixture into a

compact disk shape (commonly referred to as a green piece). Powders were compressed in a Carver model C laboratory press in which pressure was applied uniaxially to the top of the sample. Most disks were made using a pressure of 10,000 psi. A type 308 stainless steel tablet punch was used to compress the powder mixture. This punch was fabricated by the machine shop in the University of Wisconsin Department of Physics, and is shown in Figure 2.2.

To make a compact, a powder sample weighing 0.6 - 0.7 grams (weighed on the Sartorius balance) was poured into the barrel of the tablet punch, on top of the bottom die. The top die was then placed on top of the powder and pressed down with the plunger. The assembly was next placed on the lower plate of the Carver press, which was raised (by hand pumping) until the plunger of the punch met the upper plate of the press. Further pumping caused compaction of the powder to occur (the applied compaction pressure could be observed by a gauge attached to the press). Once the desired compaction pressure was reached, it was released immediately and the tablet punch was removed from the press.

To remove the compact from the punch barrel, the assembly was inverted and placed on the bottom plate of the press. The press was then pumped up until the assembly touched the upper plate of the press, and then slowly pumped further until the compact was gently forced from the barrel. The compacts were then carefully weighed in a Mettler balance (to the nearest 0.0001 gram) and stored in a glass petri dish.

c) Pre-Firing of Compacts

The next phase in fabrication of the final product involves pre-firing, or baking, of the compacts at low temperature to remove water, volatile impurities, and the PVP binder. This step was performed in a Lindberg model 51848 1100°C Moldatherm box furnace, lined with alumina firebrick. This furnace was used because it is easier to control at low

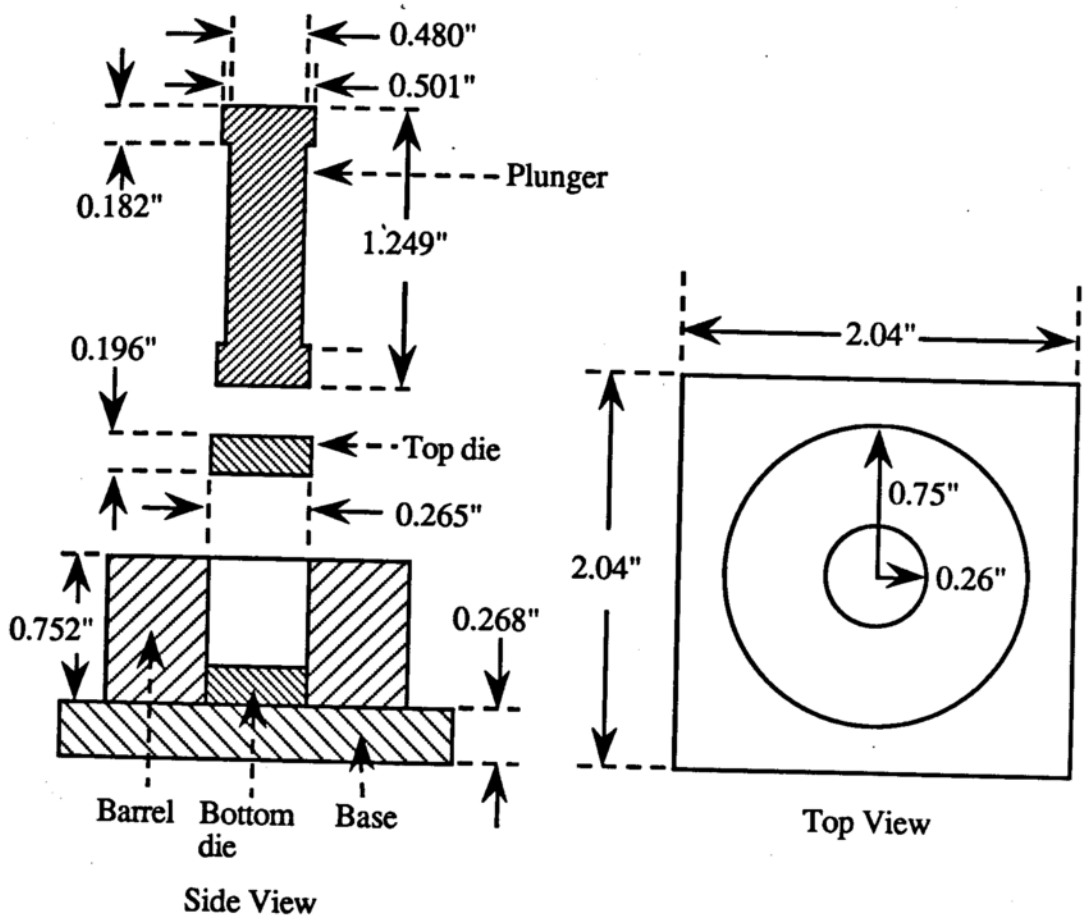

Figure 2.2. Type 308 stainless steel tablet punch.
(Figure not to scale.)

temperatures than is a furnace designed to operate at high temperatures. Also, the operating life of the high-temperature furnace is diminished by prolonged use at high temperatures.

The heating schedule used to pre-fire the compacts was as follows:

1. 120°C for 1 hour;
2. 250°C for 30 minutes;
3. 400°C for 30 minutes;
4. 700°C for 30 minutes;
5. 1100°C for 2 hours;
6. Cool to room temperature.

The furnace required about 3 minutes to reach the next higher temperature. Once the compacts had cooled to room temperature, they were carefully removed from the oven, weighed, and stored in a glass petri dish.

This schedule, as well as that to be given for high-temperature firing, was designed to achieve thermal equilibrium in the compact before subsequent increase of temperature.

d) Sintering of Compacts

The compacts are next fired at high temperature in order to produce sintering, as described in the previous chapter. The furnace employed in this step was a Lindberg model 51314 1700°C box furnace, an ambient-atmosphere furnace lined with alumina firebrick. This furnace uses six molybdenum disilicide elements suspended on the sides of the heating chamber.

In the sintering step, the pre-fired compacts were first placed on an alumina plate on the bottom of the furnace. The following heating schedule was then observed (a manual controller was used with this furnace, so the temperature was increased in steps, with the heating time between each step being about 2 minutes):

1. 250°C for 30 minutes;
2. 500°C for 30 minutes;
3. 750°C for 30 minutes;
4. 1000°C for 30 minutes;
5. 1250°C for 30 minutes;
6. 1400°C for 30 minutes;
7. 1550°C for 30 minutes;
8. 1650°C for 15 minutes;
9. 1670°C from 1 to 36 hours;
10. 1300°C for 1 hour;
11. Cool to room temperature.

Once the furnace was turned off at the end of Step 10, room temperature was reached after about 4 or 5 hours. Most disks used in this research were sintered at 1670°C.

In the above schedule, the maximum temperature was achieved as quickly as possible in order to minimize contribution of lower temperatures to the overall densification process. Cooling occurred in two stages to minimize the potential for disk cracking due to thermal stress. (Cooling from 1300°C to room temperature took four to five hours). After removal from the furnace, the disks were stored in scintillation vials (VWR Scientific Co.) marked with information about the processing parameters of the disks.

A high-temperature furnace (Thermolyne Type 46100) with a programmable controller was used in one study to estimate the effect of the heating rate (ramping) on the final disk porosity. This furnace is maintained in the Department of Water Chemistry at the University of Wisconsin, and also has a maximum temperature of 1700°C. This furnace was used in the study that compared the properties of polydisperse Aldrich Al_2O_3 disks to the properties of disks made with monodisperse Alcoa Al_2O_3 powder, since sintering of

Alcoa compacts should occur at lower temperature (because of small particle size) than Aldrich compacts. This study investigated the effects of ramping rate (from 5 to 30 $^{\circ}C/_{min}$), maximum sintering temperature (from 1450 to 1670°C), and sintering time (from 1 to 12 hours) on the final porosity.

e) Disk Handling and Cleaning

After firing, the ceramic disks were washed to remove loose inorganic impurities by bathing in approximately 5 ml of denatured HPLC grade ethyl alcohol (lot #05103BW, Aldrich) and were sonicated for 5 minutes in an American Brand Ultrasonic Cleaner. Washed disks were then dried in the low-temperature furnace for 30 minutes at 750°C. Finally, the disks were weighed on the Mettler balance and returned to scintillation vials.

f) Total Porosity Determinations

The total porosity of a disk is very difficult to determine accurately, since it depends on the bulk, or dimensional, volume of the disk. Since disks do not shrink uniformly through their volumes, the surfaces of a fired disk are typically not parallel, and thus the disk thickness is difficult to measure with a micrometer. All disks made over the course of this research were measured using a Vernier caliper (Mitutoyo) to measure the average disk diameter (to the nearest 0.002 cm), and a micrometer (Enco) to measure the average disk thickness (to the nearest 0.001 cm). The last two studies in this work compared the volumes obtained by dimensional measurement to those obtained by an alternative method for determining the total volume of a disk, which utilized the Archimedes principle of buoyancy of a solid in a liquid[62].

To determine total porosity using dimension measurements, the bulk density of the disk was calculated as follows:

$$\rho_{bulk} = \frac{M_{disk}}{l\frac{\pi d^2}{4}}\ ; \qquad (2.1)$$

where ρ_{bulk} is the bulk density of the disk (g/cm^3), M_{disk} is the dry weight of the disk, l is the average disk thickness, and d is the average disk diameter. (The diameter and thickness are each taken as the average of five measurements on a given disk.) The total porosity may then be calculated:

$$\emptyset = 1 - \frac{\rho_{bulk}}{\rho_{theor}}\ ; \qquad (2.2)$$

where ρ_{theor} is the theoretical density of Al_2O_3 (assumed to be 4.0 g/cm^3 in this work), and $\emptyset$ is the total disk porosity.

Alternatively, ρ_{bulk} may be obtained by measuring the buoyant weight of a disk. Buoyancy measurement is not often used for porous solids, since the suspending liquid (normally water) can enter the pore space. This gives an abnormally low volume reading for the disk, because the liquid drains out of the pores and is not accounted for when the solid is removed from the liquid. In this work, however, an 86% by weight glycerol/water solution[1] is used to perform the buoyancy measurement . In this method, the liquid enters the pores of the disk, but possesses a viscosity that is too high for it to drain out of the pores once the disk is removed from the liquid. The imbibed liquid may thus be accounted for when the sample is weighed after removal from the liquid , so that a correction can be made to the observed weight of the sample. This procedure was used without modification in this study.

Disk densities were determined by the above technique with a Mettler density kit

(model 33340) designed for use with both solids and liquids. This kit includes a calibrated glass sinker for determining liquid density, and a suspension basket for determining solid density. The basket (or sinker) is suspended from a wire frame that is attached to the weighing tray of the Mettler balance. The basket then hangs down into a 250 ml beaker that rests on a beaker stand that spans the balance tray between the two arms of the wire frame. A small thermometer is also provided to measure the liquid temperature. This apparatus, as set up for measurement of solid densities, appears in Figure 2.3.

The sinker provided for liquid density measurement was first suspended from the wire frame down into the empty beaker, and its weight recorded to the nearest 0.0001 gram. A solution of approximately 86% ($^{w}/_{w}$) glycerol/water was then poured into the beaker so that the top of the sinker was at least one centimeter below the surface of the liquid (about 200 ml of liquid was required). The glycerol used was 99.5+%, spectrophotometric grade, lot #05902 (Aldrich). After making sure that no air bubbles had adhered to the sinker or its suspension wire, the buoyant weight of the sinker was recorded, and the liquid temperature (to the nearest 0.5°C) noted. The liquid density was then calculated using equation (2.3),

$$\rho_l = \frac{M_1 - M_2}{10} + 0.001 \frac{g}{cm^3}; \qquad (2.3)$$

where M_1 is the dry weight of the sinker, M_2 is its buoyant weight, and ρ_l is the resultant liquid density. (The correction of 0.001 $^{g}/_{cm^3}$ is needed to account for the volume taken up by the suspension wire.) The sinker was then removed from the beaker and cleaned.

To measure disk densities, the suspension basket was first immersed in the glycerol solution and any bubbles were shaken off. A batch of ceramic disks (usually five to a batch) was next placed in the submerged basket and allowed to imbibe solution until no further weight change was noted. The disks were then removed, and the excess solution

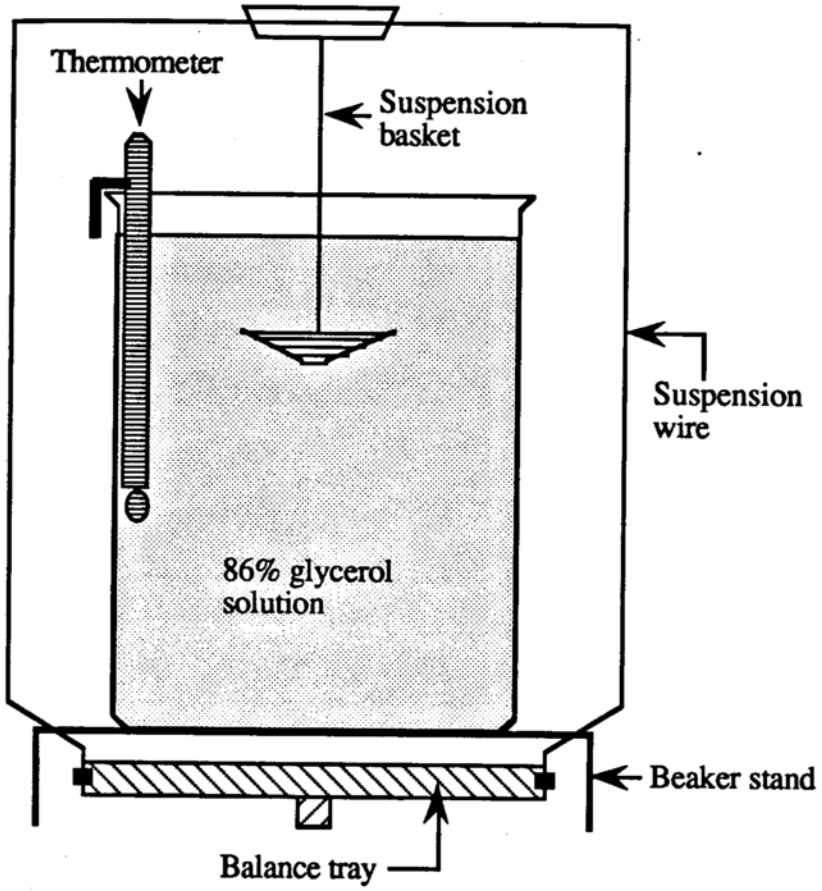

Figure 2.3. The assembled Mettler density kit (showing the basket used for measurement of solid densities).

wiped off with Kimwipes. The density of a disk was then measured by placing the disk in the submerged basket (checking for bubbles), recording its buoyant weight, and then removing the disk and wiping off the excess solution. This portion of the process is operator-biased, since different users will wipe off different amounts of liquid. In this particular case, disks were wiped until no shiny spots of liquid could be seen on the disk surface (reproducible results could be obtained using this criterion). The wiped disk was next placed in the upper tray of the suspension basket and its final weight recorded. The bulk density of the disk was then calculated:

$$\rho_{bulk} = \rho_l \left(\frac{M_{disk}}{M_3 - M_2} \right) ; \qquad (2.4)$$

where M_{disk} is the dry weight of the disk, M_3 is the weight of the disk plus the weight of imbibed solution, and M_2 is the buoyant weight of the disk. Five density determinations were performed on each disk, and an average and standard error (95% confidence limits) calculated. The total porosity of each disk was then determined using this average in equation (2.2).

Those disks measured in the above manner were dried in the low-temperature furnace at 750°C for 30 minutes to remove the glycerol solution from the pores of the disks. Disks were then weighed and returned to their scintillation vials.

This concludes the discussion of the procedures employed in manufacturing and characterizing the ceramic disks. Next, the methods involved in estimating percolation parameters presented in Chapter I will be discussed.

B. Percolation Theory Investigations

1. MICROSTRUCTURAL PROPERTIES

Characterization of disk microstructures is necessary to estimate the percolation parameters volume fraction isolated ($\emptyset^I$) and volume fraction accessible ($\emptyset^A$), which depend solely on disk morphology. The technique of pycnometry was used to determine the fraction of total disk volume occupied by the solid plus the fraction taken up by the isolated pore space, whereas that of mercury porosimetry was used to estimate the pore size distribution within the disk. These methods, taken together, form a qualitative picture of the disk interior and its accessible and isolated pore spaces.

a) Helium Pycnometry

Helium pycnometry may be used to estimate the volume fraction isolated, and the amount of disk volume taken up by solid, by measuring the drop in pressure of a reference volume of helium that is introduced into a cell containing a sample of known bulk volume. Helium molecules are assumed to fill the accessible pore space within the bulk volume of the sample, thereby removing this space from the final observed volume. Using the ideal gas law, the unknown volume V_s of the disk batch may be calculated as follows:

$$V_s = V_{cell} - V_{ref}\left[\frac{p_1}{p_2} - 1\right] ; \qquad (2.5)$$

where V_{cell} and V_{ref} are the calibrated sample cell and reference cell volumes, respectively, p_1 is the original reference cell pressure, and p_2 is the final pressure of the reference cell plus the sample cell. Note that p_1 and p_2 are the values measured in the experiment. The derivation of this equation appears in Appendix A.

A Quantachrome Multipycnometer model MVP-1 helium pycnometer with a micro

sample cell was employed in this investigation. Helium was obtained from Badger Welding Supplies, Inc. (Madison, WI). The pycnometer was calibrated (to determine V_{cell} and V_{ref}) at the beginning of the experiments using a steel reference slug of known volume (V_{slug} = 2.355 cm^3). V_{ref} and V_{cell} were typically about 5.4 cm^3 and 13.4 cm^3, respectively.

Figure 2.4(a) illustrates the setting of the pycnometer under which the reference cell pressure p_1 is obtained. To determine this pressure, the disks are enclosed in the sample cell and the pycnometer is purged with helium for 15 minutes (the three valves shown are open during purging). The inlet valve is then closed, and the system pressure (digitally displayed to the nearest 0.001 psig) allowed to fall to zero psig. To measure sample volume, the center and outlet valves are closed, and the pressure display zeroed. The gas inlet valve is then opened, pressurizing the reference cell with helium. Once a pressure between 15 and 20 psig is reached, the inlet valve is closed and the pressure (p_1) recorded. The center valve is then opened, which allows helium to flow into the sample cell as shown in Figure 2.4(b). Distribution of helium causes the system pressure to fall to p_2, a pressure equivalent to the reference cell volume plus the sample cell volume, but minus the (unknown) true sample volume. The outlet valve is then opened and the system pressure allowed to fall to zero psig for the next measurement. Finally, V_s is calculated from p_1 and p_2 using equation (2.5).

Ten useful (p_1, p_2) data pairs were typically obtained for each disk batch, and an average and standard error calculated for V_s. After each trial, V_s was calculated to check for reproducibility A standard error no greater than 1% of the final batch volume was typically desired.

The average value of V_s for a disk batch may be used to calculate the volume fraction isolated:

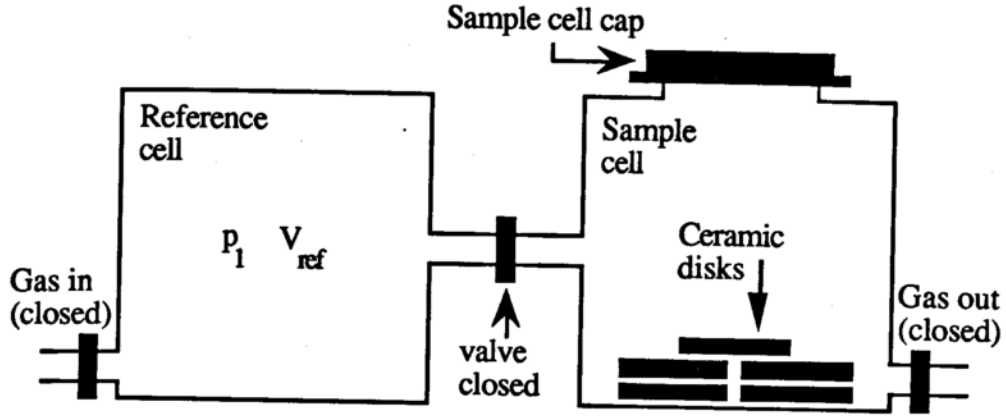

Figure 2.4(a). Helium pycnometer, reference cell pressurized.

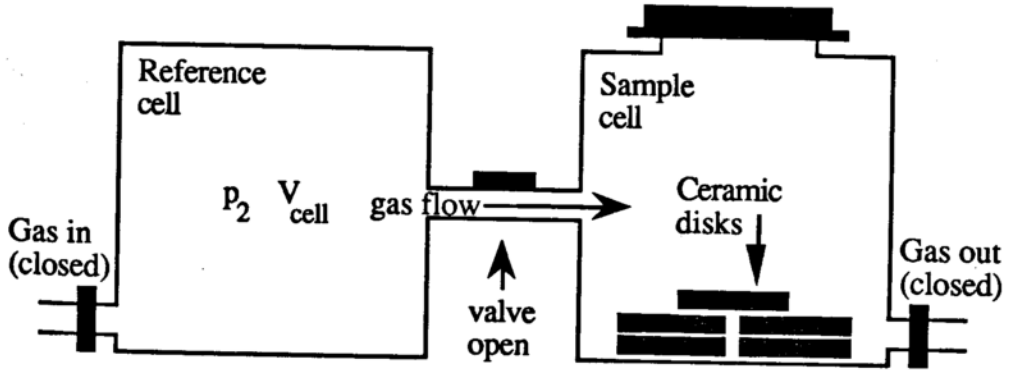

Figure 2.4(b). Helium pycnometer, reference and sample cells pressurized.

$$\emptyset^I = \frac{V_s}{V_t} - (1 - \emptyset) \; ; \tag{2.6}$$

where V_t is the total bulk volume of the disk batch and $\emptyset$ is its average total porosity. The derivation of this equation is also given in Appendix A. Replacing $\emptyset^I$ in equation (1.16) with equation (2.6) then results in:

$$1 = \frac{V_S}{V_t} + \emptyset^S + \emptyset^A \; . \tag{2.7}$$

$\emptyset^A$ is zero below the critical percolation threshold ($\emptyset_c$), so for $\emptyset \leq \emptyset_c$ the following relationship holds:

$$\emptyset^S = 1 - \frac{V_s}{V_t} \; ; \tag{2.8}$$

may be obtained for the surface porosity. Unfortunately, as discussed in Chapter I, no similar simple relationship may be obtained when $\emptyset > \emptyset_c$.

b) Aqueous Pycnometry

Aqueous pycnometry is similar to helium pycnometry in principle, but differs in that purified water is used to fill the accessible pore space in order to determine V_s. This unknown sample volume may be obtained as follows:

$$V_s = V_{cell} - \frac{(M_{total} - M_{cell} - M_{dry})}{\rho_{H_2O}} \; ; \tag{2.9}$$

where M_{total} is the total weight (cell plus water plus disks), M_{cell} is the dry cell weight,

M_{dry} is the dry weight of the disk batch, V_{cell} is the total cell volume, and ρ_{H2O} is the density of water at the experimental temperature. The aqueous pycnometry cell, a Kimax Hubbard specific gravity bottle with top hole diameter 1.6 mm and total capacity about 24 ml, appears in Figure 2.5.

In these experiments, the disks were placed in about 15 ml of water in the pycnometry cell, sonicated for one half hour, allowed to equilibrate overnight, sonicated for a half hour longer, and then washed twice with fresh water. The cell was next filled to the rim with water (typically at 22 - 25°C) such that excess water flowed out through the hole in the cell top. Excess water was wiped from the cap and the cell was then immersed (to just below the rim) in a MGW-Lauda model M3 circulating water bath set at 35.0 ± 0.1°C. Expansion of water out of the cell through the hole in the cap then occurred until the the cell water reached the bath temperature, at which point a stable meniscus formed at the rim of the hole. A 35°C water bath was used in order to ensure that the cell water would expand through the top hole. The cell was then removed from the bath, quickly dried with paper towels, and weighed (to determine M_{total}) in the Mettler balance. After weighing, approximately three-fourths of the water was poured from the cell, which was then refilled. The above procedure was then repeated. Six measurements of M_{total} were made on each disk batch and an average and standard error determined. The disks were then dried in the low temperature furnace at 750°C for 15 minutes and re-weighed to check for weight loss as a result of the experiment. The cell was calibrated (to determine V_{cell}) using the same procedure as that given above for disk volume determination, but with the cell containing only water. Ten measurements of empty cell volume were made to estimate an average and standard error for V_{cell}.

Drying and weighing of the pycnometer cell are operator-biased (and thus prone to large systematic error) for two reasons: First, the cell might not be dried to the same extent

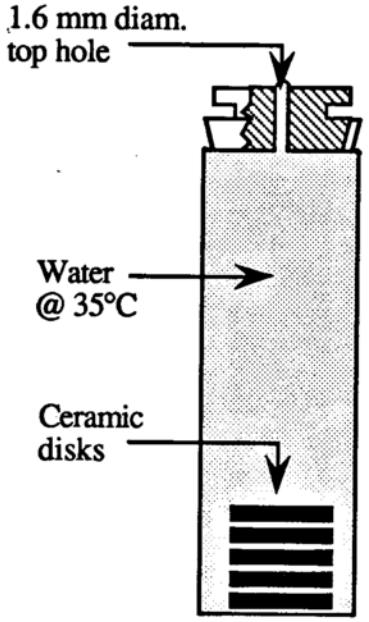

Figure 2.5. The aqueous pycnometry cell.

after each measurement; and second, using a higher bath temperature results in some water evaporating through the cap hole before the cell can be weighed, thus giving an artificially low weight. The magnitude of the latter error depends on how quickly the cell is weighed after removal from the bath.

Aqueous pycnometry was found to be more labor-intensive and prone to systematic error than helium pycnometry. This technique was only used in one study, since results obtained from it were unreliable. However, these results did allow insight into the structural stability of the disk microstructure. The uncertainties associated with this method will be reviewed in Chapter IV.

c) Mercury Porosimetry

Mercury porosimetry is used to determine the pore size distribution, and in some cases the specific surface area, of a porous sample. This sample is placed in a glass cell that is evacuated, purged with nitrogen, re-evacuated, and filled with a known volume of mercury, which due to its extremely high surface tension will not enter the sample pores under atmospheric pressure. A calibrated electrode at the closed end of the cell monitors the mercury volume, with zero being that volume at which the cell is filled with mercury, but no external pressure has been applied. Mercury is then forced into the sample pores by applying pressure to the open end of the sample cell using nitrogen. As the pressure increases, more mercury is forced from the bulk volume into the sample, thus decreasing the mercury volume detected by the electrode. The pore diameter accessible to mercury is a function of the applied pressure, with the smallest pore size accessible being limited by the maximum pressure capability of the instrument and the resisting pressure of any trapped gas in dead-end pores. The decrease in volume of mercury in the cell as a function of applied pressure ($^{dV}/_{d(logp)}$) is related to that fraction of total pore space made up of the

smallest pores into which mercury can enter at that pressure. Thus, if the cell is pressurized (scanned) from zero to maximum applied pressure a representative pore size distribution for the sample may be obtained. The sample is destroyed by this technique.

The specific surface area of a sample (in m^2/gram) may also be obtained from $dV/d(\log p)$ data, but this information is not useful in the present study. The morphological model most often used to obtain the specific surface area assumes that the pore structure consists of parallel bundles of cylinders[63], which is an unrealistic model for this system. Thus, this type of information will not be reported.

Porosimeters are available which operate mainly at low applied pressure (up to 300 psia), or at much higher pressures (up to 30,000 psia). Low pressure instruments can detect pores down to 0.7 μm diameter, while high pressure instruments can access pores as small as 0.007 μm. High pressure instruments are infrequently used, since samples with very small pores are usually analyzed by Brunauer-Emmet-Teller surface area analysis. Since it was uncertain what the pore size distributions of the finished Al_2O_3 disks would be, representative samples were sent to Porous Materials, Inc., Ithaca, NY, an analysis service specializing in materials analysis that manufactures a high pressure porosimeter with a maximum rated pressure of 30,000 psia. Samples of five disks each were analyzed using this instrument.

$dV/d(\log p)$ data cannot account for the diameters of the bulbous pores that typically occur in a complicated pore morphology, because the diameters of the necks between these bulbs dictate the pressure required to force mercury into the sample. Thus, the results obtained by porosimetry are only qualitatively useful. However, the method yields a suitable picture of the volume fractions and relative diameters of the pores that are important in transport through the disk, as will be discussed in Chapter IV.

d) Scanning Electron Microscopy

A two-dimensional picture of the pore morphology of a fired ceramic disk may be obtained through the use of a Scanning Electron Microscope (SEM) to take electron images of regions of the disk surface and interior. The instrument used was a Jeol model JSM 35-C Scanning Electron Microscope, with magnification range 0 to 99,000 X, which is maintained by the Materials Science Group in the College of Engineering at the University of Wisconsin. Disks analyzed using the SEM were first fixed to steel sample mounts, sputtered with an approximately 100 angstrom thick layer of gold, placed in a sample holder, and inserted into the SEM gun chamber for viewing and photographing. The magnifications used in sample viewing, 1000, 3300, 5000, and 10,000 X, gave resolvable surface features from 10 μm (at 1000 X) to 1 μm (at 10,000 X). The film used was Polaroid type 55 instant film.

A disk was prepared for SEM viewing by cutting away a wedge of surface to expose the interior, to determine differences in the internal and surface morphologies. Disk cutting was performed in the Department of Water Chemistry on a Buehler-Isomet model 11-1180 low speed saw with a diamond wafer blade. Approximately one-fourth of the disk was cut away, and the disk was then cleaned by sonication in ethanol for 15 minutes and dried in the low-temperature furnace before mounting. A cut disk is illustrated in Figure 2.6.

The SEM is the best means available for determining the actual two-dimensional morphology of the disk. An extension of SEM work is serial sectioning, in which the pore structure may be reconstructed, and its volume determined, by cutting the disk into several thin slices, photographing each slice, and then lining up tracings of these photographs by three-dimensional reconstruction. This results in a very powerful means of obtaining the structural percolation parameters $\emptyset^I$ and $\emptyset^A$. However, due to the extreme hardness of Al_2O_3, and the very complicated internal morphology of the disks made in this

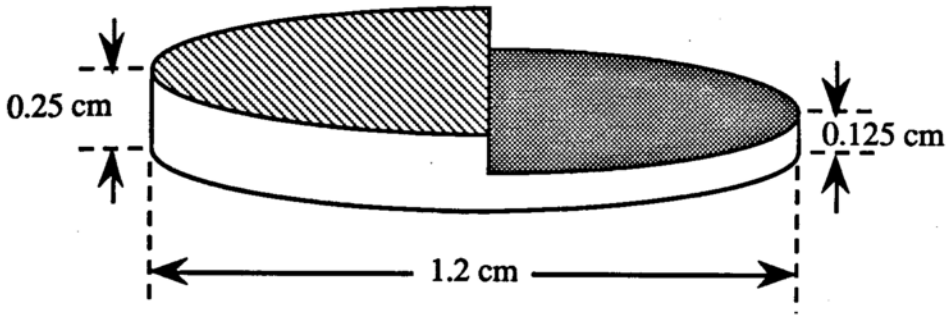

Figure 2.6. The sectioned alumina disk used in scanning electron microscopy.

investigation, it was determined that serial sectioning was not practical. Still, any picture of the internal structure can be used to estimate the coordination number of the pore structure for use in predicting $\emptyset_c$. Representative SEM photographs of the ceramic disks appear in the next chapter.

2. TRANSPORT PROPERTIES

The percolation parameter that depends on the permeability of the disk to small molecules is the volume fraction ($\emptyset^E$) of the total pore space that is utilized during steady-state transport. As discussed previously, equation (1.12),

$$\emptyset^E = \frac{D_B}{D_{aq}} \; ; \tag{1.12}$$

may be used to determine this quantity, where D_B is the bulk diffusivity of a molecule through the disk, and D_{aq} is the aqueous diffusivity of the molecule. D_B and D_{aq} are both values that may be experimentally determined, as is explained in this section.

a) Estimation of Volume Fraction Effective

The transport behavior of a porous disk may be modeled by treating the disk as a very thick membrane, so that the concepts of membrane transport may be applied to determine the bulk diffusion coefficient (D_B) of a model molecule through the pore structure. D_B in membranes is determined by means of the Stokes diaphragm cell, in which a chamber filled with solvent only is separated from one filled with a dilute solution of the model molecule by a membrane through which the solute flows due to a concentration gradient. The change in solute concentration in the sample chamber as a function of time at steady-state may be used to estimate D_B as shown[64],

$$D_B = \frac{1}{\beta t} \ln \left[\frac{(c_{bottom} - c_{top})^0}{(c_{bottom} - c_{top})^t} \right] ; \qquad (2.10)$$

where β is a constant that depends on the volumes of the cell compartments and the dimensions of the membrane, t is elapsed time at steady-state, c_{bottom} and c_{top} are bottom and top chamber solute concentrations, respectively, and t = 0 refers to the beginning of steady-state. This equation is derived in Appendix B.

A Stokes diaphragm cell as used in this investigation appears in Figure 2.7. The ceramic disk is mounted between two 1" square pieces of $^1/_4$" Lucite cast acrylic sheet (E.I. DuPont DeNemours Inc.), each having a $^3/_4$" diameter, $^1/_8$" deep depression drilled in one face for mounting a stoppered Kimax glass tube (VWR Scientific Co.), and a $^9/_{16}$" diameter, $^1/_{32}$" deep depression drilled in the other face for mounting the ceramic disk. A $^5/_{16}$" diameter hole is drilled through the center of each piece to expose 0.495 cm^2 of the disk surface. This mounting arrangement appears in Figure 2.8.

Glass tubes are mounted on the Lucite squares, and the ceramic disk mounted between them, using Torr-Seal low vapor pressure epoxy resin (Varian Inc.) as an adhesive and sealant. This adhesive sets in 24 hours. Torr-Seal was used because no partitioning of benzoate ion into it was expected to occur.

The diaphragm cell was next mounted vertically in a three-prong buret holder attached to a Talboys T-line laboratory stirrer (model 134-1, Talboys Engineering Co.). Its top chamber was filled with a phosphate buffer solution of 0.025M K_2HPO_4 (Aldrich, anhydrous, ACS reagent, lot #03420AW), and 0.025M KH_2PO_4 (Aldrich, 99%, ACS reagent, lot #03322KV), with pH typically 6.9. (pH values were obtained with an Orion Research model 501 digital ionalyzer equipped with a model 91-04 Ag/AgCl electrode.) This solution also contained 50 $\mu g/_{ml}$ 4-fluorobenzoic acid (FBA) (Aldrich, 99%, lot

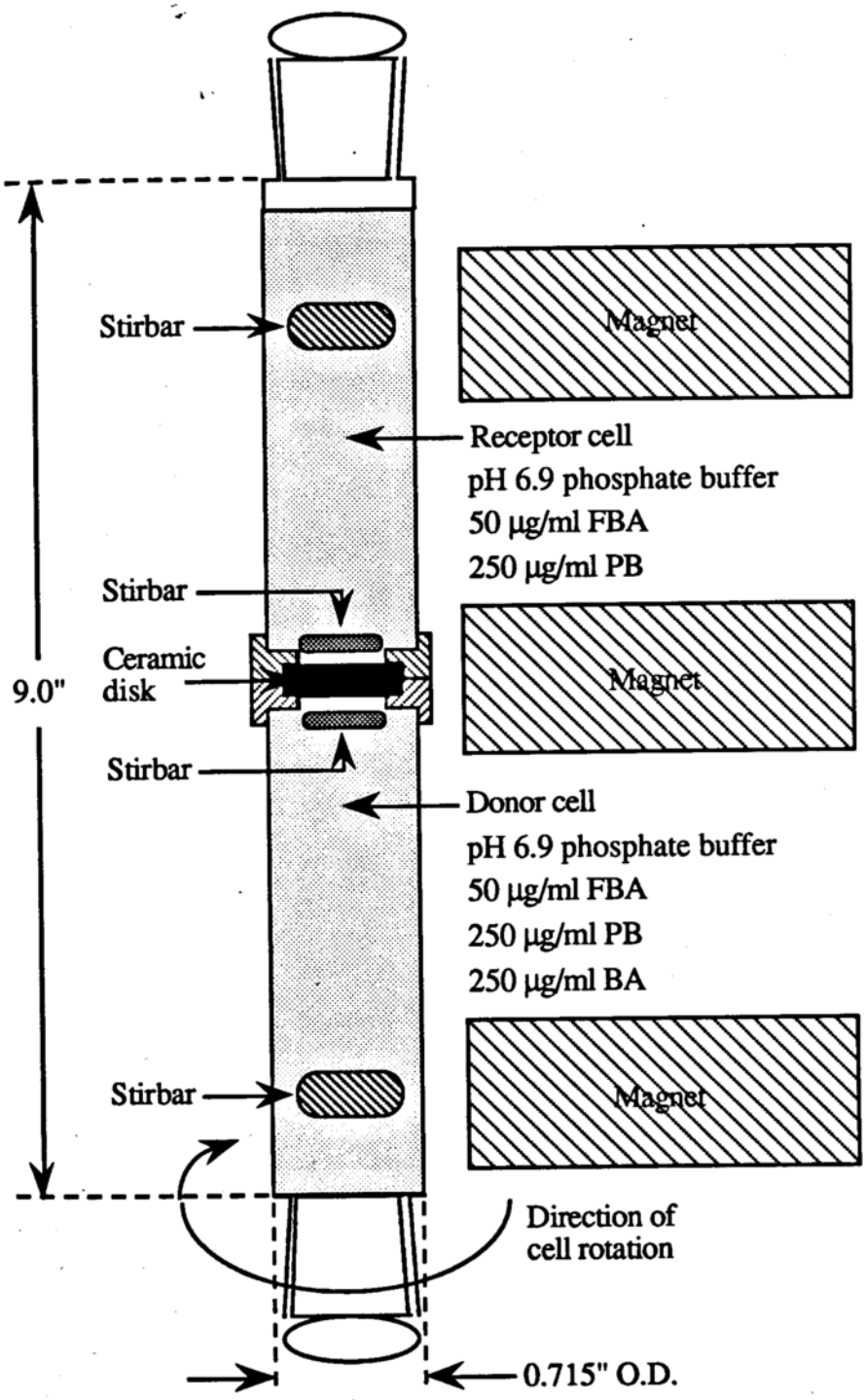

Figure 2.7 The Stokes diaphragm cell (receptor chamber on top).

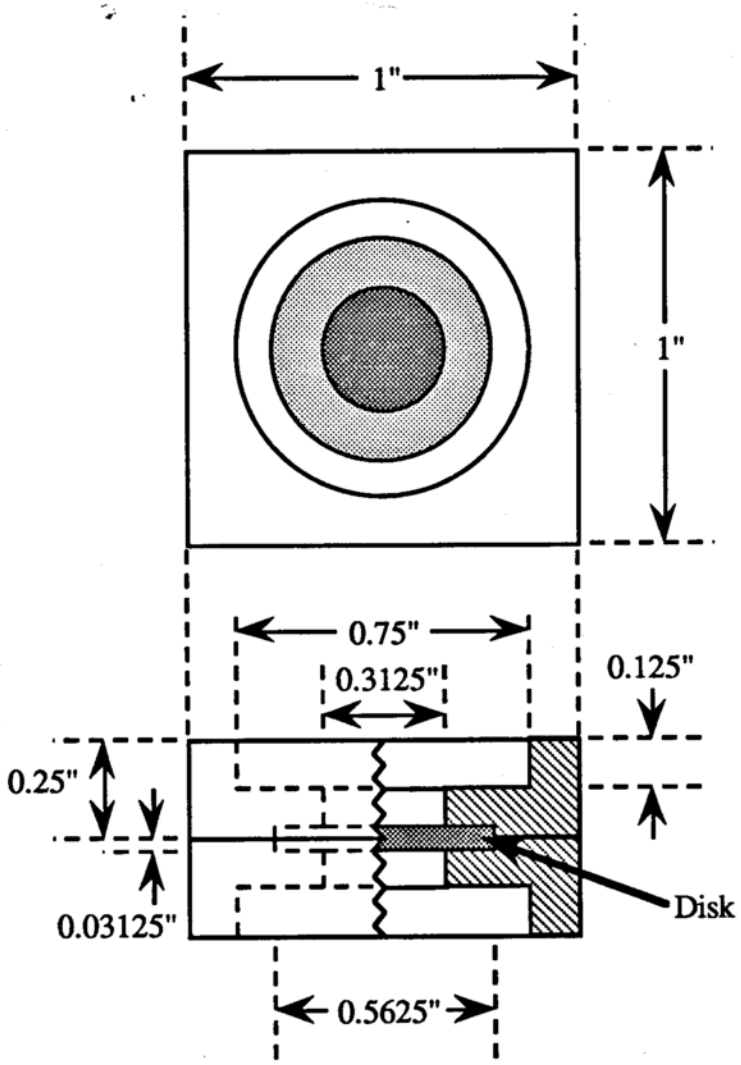

Figure 2.8. The disk mount used with the Stokes diaphragm cell.
(Figure not to scale.)

#02818BV), used as the internal standard for liquid chromatography, and 250 $\mu g/ml$ propyl 4-hydroxybenzoate (PB) (Aldrich, 99+%, lot #00712TM), used as a preservative[65]. This solution was allowed to drain through the disk into the empty bottom chamber for three days to saturate any sample-spanning pores with liquid. It was then taken down and emptied.

To determine D_B, one cell chamber was filled with the solution described above (becoming the receptor compartment), while the donor chamber was filled with this solution plus 250 $\mu g/ml$ benzoic acid (BA) (Aldrich, 99+%, ACS reagent, lot #10020LV), the model solute molecule used in this analysis. (Specific solution concentrations are listed in Appendix .) Both solutions were deaerated before use. The solutions in the cell compartments were of approximate pH 6.9, at which BA ($pK_a = 4.03$) is 99.9% ionized. This pH is a better model of that which a ceramic device would probably encounter *in vivo*. Hindrance of benzoate ion diffusion due to electrical interaction with the ceramic matrix was not expected to occur at steady-state.

Stirbars were inserted in the cell chambers after filling. The lower chamber was filled completely and checked carefully to ensure that no bubbles were present that could drift up and block contact of the solution with the disk, sealed, and the diaphragm cell mounted on the stirring motor. The lower chamber volume was typically about 18 ml. About 17 ml of solution was used in the upper compartment, since it was not necessary to fill this compartment completely. Three Alnico 5 maximum-pull horseshoe magnets were positioned on a rack next to the cell (as shown in Figure 2.5) to turn the stirbars. The cell itself was rotated at approximately 100 rpm by the stirring motor, thus achieving mixing by rotating the solutions around the stationary stirbars. The two small stirbars (VWRBrand, teflon, 10 mm x 3 mm, VWR) were positioned as close to the disk surfaces as possible in order to minimize boundary layer effects. The larger stirbars (Nalgene star-head magnetic,

$5/16$" x $3/8$", VWR) were used to stir the bulk solutions.

The high-performance liquid chromatography (HPLC) system used consisted of an Altex model 110A solvent pump set at a flow rate of 2.0 ml/min, a Rheodyne model 7125 sample injection module fitted with a 200 µl sample loop, a Waters Model 440 ultraviolet (UV) absorbance detector set at 0.05 absorbance units full scale and using a 254 nm wavelength lamp, and a Kipp and Zonen model BD40 linear chart recorder set at a speed of 5.0 mm/min. The columns used were a Beckman Ultrasphere ODS (5 µm, 4.6 mm x 25 cm, serial #9UE787) reversed-phase C18 column and a Beckman Ultrasphere ODS (5 µm, 4.6 mm x 4.5 cm, serial #7D14) matched precolumn. The mobile phase used in the analysis was composed (percentages by volume) of 54% H_20, 35% methanol (Baxter, spectrophotometric grade, lot #AW042), 10% acetonitrile (Aldrich, HPLC grade, lot #10201TW), and 1% acetic acid (Aldrich, 99.7+%, ACS reagent, lot #03210JT) to neutralize the benzoate ion. The mobile phase was deaerated before use.

The concentration of BA in the top chamber was analyzed by HPLC, once every three to five days, by withdrawing 0.50 µl of solution and diluting with approximately 1.0 ml of mobile phase. Column injections were made using a 500 µl Hamilton blunt-tipped syringe. The volume of solution removed was not replaced, but was corrected for in the calculation of c_{top} after each analysis. An output chromatogram consisted of the BA peak followed by the FBA peak (the internal standard). The height ratio of these two peaks, compared to that of a standard solution, gave the BA concentration of the top chamber, with the BA concentration in the bottom chamber obtained by mass balance (assuming negligible BA concentration inside the disk). For each analysis, four assays of the standard solution and two of each sample were made, and the output peak height ratios were averaged.

The approximate time at which steady-state was achieved for each disk was taken as that time at which a profile of the top chamber BA concentration versus sample time became

linear. Five data points after this initial steady-state point were usually sufficient to successfully determine D_B using equation (2.10), depending on the amount of scatter in the points. Steady-state was normally achieved after five to ten days, while an entire profile could be obtained after one to two months (depending on the total porosity of the disk). No cells were allowed to reach equilibrium. The diaphragm cells were discarded after the experiment since the disks were no longer useful after exposure to the adhesive.

Whether the initial BA solution was placed in the top or bottom compartment was not seen to influence the value of D_B, since Stokes cells set up either way yielded diffusivity values that fit the predicted $\emptyset^E$ versus $\emptyset$ curve equally well. The only requirement is that the cell be mounted vertically to eliminate gravity-driven convective transport of solute at the disk surface. The Stokes cells can yield accurate values of D_B when they work, but they are prone to leakage and thus take a long time to produce useful results. Nonetheless, enough bulk diffusivity values were obtained from this type of experiment to allow development of a useful model for $\emptyset^E$.

b) Measurement of Aqueous Diffusivity

The diffusivity of benzoate ion in pH 6.9 phosphate buffer solution must be determined for use in equation (1.12). An equation for predicting the diffusivity of an ion at infinite dilution in water appears as follows[66]:

$$D_0 = 8.931 \times 10^{-10}\, T \left(\frac{l^0_+ \, l^0_-}{l^0_+ + l^0_-} \right) \left(\frac{z_+ + z_-}{z_+ \, z_-} \right) [=] \frac{cm^2}{s} \; ; \qquad (2.11)$$

where T is the absolute temperature (K), l^0_+ and l^0_- are the cationic and anionic conductances, respectively, at infinite dilution ($^{mhos}/_{eq}$) and z_+ and z_- are the absolute

values of the valences of the cation and anion, respectively. In this case, for the proton, $l^0_+ = 349.8\ ^{mhos}/_{eq}$, and for benzoate, $l^0_- = 32.4\ ^{mhos}/_{eq}$ (at T = 25°C). Inserting these values into equation (2.11) gives $D_0 = 1.58 \times 10^{-5}\ ^{cm^2}/_{s}$, which may be assumed to be equal to D_{aq}. (Infinite dilution is taken as a valid assumption in this system.) This value is higher than that of $D_{aq} = 1.00 \times 10^{-5}\ ^{cm^2}/_{s}$, which is the accepted value[67] for unionized benzoic acid at 25°C.

The Taylor dispersion method was used to experimentally estimate the diffusivity of benzoate ion in the solution used in the Stokes diffusion cell. An aqueous phosphate buffer solution of pH 6.91 ± 0.01 was pumped through the tubing of the Taylor dispersion apparatus to equilibrate a Beckman model 160 variable-wavelength absorbance detector set at 254 nm, and then a solution of this buffer containing 249.0 $^{\mu g}/_{ml}$ BA was injected into the system using a 20 µl sample loop. The water bath used to control the solution temperature was set at 25.0 ± 0.5°C. FBA and PB were not included in this solution, as they were assumed not to contribute to diffusion of BA in the diaphragm cells. The solute profile observed by the detector was recorded by a Kipp and Zonen linear chart recorder. The experimental set-up and other system parameters are discussed in Appendix C.

In the Taylor dispersion model , the solvent flow rate must be slow enough for a full laminar profile to develop in the tubing, so that the injected solute pulse can broaden into a parabolic shape before it reaches the detector. The amount of broadening then depends on the diffusion coefficient of the solute. The following equations,

$$c = \frac{M}{A_{cs}\sqrt{4\pi E_z t}} \exp\left[\frac{-(z - v_0 t)^2}{4 E_z t}\right]; \qquad (2.12a)$$

$$E_z = \frac{(R_0 v^0)^2}{48 D} [=] \frac{cm^2}{s}; \qquad (2.12b)$$

may be used to estimate D (in $^{g}/_{cm^3}$)[68], with the terms defined in Appendix C. The dispersion coefficient E_z is inversely proportional to D, so molecules with high diffusivities exhibit low degrees of dispersion. These equations are only applicable to dilute solutions, and are valid if the primary mass transport mechanisms that occur in the flow process are radial diffusion and axial convection.

Equation (2.12a) is an analogy to the one-dimensional decay of a pulse, which is the form taken by the desired output of the Taylor dispersion experiment. The maximum of the output curve of solute concentration versus time may be taken as the concentration c in equation (2.12a), with t the time at which this maximum occurs. Assuming the value of the exponent to be approximately equal to one, E_z may be obtained and D calculated from equation (2.12b). Letting D be equal to D_{aq}, the experimentally-determined value of D_{aq} for the benzoate anion may thus be given as:

$$D_{aq} = 1.45 \times 10^{-5} \pm 0.03 \times 10^{-5} \frac{cm^2}{s} ;$$

which is in fairly good agreement with the estimated value given above. Eleven values of D were used in calculating the standard error. This value of D_{aq} will be used for estimation of $\emptyset^E$ in this thesis.

c) Finite-Size Scaling

The finite-size scaling experiment differs from those presented above only in the composition of the powder used in ceramic disk manufacture. Specifically, polymer microspheres of known diameter were blended into batches of Aldrich alumina, containing 5% PVP, that had been made previously by the wet-mixing process. The microspheres,

obtained from Duke Scientific Co., possessed the properties given in Table 2.1. In this table, PVS/DVB refers to poly(styrene)/divinylbenzene microspheres ($\rho = 1.05\ ^{g}/_{cm^3}$), while PMMA refers to poly(methylmethacrylate) microspheres ($\rho = 1.19\ ^{g}/_{cm^3}$).

Based on finite-size scaling as described in Chapter I, including large spheres in the powder (and thus in unfired compacts) should produce artificially large pores in the finished disks, thus invalidating the assumption of an infinite lattice. The objective is to keep the total porosity about the same as that expected if no spheres were present, yet to mix enough spheres into the powder such that at least one sample-spanning cluster appears per finished disk. Eight total powder batches were thus made; four with enough spheres to account for 1% of the estimated final total porosity per disk, and four with enough spheres to account for 10% of the estimated final total porosity per disk. The resultant compositions of the powder batches are listed in Tables 2.2(a) and 2.2(b). These powders were processed as usual, except that all disks were sintered using the high temperature furnace in the Department of Water Chemistry, at a heating rate of $10\ ^{°C}/_{min}$ and a maximum sintering temperature of 1670°C. Ten disks were pressed from each batch, with five disks then being sintered for 12 hours and the other five disks being sintered for 24 hours. These firing times were used to eliminate as much residual porosity as possible, based on the results of previous experiments.

This section concludes the discussion of the procedures involved in processing, characterizing, and modeling the ceramic disks that were the focus of this work. The next chapter will describe the results obtained using these experiments.

Table 2.1. Properties of dry microspheres used in the study of finite-size scaling.

Sphere batch	1	2	3	4
Sphere composition	PVS/DVB	PVS/DVB	PVS/DVB	PMMA
Mean diameter/μm	136 ± 2.7	282 ± 5.6	468 ± 9.4	773 ± 15
Lot number	9276	10010	9513	8543
Spheres/g	7.2×10^5	8.1×10^4	1.8×10^4	4.0×10^3
Total weight/g	1	2	2	2
Volume per sphere/cm^3	1.32×10^{-6}	1.17×10^{-5}	5.37×10^{-5}	2.42×10^{-4}
Weight per sphere/g	1.39×10^{-6}	1.23×10^{-5}	5.56×10^{-5}	2.50×10^{-4}

Table 2.2(a). Powder compositions for finite-size scaling study, disks containing 1% spheres by volume.

Powder batch	1	2	3	4
Alumina used/g	59.99	60.01	60.03	60.01
Magnesia used/g	0.30	0.34	0.33	0.29
PVP used/g	3.19	3.38	3.17	3.18
Total spheres used/g	0.1585	0.1587	0.1579	0.1513

Table 2.2(b). Powder compositions for finite-size scaling study, disks containing 10% spheres by volume.

Powder batch	5	6	7	8
Alumina used/g	12.00	11.99	11.99	12.00
Magnesia used/g	0.06	0.06	0.07	0.06
PVP used/g	0.64	0.64	0.64	0.65
Total spheres used/g	0.3165	0.3158	0.3117	0.3108

III. DISK MANUFACTURING RESULTS AND DISCUSSION

As discussed previously, the first part of this work was concerned with characterizing those processing parameters that could be used to influence the porosities of fired alumina disks. The results of these processing studies will be presented and interpreted in this chapter. Bulk properties of powders as an outcome of mixing will be outlined first, and the different processing relationships studied will then be discussed.

A. Powder Mixing Observations

Powders mixed by both wet slurry mixing and dry ball milling were employed in several processing studies in this work, to determine qualitatively how the final porosity and densification behaviors of fired disks were affected by the method used to mix the binder with the ceramic powder. The two mixing methods investigated produced powders that exhibited very different bulk properties in regard to ease of handling and stability after compaction.

After mixing and vacuum drying, powders made by slurry mixing were very dry and showed no tendency to cake. Compacts pressed from these powders could not be easily broken. Thus, coating of the ceramic particles by the solubilized polymer binder during the slurry mixing process appeared to aid in adhesion of particles in the powder compact after compaction.

Conversely, ball-milled powders were very sticky after vacuum drying and tended to cake, making them difficult to measure or pour. Longer vacuum drying times did not affect this behavior. For a given compaction pressure, compacts made from ball-milled powders were easier to break than those made from slurry mixed powders. This indicated that the polymer binder was dispersed through the powder mass in discrete clumps, rather than as a

coating as in slurry mixing, so influence of the binder on compact mechanical strength was not as great. Also, plates of material on the upper face of a pressed compact had the tendency to shear away on separation from the upper die, which did not occur with slurry-mixed compacts. Caking appeared to be a result of electrostatic attraction between the ceramic particles rather than a consequence of the binder being present, since otherwise the slurry mixed powder should also have exhibited caking (which it did not). Because of the difficulty observed in handling ball milled powders, they were not used in some processing studies, or in the percolation theory work to be discussed in Chapter IV.

In all studies to be discussed next, the normalized weight loss ($[M_{initial} - M_{final}] / M_{initial}$) of a batch of disks pressed from a single powder mixture was observed in order to gauge whether or not the binder was completely dispersed throughout the ceramic powder by mixing. The standard error in the average weight loss for a batch of disks processed under a given set of conditions is an indication of nonuniformity due to incomplete mixing. This standard error was very low (typically about 1 to 5% of the total weight loss) in all studies, indicating that all powders could be considered completely mixed.

The compositions of powders used in this research, except for those powders used in the study of dependence of porosity on binder content, are summarized in Table 3.1. The mixtures used in the studies to be discussed next will be referred to in each study by the number in the first column of the table. All binder percentages are given as percent by weight (% ($^{W}/_{W}$)) of the total powder mass.

B. Processing Results

The processing studies outlined here were intended to determine how the variables compaction pressure, binder content, heating temperature, and heating time affected the final total porosity (Ø) of a fired alumina disk, so as to identify the one quantity that could

Table 3.1. Compositions of powder mixtures used in this research (except binder content study).

Powder mixtures are referred to by number in the following discussion.

Powder Mixture	Mixing Method	Alumina % ($^{w}/_{w}$)	Magnesia % ($^{w}/_{w}$)	PVP % ($^{w}/_{w}$)
1	Slurry mixing	89.51	0.48	10.01
2	Ball milling	89.50	0.48	10.02
3	Slurry mixing	89.55	0.45	10.00
4	Slurry mixing	94.48	0.50	5.02
5	Ball milling	94.48	0.52	5.00
6	Slurry mixing	94.51[a]	0.48	5.01

[a]Alcoa monodisperse alumina; all others Aldrich polydisperse alumina.

be most easily adjusted to manufacture disks with a range of total porosities for use in percolation theory analysis. Also, in some cases the fraction of volume lost by disks during firing ($\Delta V/V_0$) was estimated to demonstrate how the densification process was influenced by the above variables.

While reviewing the results given in this chapter, it must be kept in mind that ceramic powders typically exhibit different properties between manufacturers, or even between batches from the same manufacturer. Thus, although the trends observed in these processing studies are strictly valid only for the specific batch of alumina used, they can still help illustrate the expected processing characteristics of any alumina powder.

1. POWDER COMPACTION

This study was intended to determine the effect of compaction pressure on total disk porosity after firing at 1670°C for 4 hours, using both slurry mixed and ball-milled powders. Powder mixtures 1 and 2 in Table 3.1 were used in this study.

The fired disk porosity as a function of compaction pressure is summarized in Figure 3.1 for batches of disks made from both powder mixing techniques. In both cases the porosity decreased rapidly with increasing compaction pressure and then leveled off. From the trends exhibited in the figure it appears that increasing the compaction pressure decreased the void volume in the compact while increasing the total surface area of contact between particles, resulting in decreased porosity after firing. It should be noted that disks made from the ball-milled powder reach lower total porosities at lower compaction pressures than disks made from the slurry mixed powder, which is possibly a result of particle size reduction during the ball milling process.

Every powder possesses a maximum packing density that depends on its average particle size and polydispersity, and once this density is attained through compaction any

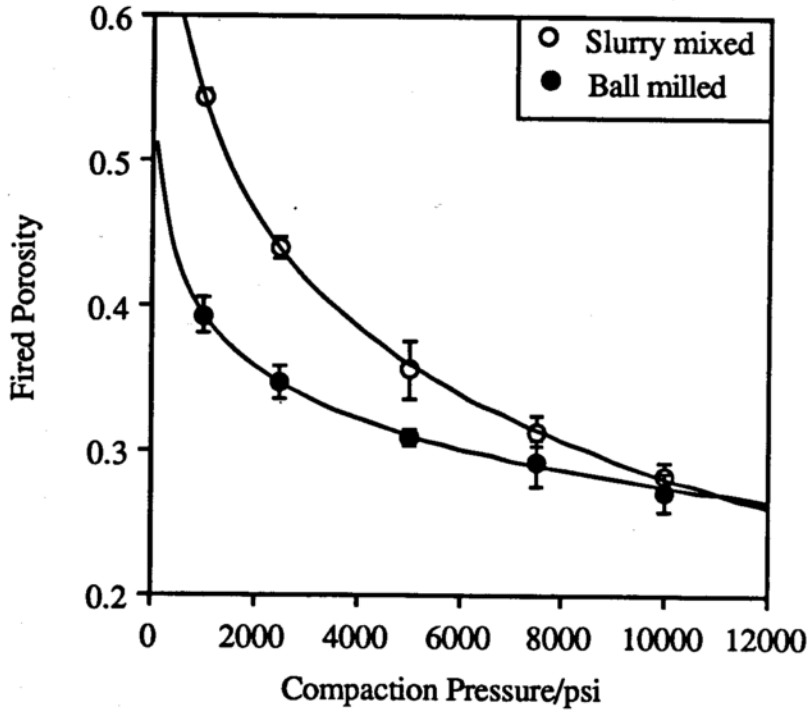

Figure 3.1. Influence of applied compaction pressure on average total porosity.
10% PVP, firing time 4 hours, firing temperature 1670°C.
(Data from Tables 3.2(a) and (b).)

Table 3.2(a). Compaction pressure study, 10% PVP slurry mixed powder. Values in parentheses represent standard error of four samples.

Pressure/psia[a]	Weight Loss	Sintered Porosity
1,000	0.0592 (0.0035)	0.544 (0.005)
2,500	0.0591 (0.0065)	0.440 (0.008)
5,000	0.0573 (0.0035)	0.356 (0.019)
7,500	0.0621 (0.0029)	0.314 (0.011)
10,000	0.0601 (0.0014)	0.283 (0.010)

[a]Firing time 4 hours, firing temperature 1670°C.

Table 3.2(b). Compaction pressure study, 10% PVP ball milled powder. Values in parentheses represent standard error of four samples.

Pressure/psia[a]	Weight Loss	Sintered Porosity
1,000	0.0645 (0.0027)	0.393 (0.013)
2,500	0.0635 (0.0027)	0.348 (0.011)
5,000	0.0650 (0.0024)	0.309 (0.006)
7,500	0.0657 (0.0032)	0.292 (0.016)
10,000	0.0667 (0.0033)	0.272 (0.013)

[a]Firing time 4 hours, firing temperature 1670°C.

further increase in pressure will not cause an additional decrease in the total void volume in the compact. Thus, only limited control over the final porosity is possible by varying the compaction pressure, since according to Figure 3.1, the total porosity would not be expected to decrease much further above a pressure of 10,000 psi. Also, since the total contact area between particles in a compact made at low pressure will be relatively low, mechanical stability of the solid microstructure of the disk cannot be assured at lower pressures.

All other processing studies in this work used a compaction pressure of 10,000 psi to manufacture compacts, to limit the amount of residual void space resulting from low-pressure compaction.

2. Influence of Binder Content

PVP binder contents of 5, 10, 15, and 20% ($^{w}/_{w}$) total powder were investigated in this study to determine whether increasing the binder content increased void volume in the compact after binder burn-out, which would result in increased total porosity of the fired disk. The compositions of the powder batches used in this study are summarized in Table 3.3. It was not possible to make compacts with 0% binder, since they could not be removed from the tablet punch without breaking.

The plot of total fired porosity versus binder content shown in Figure 3.2 illustrates that increasing the binder content increased the total fired porosity. The porosities of disks made from the two powders were approximately equal at low (5 and 10%) binder contents. However, the porosities of ball-milled powder disks increased more rapidly than the porosities of slurry-mixed powder disks at higher binder contents, reflecting the contribution of the binder to the volumes of individual voids remaining after burn-out. In other words, solubilizing the binder during slurry mixing allows the individual polymer

Table 3.3. Compositions of powder mixtures used in binder content study.

Powder Mixture	Mixing Method	Alumina % ($^{w}/_{w}$)	Magnesia % ($^{w}/_{w}$)	PVP % ($^{w}/_{w}$)
1.1	Slurry mixing	94.52	0.48	5.00
1.2	Ball milling	94.50	0.47	5.03
2.1	Slurry mixing	89.55	0.45	10.00
2.2	Ball milling	89.56	0.45	9.98
3.1	Slurry mixing	84.57	0.42	15.00
3.2	Ball milling	84.54	0.43	15.03
4.1	Slurry mixing	79.60	0.40	20.00
4.2	Ball milling	79.60	0.40	20.00

Table 3.4(a). Percent PVP study, slurry mixed powder. Values in parentheses represent standard error of six samples.

% ($^{W}/_{W}$) PVP[a]	Weight Loss	Sintered Porosity
5.00	0.0533 (0.0022)	0.168 (0.007)
10.00	0.0979 (0.0016)	0.219 (0.011)
15.00	0.1482 (0.0021)	0.284 (0.019)
20.00	0.1867 (0.0014)	0.315 (0.007)

[a]Compaction pressure 10,000 psi, firing time 4 hours, firing temperature 1670°C.

Table 3.4(b). Percent PVP study, ball milled powder. Values in parentheses represent standard error of six samples.

% ($^{W}/_{W}$) PVP[a]	Weight Loss	Sintered Porosity
5.03	0.0539 (0.0016)	0.148 (0.014)
9.98	0.0965 (0.0007)	0.189 (0.010)
15.03	0.1455 (0.0013)	0.333 (0.006)
20.00	0.1997 (0.0007)	0.451 (0.011)

[a]Compaction pressure 10,000 psi, firing time 4 hours, firing temperature 1670°C.

chains to disperse through the mixture, while the ball-milling process cannot break up the binder to as fine an extent during mixing. As a result, larger individual voids (that are difficult to remove by grain growth) may be left in ball-milled compacts after binder burn-out than in slurry mixed compacts. Thus, although the small error bars shown in Figure 3.2 for each datum point imply that the binder was uniformly dispersed in both powders during mixing (otherwise, the porosities of disks within a set would have varied more widely), the slurry mixing procedure appears to result in smaller, more numerous individual "clumps" of binder within the compact. On the other hand, the ball milling procedure does not reduce the binder to as fine a size as does slurry mixing, so larger clumps of binder separated by areas of no binder probably exist in the ball milled powder. Also, the observed difference in porosity between the ball-milled and slurry-mixed samples was not due to a difference in powder binder content, since normalized weight loss data given in Tables 3.4(a) and (b) illustrate that the same amount of binder was present in both powders.

The two lowest binder contents studied (5 and 10%) were used in the remainder of the processing work to be discussed in this chapter to minimize the contribution of binder volume to total porosity. In general, however, the amount of binder added to the ceramic powder does not appear to be a useful means of controlling the total porosity of the final device, since the distribution of binder through the powder during mixing is difficult to control and depends too strongly on the mixing method.

3. Weight Loss During Burn-Out

A qualitative estimate of the weight loss during burn-out of compacts containing 10% PVP was performed to determine the temperature range over which control of the rate of burn-out was most critical. Powder batches 1 and 2 in Table 3.1 were used in this study.

Figure 3.3 shows the normalized weight loss profiles for sets of compacts made from slurry mixed and ball milled powders In each case, one set of compacts was used to obtain every point in the profile, by heating to the desired temperature, cooling, and determining the weight. Both sets of compacts exhibited equivalent weight loss profiles.

Initial heating from room temperature (25°C) to 220°C resulted in a small amount of weight loss due to removing bound water from the microstructure. Heating from 220°C to 520°C resulted in the most weight loss, due to volatilization of the organic binder. Above this range, the small amount of additional weight loss was probably due to removal of bound surface water from the alumina grains. Thus, control of the rate of temperature increase over the temperature range 220°C - 520°C is needed to keep the rate of binder combustion low, so as to prevent disruption of the solid microstructure during escape of volatilized binder. Because the compacts made in this study were fairly small, a heating time of 30 minutes at each step was thought to be sufficient for complete thermal equilibrium to be attained throughout the compact bulk.

The average total weight lost by a set of disks after burn-out was found to coincide closely with the weight percent binder added to the ceramic powder before mixing. Specifically, as may be seen from Table 3.5, the weight loss over the range 220°C - 520°C corresponds to within 1% of the weight percent PVP added to the powder before mixing. Also, the standard error bars shown in Figure 3.3 are fairly small, indicating that the binder was uniformly mixed into the ceramic powder by both mixing procedures.

After burn-out, the compacts were very fragile and required great care in handling. No change in the overall compact volume was observed as a result of burn-out.

4. Temperature Dependence of Porosity

As discussed in Chapter I, thermal energy must be supplied to the ceramic compact to

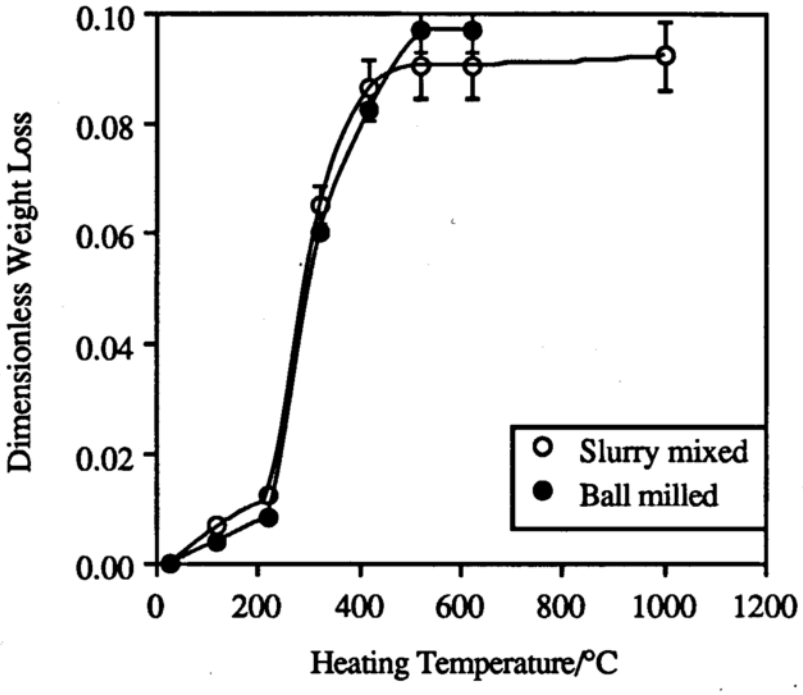

Figure 3.3. Relative weight loss during burn-out, slurry mixed disks.
Pressure 10,000 psi, heating time 30 minutes each step.
(Data from Table 3.5.)

Table 3.5. Weight loss during heating at low temperature (10% PVP). Values in parentheses represent standard error of four samples.

Temperature[a]/°C	Weight Loss[b]	Weight Loss[c]
25	0.0000 (0.0000)	0.0000 (0.0000)
100	0.0068 (0.0004)	0.0041 (0.0005)
220	0.0123 (0.0008)	0.0086 (0.0005)
320	0.0654 (0.0035)	0.0603 (0.0009)
420	0.0868 (0.0047)	0.0828 (0.0024)
520	0.0907 (0.0062)	0.0968 (0.0037)
620	0.0907 (0.0062)	0.0968 (0.0037)
1000	0.0923 (0.0062)	

[a]Compaction pressure 10,000 psi, heating time 30 minutes.
[b]Slurry mixed powder; [c]ball milled powder.

drive the dual processes of grain coalescence (sintering) and densification. Thus, temperature should be the variable that exerts the most influence on the shrinkage and final porosity of a fired disk, since it controls atomic mobility within and between grains. In this study, compacts were heated over the temperature range 1000°C to 1670°C to establish the approximate temperature at which densification appeared to begin, and also to see how rapidly the porosity decreased above this temperature. Powder batches 1 and 2 listed in Table 3.1 were used in this study.

The fraction of original volume lost versus heating temperature is shown in Figure 3.4, while total disk porosity as a function of temperature is given in Figure 3.5. Again, one set of disks was used to obtain every point in the profile shown for a given powder type, by heating to the desired temperature, cooling, and weighing. The profiles shown in both figures exhibit an "initiation temperature", at about 1400°C, below which the compacts did not appear to densify. Whether any grain coalescence occurred below this temperature could not be determined, but compacts heated at or below 1400°C showed no discernible increase in mechanical strength (as exhibited by resistance to breakage) compared to compacts that were not heated. Ball-milled and slurry mixed powders exhibited nearly identical decreases in porosity above the initiation temperature, and also showed equivalent densification behaviors.

Above the assumed initiation temperature, the rate of compact densification increased rapidly with increasing temperature. For example, 10% of the initial disk volume was lost between 1600°C and 1670°C, as may be seen from Figure 3.4. Heating to higher temperatures should cause an even more significant decrease in volume, although it was not possible, due to the maximum heating temperature of the available equipment (1700°C), to determine at what temperature a polydisperse compact would attain its maximum density.

Figure 3.4 shows that compacts made from either powder batch appeared to gain some

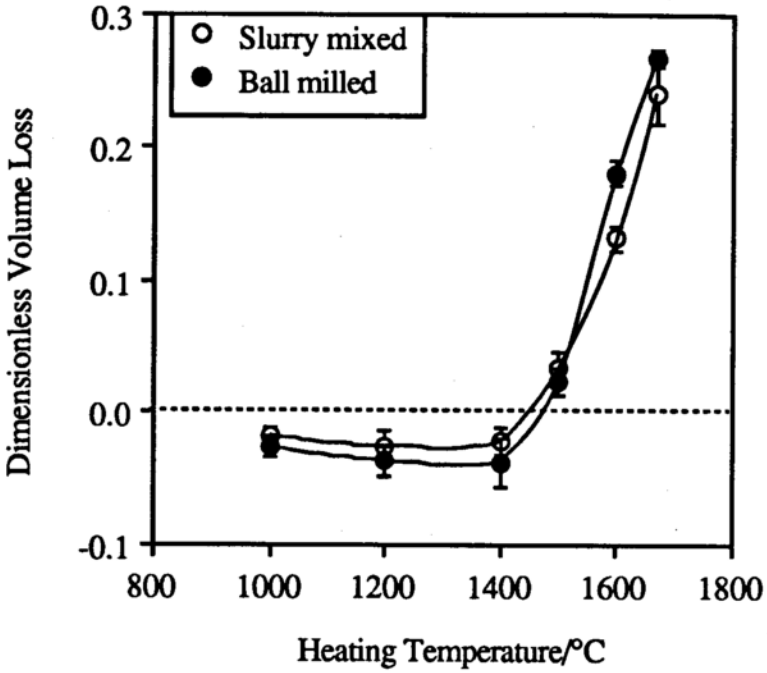

Figure 3.4. Relative volume shrinkage as a function of heating temperature. 10% PVP, pressure 10,000 psi, heating time 4 hours each step. (Data from Tables 3.6(a) and (b).)

Table 3.6(a). Firing temperature study, 10% PVP slurry mixed powder.
Values in parentheses represent standard error of four samples.

Temperature[a]/°C	Weight loss	Volume loss	Sintered Porosity
1000	0.0544 (0.0024)	- 0.017 (0.005)	0.482 (0.003)
1200	0.0554 (0.0029)	- 0.026 (0.013)	0.487 (0.006)
1400	0.0539 (0.0016)	- 0.022 (0.010)	0.487 (0.003)
1500	0.0561 (0.0032)	0.033 (0.014)	0.457 (0.010)
1600	0.0575 (0.0025)	0.132 (0.009)	0.396 (0.005)
1670	0.0588 (0.0054)	0.241 (0.023)	0.312 (0.019)

[a]Compaction pressure 10,000 psi, firing time 4 hours.

Table 3.6(b). Firing temperature study, 10% PVP ball milled powder.
Values in parentheses represent standard error of four samples.

Temperature[a]/°C	Weight loss	Volume loss	Sintered Porosity
1000	0.0603 (0.0013)	- 0.026 (0.009)	0.499 (0.004)
1200	0.0601 (0.0016)	- 0.037 (0.011)	0.504 (0.006)
1400	0.0580 (0.0024)	- 0.038 (0.019)	0.503 (0.008)
1500	0.0600 (0.0046)	0.023 (0.010)	0.475 (0.005)
1600	0.0634 (0.0024)	0.181 (0.009)	0.390 (0.006)
1670	0.0623 (0.0008)	0.267 (0.007)	0.298 (0.006)

[a]Compaction pressure 10,000 psi, firing time 4 hours.

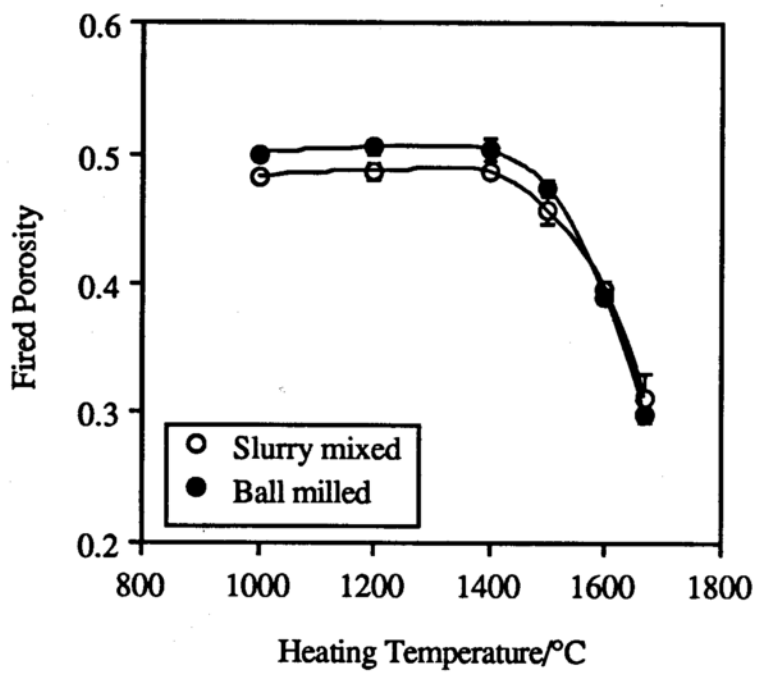

Figure 3.5. Average total porosity as a function of heating temperature. 10% PVP, pressure 10,000 psi, heating time 4 hours each step. (Data from Tables 3.6(a) and (b).)

volume below 1400°C. It is not known what process might be responsible for this behavior, but some rearrangement of the solid microstructure due to thermal expansion of the compact may be occurring that prevents the compact from shrinking back to its original size when cooled. This behavior would be less likely to occur with a more monodisperse powder compact, since rearrangement in such a compact would not result in significantly altering the stacking pattern in the microstructure.

The observed degree of densification with increasing temperature indicates that heating temperature is the most important variable for control of porosity during the firing process, at least for a given ceramic powder with a distinct set of characteristics. However, particle size of the powder (to be considered shortly) should be as important an influence on porosity and densification as is temperature, since smaller particles should exhibit a lower initiation temperature and an accelerated rate of densification.

5. Time Dependence of Shrinkage and Porosity

The manner in which the densification process depends on the length of time spent at a certain firing temperature reflects the mechanism of grain growth occurring at that time and temperature. The influence of firing time on the processes of densification and porosity elimination was investigated in this study for two reasons: First, the rapid densification that was seen to occur over a narrow range of available temperatures (1400 - 1670°C) in this system was thought to make reproducible variation of the fired porosity through temperature control impractical; and second, it was hoped that some insight into the mechanism of densification of the polydisperse powder could be obtained through such a study. Normalized volume loss and total porosity were determined at 1670°C over a range of firing times (1 to 36 hours) for disks made from powder batches 3, 4, and 5.

The volume loss observed for disks made from 10% PVP slurry mixed powder is

given as a function of firing time in Figure 3.6. Different sets of disks were used to obtain each datum point. The profile shown indicates that densification is a decreasing function of firing time, such that for a given firing temperature the rate of densification of the disk will become slower with increasing firing time until virtually no change in density is observed. However, the densification process should not entirely cease at any time.

Although not studied directly in this work, grain coalescence was assumed to occur over the entire range of heating times, since it depends only on contact between discrete grains and not on the presence of large voids that will control the ultimate shrinkage of the compact. However, the rate of densification should decrease as the concentration of large voids in the disk (before firing) increases. The rapid initial rate of densification is probably a result of eliminating small voids in the compact through grain growth, which slows once the majority of these voids have been filled.

Thus, two different processes appear to take place during firing in this system. The first, occurring primarily at short firing times, is that of rapid densification due to growth of grains into small voids, while the other, occurring over the entire time range, may be that of grain coalescence with little additional shrinkage of the disk. The rapid densification mechanism is assumed to control the bulk properties of the fired disk (except for strength, which was not investigated).

To show that two parallel processes exist, The logarithmic form of equation (1.3) can be used to show that two parallel densification processes exist, as follows: of both volume loss and firing time may be plotted to obtain a fit analogous to equation 3.1,

$$\ln\left(\frac{\Delta V}{V_0}\right) = \frac{2}{5}\ln(t) + \alpha \ ; \qquad (3.1)$$

where α is a lumped constant that includes the unknown particle radius, which was not

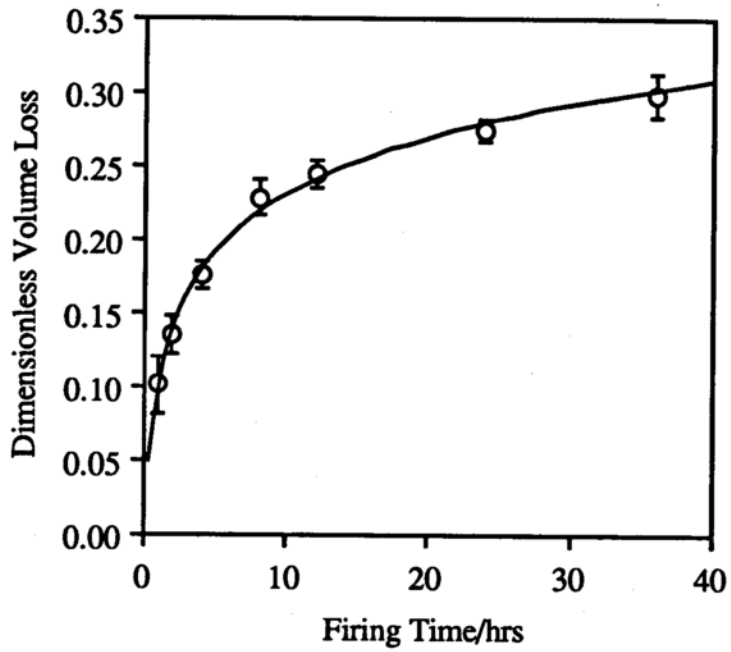

Figure 3.6. Relative volume shrinkage as a function of time, firing temperature 1670°C. 10% PVP, slurry mixed powder, pressure 10,000 psi.
(Data from Table 3.7.)

Table 3.7. Firing time study, 10% PVP slurry mixed powder.
Values in parentheses represent standard error of number of samples listed.

Time/hrs[a]	Disks	Weight loss	Volume loss	Sintered Porosity
1	14	0.0973 (0.0037)	0.101 (0.019)	0.349 (0.014)
2	14	0.1015 (0.0029)	0.135 (0.013)	0.325 (0.010)
4	15	0.0975 (0.0041)	0.176 (0.009)	0.291 (0.008)
8	15	0.0981 (0.0023)	0.228 (0.012)	0.243 (0.012)
12	14	0.0988 (0.0029)	0.245 (0.009)	0.227 (0.009)
24	14	0.1001 (0.0040)	0.274 (0.007)	0.195 (0.008)
36	15	0.1041 (0.0072)	0.298 (0.015)	0.167 (0.018)

[a]Compaction pressure 10,000 psi, sintering temperature 1670°C.

expected to change substantially in this study due to the polydispersity of the powder. A plot of $\ln(\Delta V/V_0)$ versus ln(t) can be made to determine if the experimental data follow the predicted time exponent of $2/5$.

A plot of $\ln(\Delta V/V_0)$ versus ln(t) is shown in Figure 3.7. The initial (steeper) portion of the plot is fit by the following equation:

$$\ln\left(\frac{\Delta V}{V_0}\right) = 0.391 \ln(t) - 2.284 \ ; \tag{3.2}$$

while the latter part of the plot is fit as follows:

$$\ln\left(\frac{\Delta V}{V_0}\right) = 0.175 \ln(t) - 1.843 \ . \tag{3.3}$$

The time exponents obtained from these fits, 0.391 and 0.175, show that one mechanism controls the volume loss at short firing times, but fades at longer times. The slope of the initial curve, 0.391, closely approximates the predicted exponent of $2/5$, implying that the mechanism modeled by equation (1.3) also occurs in this system; namely, lattice diffusion of material from the grain boundaries to the necks between the particles[19].

Densification at longer times follows a slope of 0.175, which approximates a time exponent of $1/5$. The transport mechanism governing this densification behavior was not determined. Thus, those small voids that can be filled through densification have mostly disappeared after eight hours firing at 1670°C, so heating of a polydisperse compact at longer times should primarily result in additional grain coalescence and little additional densification, as was observed in this system.

The influence of time on total fired porosity for the same sets of disks is presented in Figure 3.8. This profile shows a rapid decrease in total porosity due to densification at

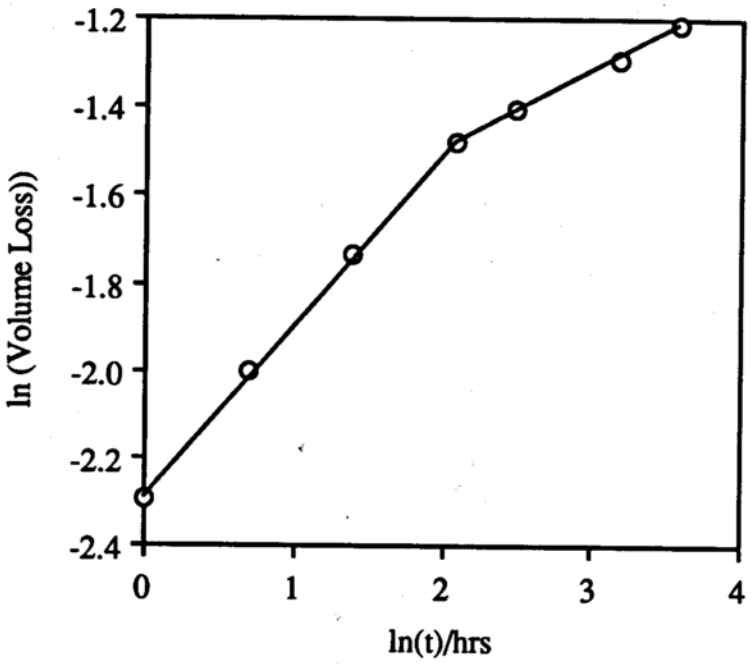

Figure 3.7. $\ln(\Delta V/V_0)$ as a function of ln(t).
(Logarithmic form of Figure (3.6).)
(Data from Table 3.7.)

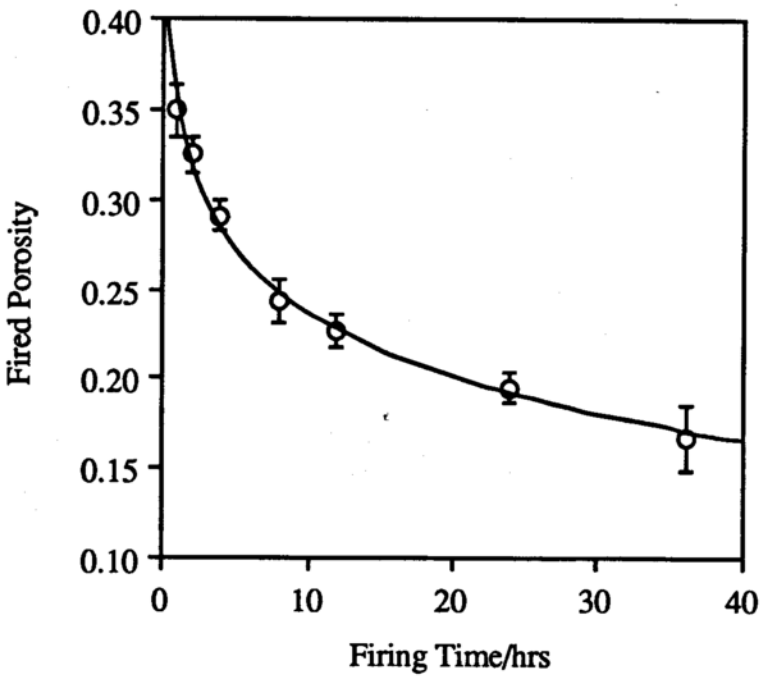

Figure 3.8. Dependence of average total porosity on time, firing temperature 1670°C. 10% PVP, slurry mixed powder, pressure 10,000 psi.
(Data from Table 3.7.)

short times, but little additional shrinkage at longer times. Thus, in general, time is not a very useful means of controlling the final porosity[19], especially if the overall goal of the process is porosity removal (as is the usual case).

Although some influence over total porosity is possible over short times, firing for a short period does not guarantee that sintering has occurred uniformly (on a microscopic scale) through the entire disk. This is especially true for a disk made from a polydisperse powder, since it would tend to sinter more slowly than a monodisperse powder disk as a result of its wide distribution of grain sizes[23]. In other words, after only one hour the center of a polydisperse disk may have sintered to a lesser extent than its exterior. This may occur because the individual ceramic grains have been observed in this work to align parallel to the disk surface as a result of compaction, such that the surface structure possesses more surface area of contact between grains than the interior (as will be discussed in the next chapter). Thus, the interior solid microstructure will be only loosely held together. This weak interior structure may be more easily disrupted by mechanical stress than the more strongly-bonded surface, and if such disruption occurs a non-random porosity distribution can result between the interior and the surface that makes percolation theory results more difficult to interpret. It does appear to occur in disks fired at short times, as will be discussed in the context of aqueous pycnometry in the next chapter.

The volume loss and total fired porosity for disks made from both slurry mixed and ball-milled powders containing 5% binder are shown as functions of firing time in Figures 3.9 and 3.10, respectively. Both mixing processes result in the same densification behavior as shown previously in Figure 3.6. The ball-milled compacts appeared to shrink more rapidly than the slurry mixed compacts, due to size reduction of the powder during milling. As expected from the results shown in Figure 3.2, disks made from 10% PVP powder exhibited less densification over a given firing time than disks made from 5% PVP

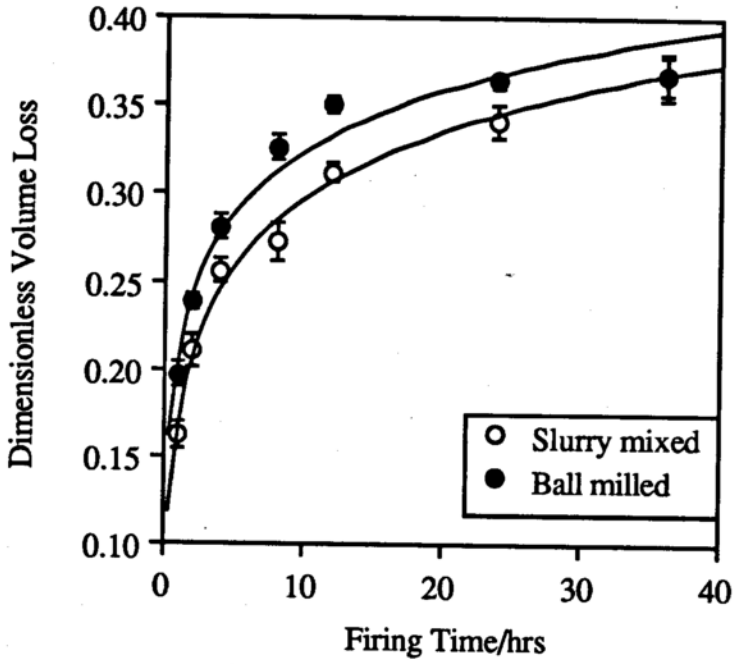

Figure 3.9. Dependence of relative volume shrinkage on time fired at 1670°C.
5% PVP, pressure 10,000 psi.
(Data from Tables 3.8(a) and (b).)

Table 3.8(a). Firing time study, 5% PVP slurry mixed powder.
Values in parentheses represent standard error of six samples.

Time/hrs[a]	Weight loss	Volume loss	Sintered Porosity
1	0.0584 (0.0034)	0.162 (0.008)	0.349 (0.008)
2	0.0536 (0.0044)	0.210 (0.009)	0.306 (0.011)
4	0.0518 (0.0038)	0.256 (0.007)	0.262 (0.006)
8	0.0526 (0.0027)	0.272 (0.011)	0.247 (0.012)
12	0.0507 (0.0024)	0.312 (0.006)	0.201 (0.006)
24	0.0499 (0.0023)	0.341 (0.010)	0.167 (0.013)
36	0.0452 (0.0036)	0.367 (0.011)	0.129 (0.016)

[a]Compaction pressure 10,000 psi, firing temperature 1670°C.

Table 3.8(b). Firing time study, 5% PVP ball milled powder.
Values in parentheses represent standard error of six samples.

Time/hrs[a]	Weight loss	Volume loss	Sintered Porosity
1	0.0531 (0.0006)	0.197 (0.007)	0.318 (0.007)
2	0.0523 (0.0047)	0.238 (0.005	0.281 (0.007)
4	0.0503 (0.0015)	0.281 (0.007)	0.237 (0.008)
8	0.0527 (0.0020)	0.326 (0.007)	0.189 (0.009)
12	0.0526 (0.0015)	0.350 (0.005)	0.159 (0.007)
24	0.0540 (0.0021)	0.364 (0.004)	0.141 (0.006)
36	0.0451 (0.0035)	0.367 (0.013)	0.130 (0.016)

[a]Compaction pressure 10,000 psi, firing temperature 1670°C.

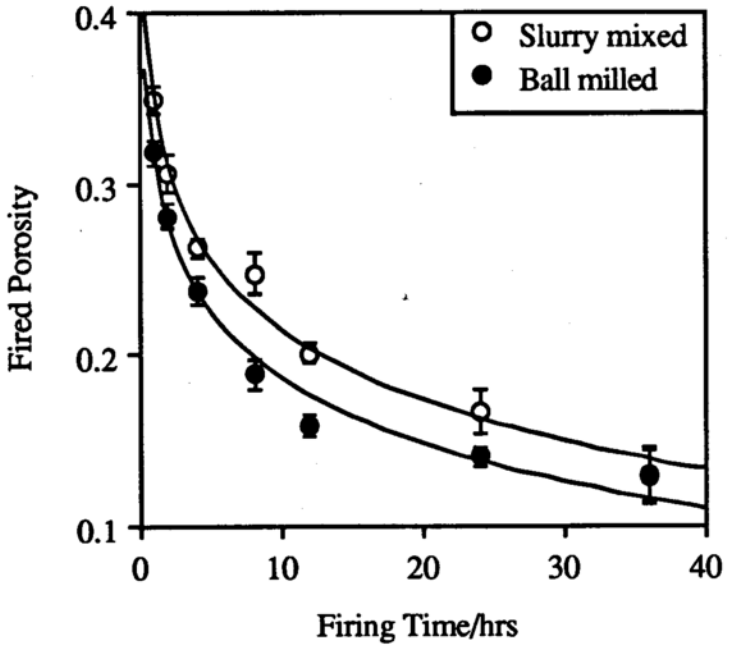

Figure 3.10. Dependence of average total porosity on time fired at 1670°C.
5% PVP, pressure 10,000 psi.
(Data from Tables 3.8(a) and (b).)

powder, reflecting the increased contact area and smaller average void size between grains in the 5% compacts. The total fired porosities of 10% disks were somewhat higher than those of 5% disks, indicating that 5% PVP compacts contained voids of smaller average size that could be filled more easily by the surrounding grains during firing.

In summary, for a ceramic compact with a set particle size or range of polydispersity, the final porosity and extent of densification will be influenced most strongly by the firing temperature. Only limited control of either property is possible through varying compaction pressure or firing time, especially since low compaction pressures or short firing times may detract from the strength of the final product. However, variation of the porosities of disks made for percolation theory investigations was accomplished in this work using firing time as the controlling variable, since (as noted previously) time could be manipulated more conveniently than temperature given the equipment at hand, and also because the desired range of porosities could be obtained through varying the firing time alone.

The amount of binder added to the ceramic powder appeared to influence the volumes of individual voids within the compact, with the void volume increasing with increasing binder content. However, this method of modifying the porosity will also depend on the technique used to mix the powders, thus making it difficult to control. Variation of the ceramic particle size is the best way to control total porosity and shrinkage within a given set of compaction and firing conditions, as will be shown next.

6. Effect of Polydispersity on Porosity and Densification

The final set of processing studies undertaken in this work compared the results already obtained for polydisperse Aldrich alumina powders to those exhibited by an Alcoa

0.5 μm nominal diameter monodisperse alumina powder (batch #6). Aldrich polydisperse powder 4 listed in Table 3.1 was used in this study. Both powders were mixed by slurry mixing, and both mixtures were used to press disks at 10,000 psi. Each datum point in the graphs shown in this section was obtained using a different set of disks. A programmable furnace was used to allow for fine control of these processing variables: Firing temperature, firing time, and heating rate. Comparisons were also made in these studies between the dimensional measurement and Archimedes volume displacement methods of bulk disk volume determination discussed in Chapter II. The small monodisperse powder and highly polydisperse powder used in this investigation may be regarded as lower and upper bounds, respectively, in study of the influence of particle size on densification.

a) Firing Temperature

Volume loss as a function of firing temperature for monodisperse and polydisperse compacts is shown in Figure 3.11. In the temperature range (1450 - 1670°C) over which densification was observed in a polydisperse compact, the monodisperse compact had already nearly reached its maximum density and was only weakly influenced by temperature. Monodisperse compacts probably possess a lower initiation temperature for densification (about 1100°C) than polydisperse compacts, and densify much more rapidly once this temperature is achieved. The temperature at which densification begins in a monodisperse compact would thus be likely to increase with increasing particle size, while the rate of densification would decrease with increasing particle size.

Monodisperse compacts lost about 40% of their initial volumes as a result of densification. Thus, these compacts possessed large total void volumes before firing, but the individual voids were of small enough size that the small surrounding grains were able to grow to occupy their volumes and produce substantial amounts of shrinkage. The small

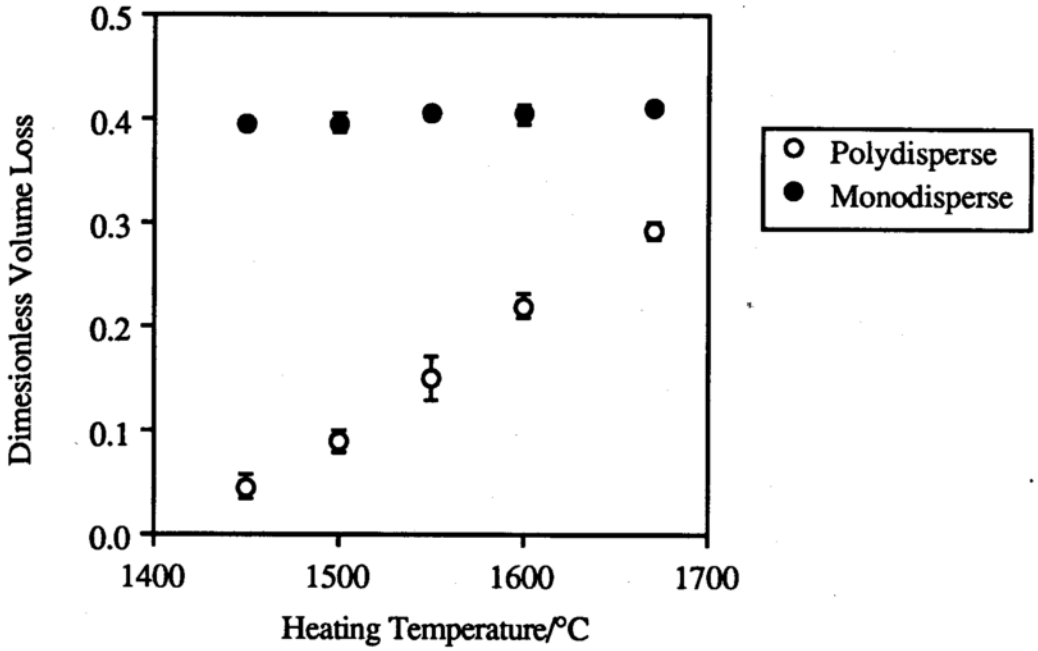

Figure 3.11. Relative volume loss due to heating temperature and powder polydispersity. 5% PVP, slurry mixed powders, pressure 10,000 psi, firing time 4 hours. (Data from Tables 3.9(a) and (b).)

Table 3.9(a). Firing temperature study, Thermolyne furnace, 5% PVP polydisperse alumina powder

Values in parentheses represent standard error of five samples.

Temp.[a]/ ℃	Weight loss	Volume loss (Dimensional)[b]	Sintered Porosity (Dimensional)[b]	Sintered Porosity (Archimedes)[c]
1450	0.0507 (0.0012)	0.046 (0.013)	0.445 (0.008)	0.429 (0.002)
1500	0.0502 (0.0007)	0.090 (0.011)	0.413 (0.007)	0.394 (0.002)
1550	0.0498 (0.0009)	0.149 (0.021)	0.371 (0.016)	0.354 (0.001)
1600	0.0510 (0.0018)	0.219 (0.012)	0.315 (0.011)	0.293 (0.003)
1670	0.0498 (0.0011)	0.291 (0.008)	0.244 (0.009)	0.215 (0.002)

[a]Compaction pressure 10,000 psi, firing time 4 hours.

[b]Bulk method of volume estimation.

[c]Archimedes principle volume estimation.

Table 3.9(b). Firing temperature study, Thermolyne Furnace, 5% PVP monodisperse alumina powder.

Values in parentheses represent standard error of five samples.

Temp.[a]/ ℃	Weight loss	Volume loss (Dimensional)[b]	Sintered Porosity (Dimensional)[b]	Sintered Porosity (Archimedes)[c]
1450	0.0596 (0.0010)	0.395 (0.006)	0.114 (0.010)	0.080 (0.001)
1500	0.0596 (0.0018)	0.395 (0.009)	0.114 (0.014)	0.078 (0.001)
1550	0.0602 (0.0008)	0.404 (0.004)	0.103 (0.005)	0.053 (0.001)
1600	0.0604 (0.0008)	0.405 (0.009)	0.099 (0.015)	0.051 (0.001)
1670	0.0592 (0.0011)	0.411 (0.005)	0.099 (0.008)	0.045 (0.003)

[a]Compaction pressure 10,000 psi, firing time 4 hours, heating rate $10°C/_{min}$.

[b]Bulk method of volume estimation.

[c]Archimedes principle volume estimation.

surface area of contact and large individual voids between particles in the polydisperse compacts prevented them from densifying to a comparable extent at any given firing temperature, which is why polydisperse materials would be more useful for manufacture of porous ceramic delivery devices.

The large amount of shrinkage that took place in monodisperse compacts resulted in more severe dimensional nonuniformity than was observed previously with polydisperse compacts, such that the dimensions of these disks were very difficult to measure using the micrometer and calipers employed for determining volume in previous studies. The monodisperse disks tended to shrink along the density gradients shown in Figure 1.3, with the regions of lowest compaction density exhibiting the greatest shrinkage. Overall, the disks assumed a bowl-like shape, with one face bowing outward and the other sinking toward the center.

To determine the inaccuracy of dimensional measurement, the Archimedes volume exclusion method described in Chapter II was used to measure bulk volumes of the fired disks. Figures 3.12 and 3.13 show comparisons between total porosities calculated from volumes obtained by the dimensional and Archimedes volume determination methods for polydisperse and monodisperse disks, respectively. The error bars shown in Figure 3.13 illustrate the substantial error associated with porosity determination by dimensional measurement of the monodisperse disks. The error in volume measurement was lower in all cases using the Archimedes method than the dimensional method. Also, the small error bars associated with the Archimedes porosities indicated that any systematic errors due to the process of blotting the disks dry before final weighing were negligible.

Porosities obtained by the Archimedes method for both monodisperse and polydisperse disks were lower, typically by about 4%, than those obtained dimensionally. It was unclear whether this discrepancy was due to the blotting process, or whether the

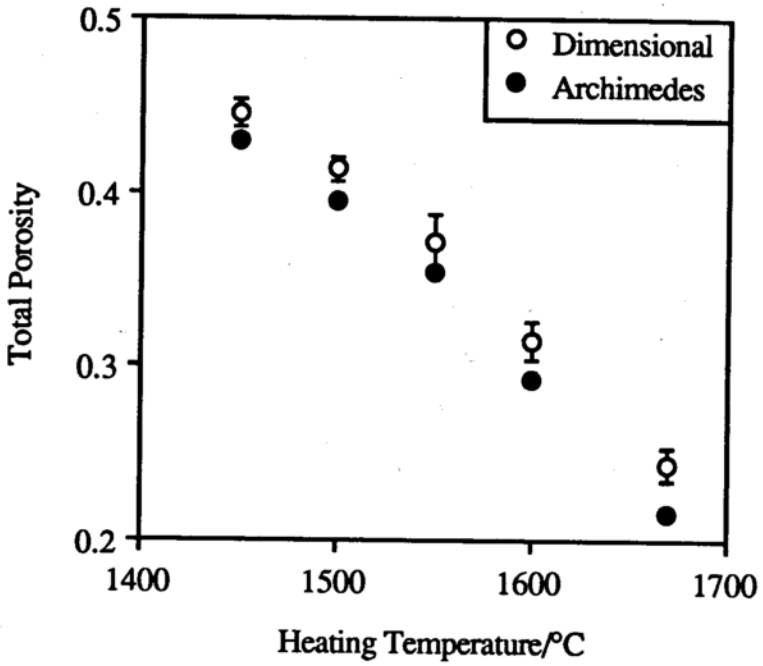

Figure 3.12. Difference in total porosities obtained by dimensional or Archimedes volume measurement, polydisperse compacts.
(Data from Table 3.9(a).)

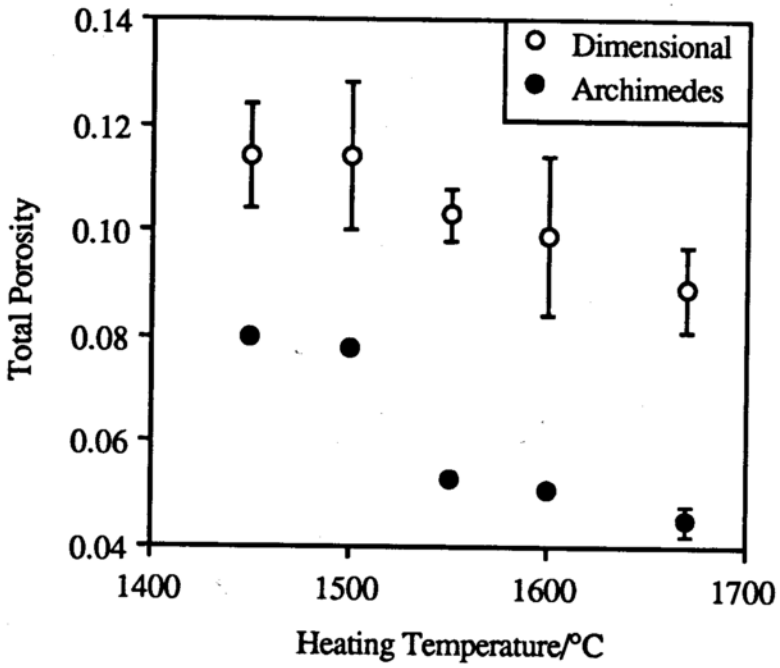

Figure 3.13. Difference in total porosities obtained by dimensional or Archimedes volume measurement, monodisperse compacts.
(Data from Table 3.9(b).)

method of dimensional measurement tended to yield total disk volumes that were too high. The latter possibility appeared to be more likely, since use of the Archimedes method should eliminate much of the contribution of surface roughness of a disk to its observed total volume.

The observed densification during firing was not corrected using the Archimedes volumes obtained in these studies, since all initial compact volumes were obtained by dimensional measurement only and it was felt that results of the two different methods should not be mixed. Also, the normalization calculation appeared to minimize any random error due to disk nonuniformity or surface roughness. However, all final disk porosities were obtained using both methods, and compared. The porosities described in the remainder of this chapter will be those obtained using the Archimedes method only.

The Archimedes porosities for monodisperse and polydisperse powder compacts as functions of firing temperature are shown in Figure 3.14. The monodisperse compacts exhibited little decrease in porosity over the temperature range studied, whereas the polydisperse compacts lost 25% of their initial porosity. The slope of the porosity profile for the polydisperse powder became increasingly negative as the temperature increased, illustrating that the rate of void elimination increased as expected from the profile given in Figure 3.5.

b) Firing Time

From the results of the previous study, the firing time was not expected to influence the shrinkage or porosity of a monodisperse compact at the temperature under investigation (1600°C). Figure 3.15 shows that, even after one hour at the firing temperature, the monodisperse compact had reached its maximum volume loss, while polydisperse compacts showed the same behavior as exhibited in Figure 3.9. No change in porosity

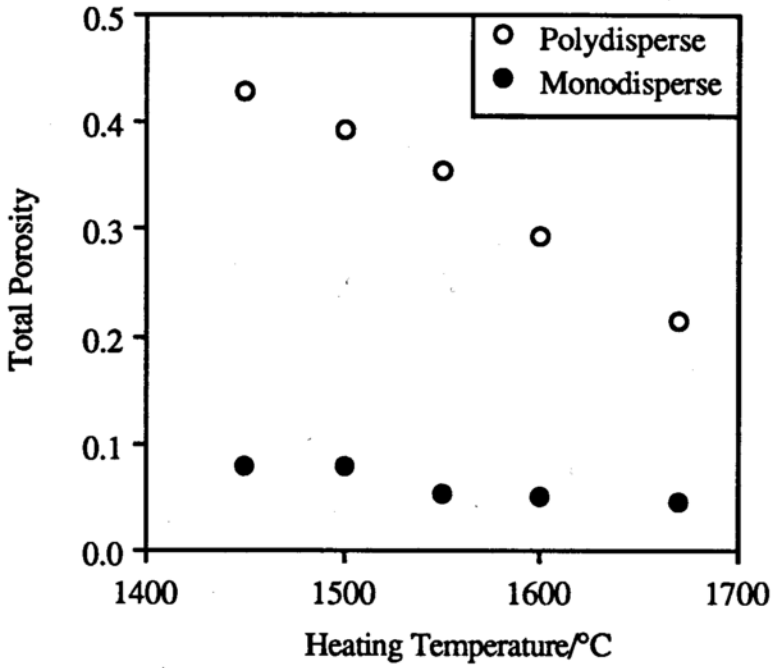

Figure 3.14. Dependence of total porosity on heating temperature and powder polydispersity.
Porosities obtained by Archimedes method, 5% PVP, slurry mixed powders, pressure 10,000 psi, firing time 4 hours.
(Data from Tables 3.9(a) and (b).)

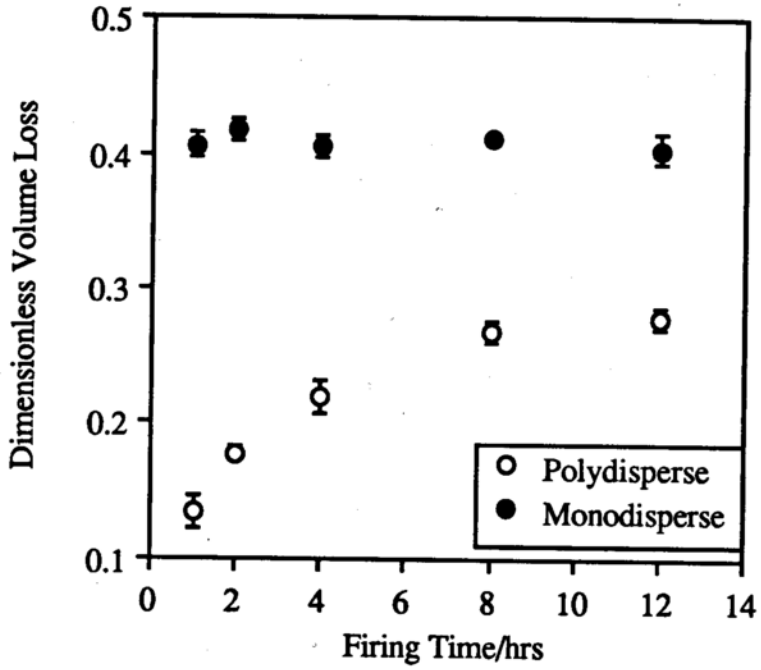

Figure 3.15. Relative volume loss due to firing time and powder polydispersity. 5% PVP, slurry mixed powders, pressure 10,000 psi, firing temperature 1600°C. (Data from Tables 3.10(a) and (b).)

Table 3.10(a). Sintering time study, Thermolyne furnace, 5% PVP polydisperse alumina powder.

Values in parentheses represent standard error of five samples.

Time/ hrs[a]	Weight loss	Volume loss (Dimensional)[b]	Sintered Porosity (Dimensional)[b]	Sintered Porosity (Archimedes)[c]
1	0.0486 (0.0015)	0.134 (0.012)	0.383 (0.008)	0.364 (0.001)
2	0.0488 (0.0010)	0.177 (0.005)	0.351 (0.005)	0.333 (0.002)
4	0.0510 (0.0018)	0.219 (0.012)	0.315 (0.011)	0.293 (0.003)
8	0.0479 (0.0014)	0.267 (0.008)	0.268 (0.009)	0.251 (0.001)
12	0.0485 (0.0020)	0.278 (0.008)	0.257 (0.009)	0.228 (0.003)

[a]Compaction pressure 10,000 psi, firing temperature 1600°C, heating rate $10°C/_{min}$.

[b]Bulk method of volume estimation.

[c]Archimedes principle volume estimation.

Table 3.10(b). Sintering time study, Thermolyne furnace, 5% PVP monodisperse alumina powder.

Values in parentheses represent standard error of five samples.

Time/ hrs[a]	Weight loss	Volume loss (Dimensional)[b]	Sintered Porosity (Dimensional)[b]	Sintered Porosity (Archimedes)[c]
1	0.0598 (0.0002)	0.406 (0.010)	0.099 (0.015)	0.056 (0.002)
2	0.0605 (0.0014)	0.417 (0.008)	0.083 (0.014)	0.046 (0.001)
4	0.0604 (0.0008)	0.405 (0.009)	0.099 (0.015)	0.051 (0.001)
8	0.0596 (0.0016)	0.412 (0.002)	0.088 (0.005)	0.049 (0.002)
12	0.0589 (0.0009)	0.404 (0.011)	0.099 (0.017)	0.048 (0.001)

[a]Compaction pressure 10,000 psi, firing temperature 1600°C, heating rate $10°C/_{min}$.

[b]Bulk method of volume estimation.

[c]Archimedes principle volume estimation.

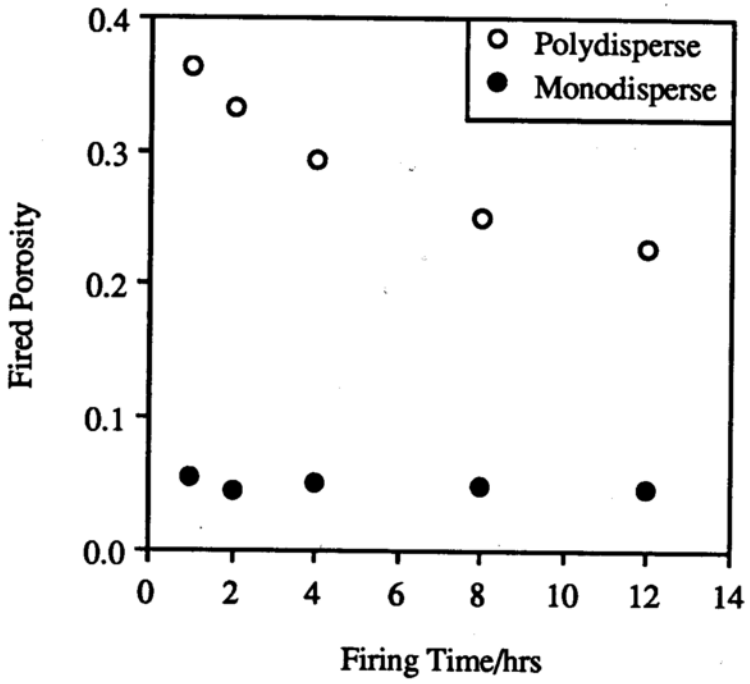

Figure 3.16. Dependence of total porosity on firing time and powder polydispersity. Porosities obtained by Archimedes method, 5% PVP, slurry mixed powders, pressure 10,000 psi, firing temperature 1600°C.
(Data from Tables 3.10(a) and (b).)

with respect to firing time was observed with the monodisperse compacts either, as may be seen in Figure 3.16.

c) Heating Rate

This final study was undertaken to see if the rate at which the firing temperature was reached had any influence on the final disk porosity. Based on the results of the previous two studies, no effect was anticipated in the case of the monodisperse powder for the particular processing parameters used (1600°C firing for 4 hours).

Volume loss and fired porosity are shown in Figures 3.17 and 3.18, respectively, for both monodisperse and polydisperse compacts. As expected, the monodisperse compacts had already attained their maximum densities, but some slight decrease in volume loss with increasing heating rate was noted for polydisperse compacts. This decrease was probably due to the amount of time required to heat the sample from the initiation temperature to the maximum firing temperature, since some slight densification that is not considered significant when compared to the total densification observed as a result of firing could occur over this temperature range. The time spent in heating from 1450°C to 1600°C is 15 minutes at a rate of $10^{\circ}C/_{min}$, while at a rate of $30^{\circ}C/_{min}$ this time is only 5 minutes. This difference is not important when compared to the total firing time used in these studies, but it serves to illustrate that the heating rate can be an issue if the actual firing time to be used is very short, or if the material being fired densifies very rapidly. Thus, densification of a compact made from monodisperse powder would probably be more strongly affected by the heating rate than densification of a polydisperse compact.

It is apparent from this set of studies that compacts made from powders that are of larger particle size and/or are more polydisperse require longer firing times and higher temperatures to achieve the same density as a small monodisperse powder. Retaining

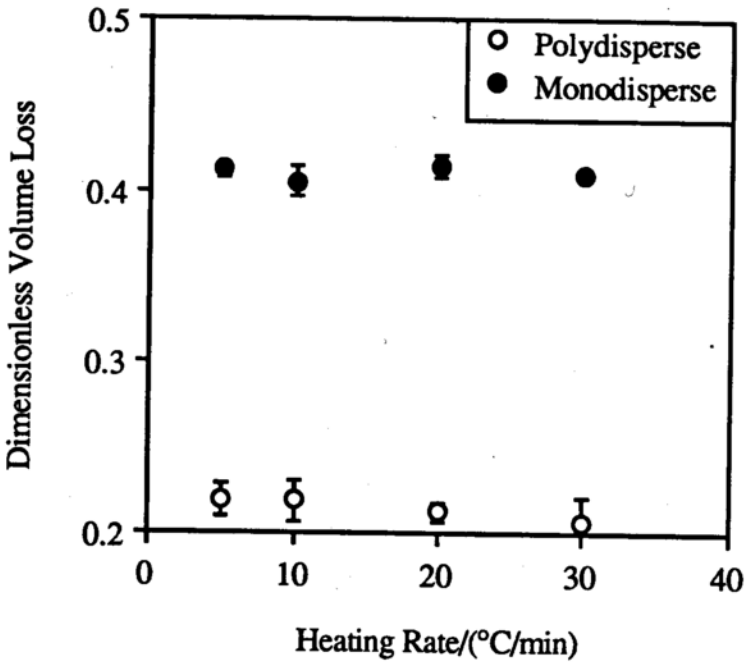

Figure 3.17. Relative volume loss due to heating rate and powder polydispersity. 5% PVP, slurry mixed powders, pressure 10,000 psi, firing time 4 hours, firing temperature 1600°C.
(Data from Tables 3.11(a) and (b).)

Table 3.11(a). Heating rate study, Thermolyne furnace, 5% PVP polydisperse alumina powder.

Values in parentheses represent standard error of five samples.

Rate/ °C/min[a]	Weight loss	Volume loss (Dimensional)[b]	Sintered Porosity (Dimensional)[b]	Sintered Porosity (Archimedes)[c]
5	0.0519 (0.0020)	0.219 (0.010)	0.316 (0.010)	0.296 (0.001)
10	0.0510 (0.0018)	0.219 (0.012)	0.315 (0.011)	0.293 (0.003)
20	0.0517 (0.0018)	0.212 (0.006)	0.323 (0.006)	0.301 (0.001)
30	0.0517 (0.0037)	0.206 (0.015)	0.328 (0.011)	0.306 (0.001)

[a]Compaction pressure 10,000 psi, firing time 4 hours, firing temperature 1600°C.

[b]Bulk method of volume estimation.

[c]Archimedes principle volume estimation.

Table 3.11(b). Heating rate study, Thermolyne furnace, 5% PVP monodisperse alumina powder.

Values in parentheses represent standard error of five samples.

Rate/ °C/min[a]	Weight loss	Volume loss (Dimensional)[b]	Sintered Porosity (Dimensional)[b]	Sintered Porosity (Archimedes)[c]
5	0.0597 (0.0023)	0.412 (0.004)	0.089 (0.007)	0.049 (0.002)
10	0.0604 (0.0008)	0.405 (0.009)	0.099 (0.015)	0.051 (0.001)
20	0.0595 (0.0015)	0.414 (0.007)	0.085 (0.012)	0.048 (0.001)
30	0.0590 (0.0020)	0.409 (0.002)	0.093 (0.002)	0.049 (0.002)

[a]Compaction pressure 10,000 psi, sintering time 4 hours, sintering temperature 1600°C.

[b]Bulk method of volume estimation.

[c]Archimedes principle volume estimation.

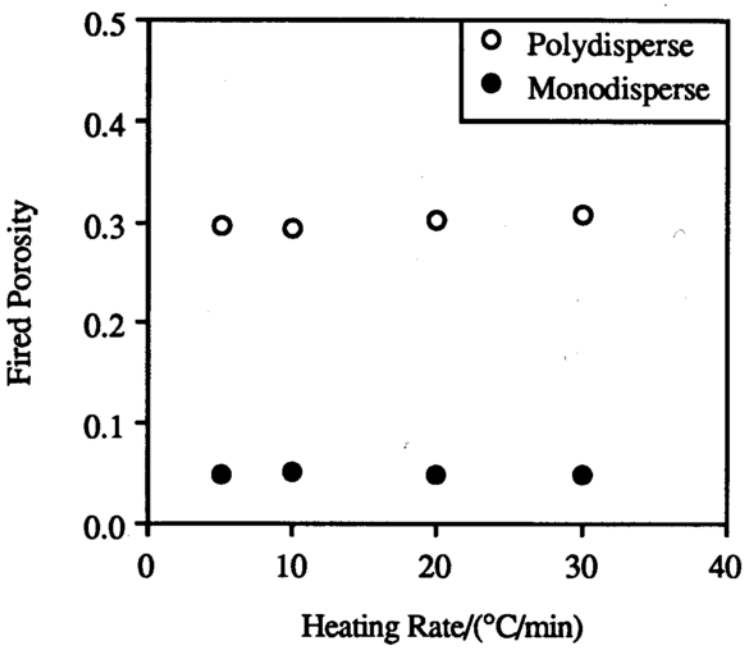

Figure 3.18. Dependence of total porosity on heating rate and powder polydispersity. Porosities obtained by Archimedes method, 5% PVP, slurry mixed powders, pressure 10,000 psi, firing time 4 hours, firing temperature 1600°C.
(Data from Tables 3.11(a) and (b).)

porosity would be quite difficult with a monodisperse powder such as was used here, although it would be a good powder to use if the primary interest was in completely eliminating void space. Thus, polydisperse powders appear to be the best choice for use in production of disks with substantial porosities, such as were required in this work.

This concludes a brief review of the processing studies performed toward this thesis. These studies showed that firing time was the variable that could be most conveniently manipulated to control the final porosities of fired alumina disks, given the specific powder used and equipment available. Knowledge of the relationship between firing time and final total porosity could then be exploited to manufacture disks of a desired range of porosities for analysis of percolation theory parameters, which will be considered next.

IV. PORE STRUCTURE MODELING RESULTS AND DISCUSSION

It is now necessary to obtain a qualitative model of the microstructure of an alumina disk to understand how it may influence the transport of a small molecule. This chapter will apply the percolation scaling relationships discussed in Chapter I to modeling of both the structural and transport-dependent properties of alumina disks, with its objectives being to show that transport of a small water-soluble molecule through a ceramic matrix of relatively low porosity is possible, and to verify that a complicated microstructure such as that possessed by a porous ceramic does exhibit behavior corresponding to the predictions of percolation theory.

A. Morphological Characteristics

A general picture of the microscopic appearance of a fired disk is important for a clear understanding of what is actually being represented by the various percolation parameters. Mercury porosimetry was employed in this work to estimate the diameters of the pore throats, and scanning electron microscopy was used to obtain actual photographs of the microstructure. The results of these studies, and the conceptual picture that may be drawn from them, are the subjects of this section.

1. Pore Size Distributions

Mercury porosimetry was used in this study to determine how firing time (at 1670°C) affected the pore throat diameter in a select series of disks. The disks used were made from powder 3 (listed in Table 3.1), and were heated from 1 to 12 hours. Each analysis used five disks from each firing time.

The diameters of the pore throats that form the constrictions between bulbs in the

overall pore space control the rate at which mercury can be forced into the sample, because capillary pressure will be higher in the throats than in the larger bulbs. Thus, the applied pressure required to overcome this capillary pressure and force mercury into a sample will be dictated by the diameters of the throats, and will not be affected by the bulb diameters, which are needed to estimate the total void space in the sample.

Even though mercury porosimetry is of limited importance in estimating the total void space, it is still useful in determining the average throat diameter. This diameter can dictate the rate at which fluid infiltrates a real release device, and so it will indirectly determine how fast a solubilized drug can escape. Also, knowledge of the throat diameter was needed in this study to verify that the pores through which the model molecule was being transported were not so small as to produce Knudsen diffusion, which can occur if a pore is small enough to influence the mean free path of the random walk of the molecule. Such an effect was not expected to occur in this system.

Figure 4.1 shows a typical throat diameter distribution profile obtained in this study. The apparent decrease in mercury volume (dV) in the sample cell resulting from increasing the pressure from p_i to p_{i+1} is represented by the quantity $^{dV}/_{d(\log p)}$. The minimum intruded pore diameter at p_{i+1} is a function of the contact angle and surface tension of mercury, so if p_{i+1} is known then this diameter may be calculated. For example, the throat diameter controlling the majority of void volume in the set of disks shown in Figure 4.1(a) was 0.9804 μm. The value of dV at a certain pore diameter thus reflects the fraction of the total porosity that is due to pores of that diameter, assuming that all pores are cylindrical. Figure 4.1 shows only the central segment of the entire pore diameter range scanned (0.007 to 250 μm); no significant pore volume was observed at other diameters. It is especially important to note that little additional pore volume was seen below the maximum peak, so any contribution of extremely small pores to uptake of helium during pycnometry (to be

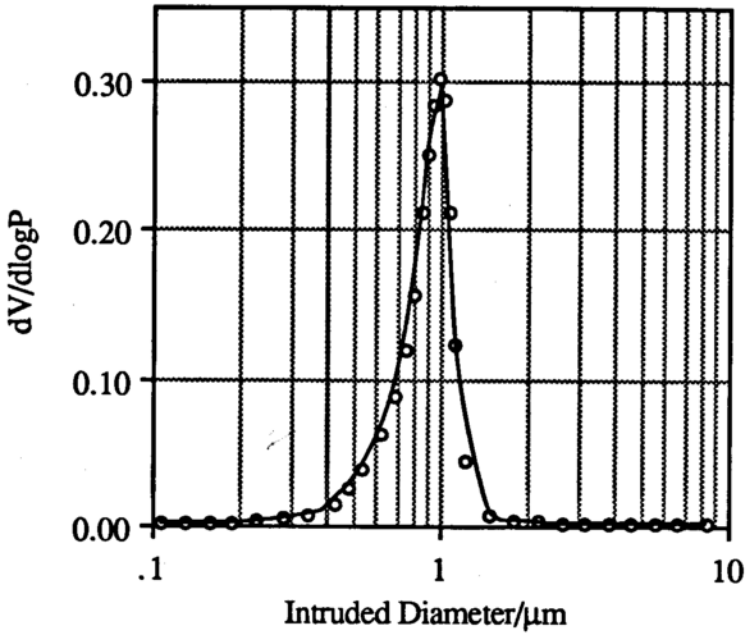

Figure 4.1. Sample mercury porosimetry profile.
Intruded volume at log (applied pressure) versus intruded pore diameter curve, slurry-mixed disks fired for 4 hours.

discussed shortly) may be neglected. Disk sets for other firing times showed similar $^{dV}/_{d(logp)}$ vs. diameter profiles.

A slight decrease in pore diameter at maximum $^{dV}/_{d(logp)}$ with increasing firing time was observed, as is shown in Figure 4.2. Also, the maximum value of $^{dV}/_{d(logp)}$ was seen to decrease also, implying that the total void volume in the disk set was decreasing with increasing firing time. However, since the decrease in pore diameter over the firing time range studied is relatively minor, the effect of this decrease on the transport properties of a disk is expected to be negligible compared to the effect of its complicated morphology on these same properties. From Figure 4.2, all disks appear to exhibit pore throat diameters on the order of 1 μm, a size too large to influence transport of benzoic acid through Knudsen diffusion. Thus, the processing methods outlined in Chapter III seem to primarily influence the total pore space and tortuosity of a disk, but exert negligible influence over the sizes of the individual pores (in the case of the polydisperse disks studied).

The fraction of total void volume, using the parallel tube bundle model, that is attributed to a pore of a certain diameter is not a useful representation of the true pore size distribution, since this model assumes that the entire volume fraction is a pore of that diameter. In reality, the pressure required to force mercury through the pore throats is much higher than that which would be required to force it through the bulbs, so when this higher pressure is reached mercury will flow through the throats and fill all larger pores. The resulting large drop in mercury volume in the sample cell will then be attributed to the throats only. Thus, although the total intruded volume may still be a reasonable measure of the total void space in the sample, it cannot be used to obtain a realistic pore size distribution. The results given in this section therefore only reflect the average throat size in the disk, and give no information regarding the bulb dimensions. This is the primary

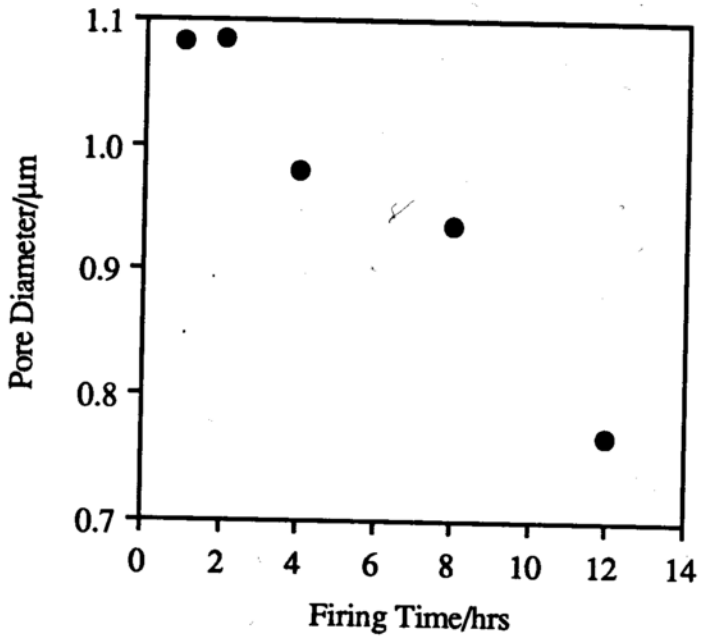

Figure 4.2. Influence of firing time (at 1670°C) on pore diameter at maximum $dV/d(\log p)$.
10% PVP slurry mixed disks, pressure 10,000 psi.
(Data from Table 4.1.)

Table 4.1. Intruded pore diameter at maximum $^{dV}/_{d(logp)}$, mercury porosimetry, 10% PVP slurry mixed disks.
Sample size 5 disks per firing time.

Firing Time/hrs[a]	Fired Porosity	Pore Diam./μm
1	0.344	1.0830
2	0.323	1.0840
4	0.301	0.9804
8	0.244	0.9360
12	0.230	0.7669

[a]Compaction pressure 10,000 psi, sintering temperature 1670°C.

flaw of the parallel tube bundle model commonly used to describe the pore structure in mercury porosimetry, since knowledge of the average bulb diameter is needed to estimate the total void space in the sample.

A possible drawback to porosimetry as used in this study is that of densification of the disk surface to a greater extent than the interior. In such an event, the surface will be less porous than the interior, and the surface pores (which will control intrusion of mercury into the disk) will be smaller than the interior pores. The mean diameter data given in Figure 4.2 would then only reflect the sizes of the surface pores. Disk morphology analysis using scanning electron microscopy was performed in order to observe whether this behavior occurred, as will be discussed next.

2. VISUAL INVESTIGATIONS

Scanning electron microscopy (SEM) was used in this work to obtain an idea of the extremely tortuous nature of the pore structure in a disk, as well as to determine if the surface of a disk was morphologically similar to its interior. To these ends, representative polydisperse and monodisperse disks were sectioned as discussed in Chapter II and both the exterior and interior surfaces were photographed.

Figures 4.3(a) and (b) show exterior and interior surfaces, respectively, of a 10% PVP polydisperse disk that was fired for 4 hours at 1670°C (total porosity 28.4%). Individual grains of aluminum oxide, separated by grain boundaries and interspersed with voids, are evident in these pictures. The two surfaces do indeed look different; specifically, the interior surface appears as a randomly-oriented mass of small plates, but the exterior seems to consist of plates that have been aligned onto the surface plane. The tetrakaidecahedral unit cell typically cited[49] as a model of the grain structure of a ceramic solid is not evident. In either case, the microstructure is extremely complicated, making estimation of the true

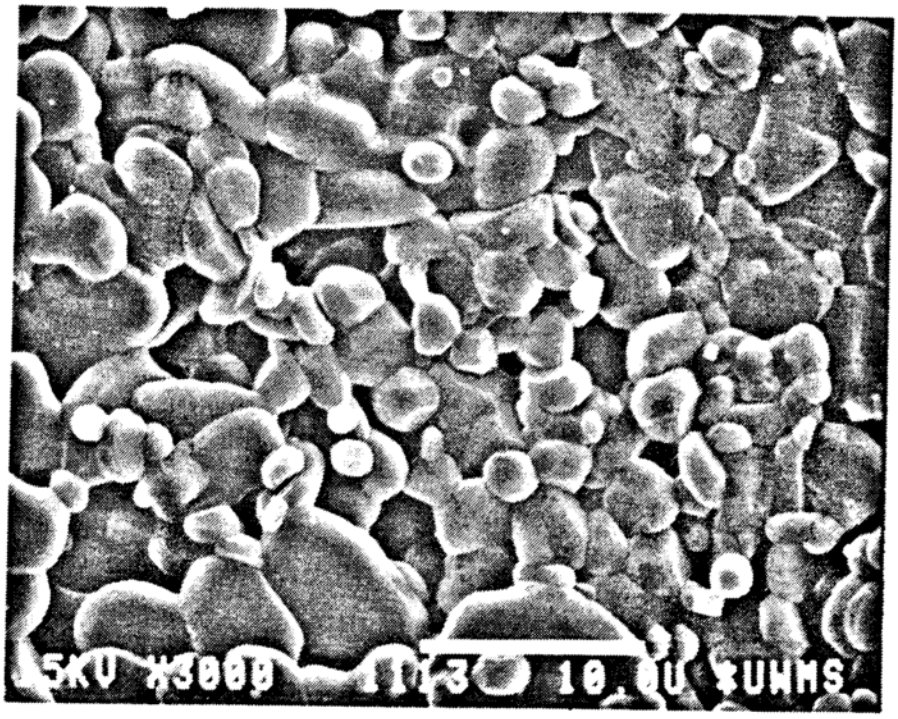

Figure 4.3(a). Scanning electron micrograph of the exterior surface of a polydisperse slurry mixed alumina disk, total porosity 28.4%.
(Scale bar is 10 μm; magnification 3000X.)

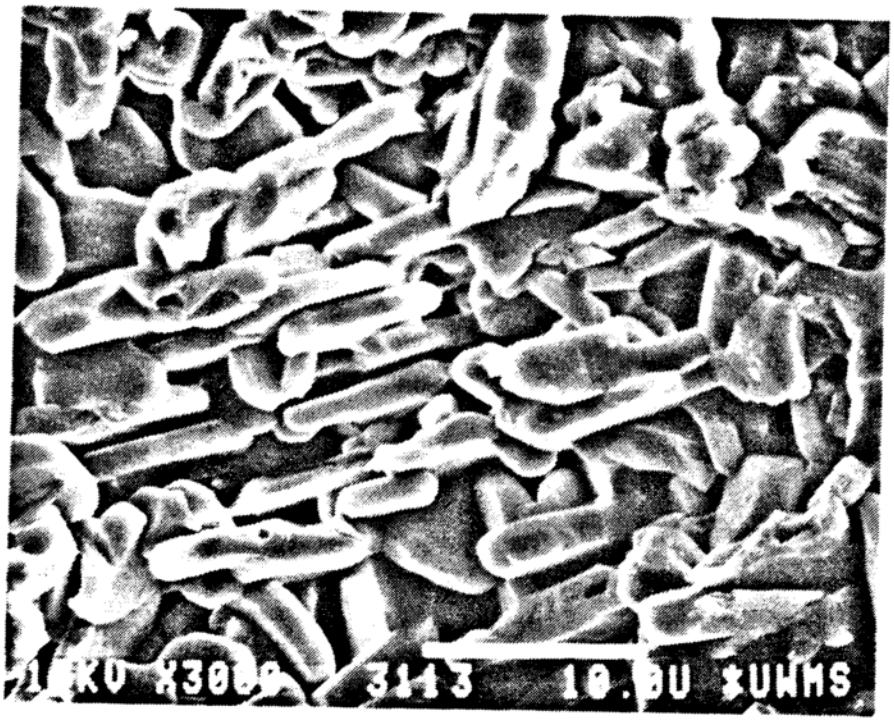

Figure 4.3(b). Scanning electron micrograph of the interior surface of a polydisperse slurry mixed alumina disk, total porosity 28.4%.
(Scale bar is 10 μm; magnification 3000X.)

pore size distribution by visual examination impossible. Relatively little shrinkage of the polydisperse disks occurs during firing, so the interior structure of an unfired compact is probably not much different than that shown in Figure 4.3(b) for the fired disk. Thus, the ceramic powder used in this study is assumed to consist of plate-shaped particles.

Some reduction in porosity due to particle alignment at the surface is evident from visual inspection of Figures 4.3(a) and (b), but how much reduction occurs, and how far this surface layer extends into the disk, are not known. Removing a thin layer of the disk surface, followed by estimating the pore throat size by mercury porosimetry, can aid in determining whether the exterior porosity is lower than that of the interior. Serial sectioning to remove successive thin (i.e. about 50 μm) layers of the disk, followed by SEM imaging of the exposed surface, might be used to estimate the depth of the surface layer. The possibility of non-random pore distribution due to a dense surface layer was not taken into account in this work, but characterization of such a layer would be an important next step in complete description of the properties of alumina disks.

Exterior and interior surfaces of a 5% PVP monodisperse disk fired for 4 hours at 1670°C are shown for comparison in Figures 4.4(a) and (b), respectively. While the same platelike morphology is evident, the individual ceramic grains are smaller than those in Figures 4.3(a) and (b), and very few voids are apparent between them. At lower magnification, these surfaces would exhibit less void space than those shown in Figures 4.3(a) and (b). The very low total porosity of this disk (8.8%) is apparent from the almost total lack of void space. The grains shown on the exterior surface do appear flattened with respect to those in the interior. Thus, the polydisperse and monodisperse compacts exhibit similar morphologies, but the microstructure of a monodisperse compact is smaller and more dense than that of a polydisperse compact as a result of initial particle size and amount of shrinkage during firing. Nonetheless, the two microstructures appear to be similar

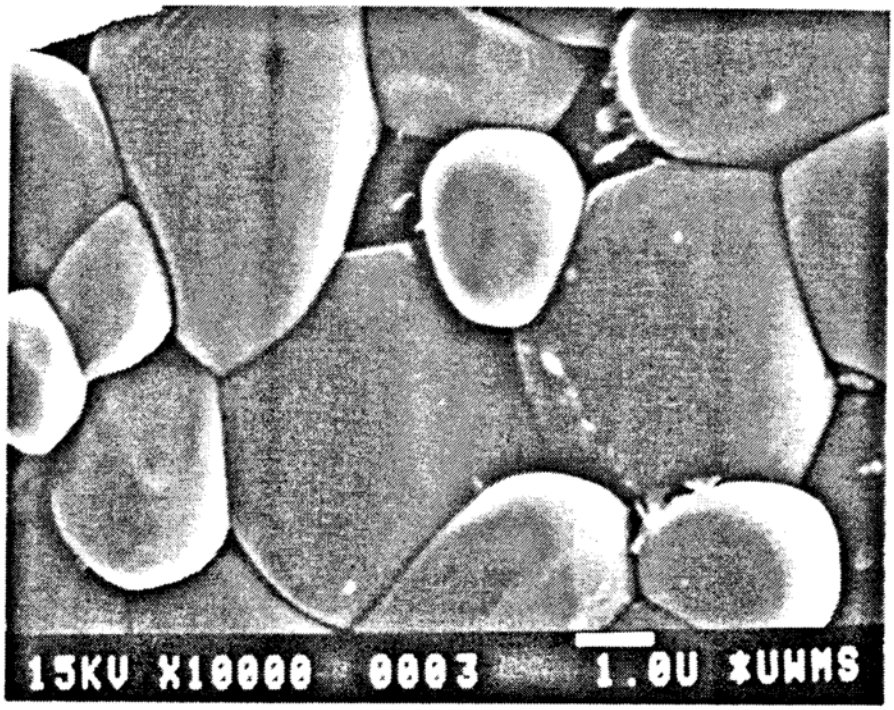

Figure 4.4(a). Scanning electron micrograph of the exterior surface of a monodisperse slurry-mixed alumina disk, total porosity 8.8%.
(Scale bar is 1 μm; magnification 10,000X.)

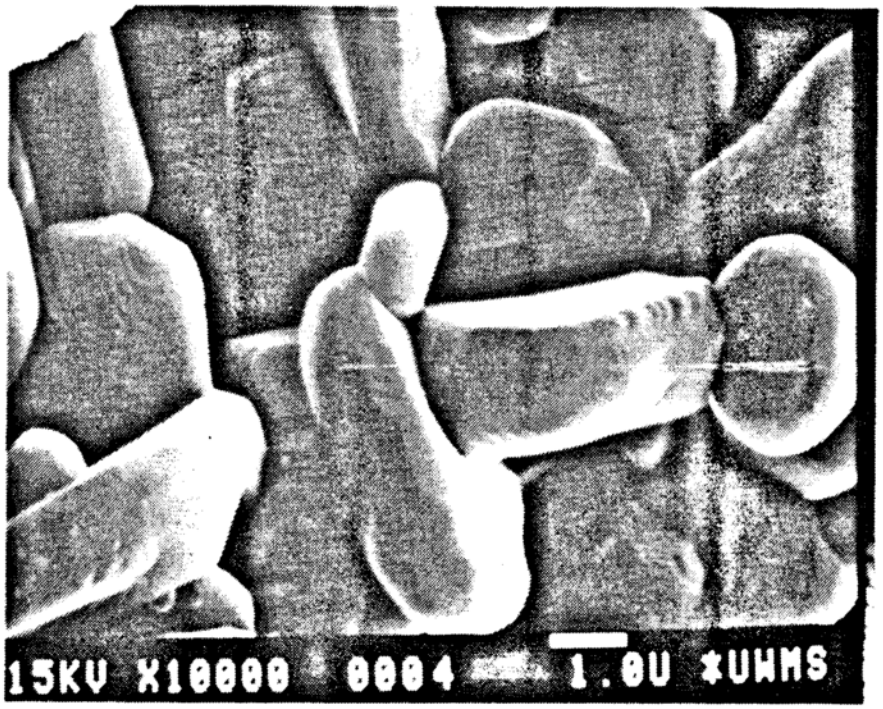

Figure 4.4(b). Scanning electron micrograph of the interior surface of a monodisperse slurry-mixed alumina disk, total porosity 8.8%.
(Scale bar is 1 μm; magnification 10,000X.)

enough to one another that comparisons can be made between disks manufactured from both types of powder, in order to facilitate development of structural percolation theory models to be discussed next.

It is apparent from both sets of photographs that the solid microstructure is not completely random, since regions of stacked plates exist in the disk interior. However, the individual stacked regions appear to be small enough (usually no more than 10 μm in any direction) that this regularity may be neglected. Whether a stacked plate morphology is a better description of the lattice structure than the tetrakaidecahedron mentioned in Chapter I, or alternatively whether regions of stacked plates still result in tetrakaidecahedral pore structures, will be discussed shortly.

B. The Structural Percolation Model

The next step in characterizing the transport properties of an alumina disk is estimation of the volume fraction of total pore space that spans the sample ($\emptyset^A$), which is accessible from both faces of the disk. This is a structural parameter that depends only on the total void fraction of the microstructure, so (ideally) its value should not be influenced by the pore throats or the tortuous nature of the pore space.

Helium and aqueous pycnometry were the two methods used in this work to estimate the volume fraction accessible, by experimentally determining the fraction of total void space resulting from isolated pores (i.e. the volume fraction isolated, $\emptyset^I$) and then calculating $\emptyset^A$. Only helium pycnometry appeared not to be dependent on the pore morphology, so the results it gave were assumed to be the more reliable. Both methods, and determination of the percolation theory parameters $\emptyset^I$, $\emptyset^A$, and the volume fraction of surface pores ($\emptyset^S$) will be discussed in this section.

1. HELIUM PYCNOMETRY

Volume fraction isolated pore results obtained by helium pycnometry indicate that the small molecular size of helium and its low affinity for other materials make it ideal for use in filling very small pores. Thus, helium should easily displace air from very small or dead-end pores in the disk microstructure. Also, movement of helium in and out of the disk should not be influenced by the pore throat diameter. For the purposes of developing percolation models in this work, it was assumed that helium entered every accessible pore space, so that the measured value of $\emptyset^I$ could be taken as the true isolated porosity.

The difficulty in determining $\emptyset^A$ by helium pycnometry in a real system is that the true accessible pore space, which consists only of those pores belonging to sample-spanning clusters, cannot be found directly from knowledge of only $\emptyset^I$ and the total disk porosity $\emptyset$, because helium fills both sample-spanning and surface pores in the disk. Subtraction of $\emptyset^I$ from $\emptyset$ in the real system does not result in $\emptyset^A$ (as is the case in computer models), but rather in the sum shown on the left side of equation (4.1):

$$\emptyset^A + \emptyset^S = \emptyset - \emptyset^I \; ; \; \emptyset > \emptyset_c \; ; \tag{4.1a}$$

$$\emptyset^S = \emptyset - \emptyset^I \; ; \; \emptyset \leq \emptyset_c \; . \tag{4.1b}$$

Recall that the volume fraction accessible is the sum of the backbone ($\emptyset^B$) and dead-end ($\emptyset^D$) pore fractions. Because the scaling relationships outlined in Chapter I are only valid for sample-spanning clusters, the value of $\emptyset^A$, not ($\emptyset^A + \emptyset^S$), must be used to determine the structural critical percolation threshold ($\emptyset_c$) from the accessible scaling law:

$$\emptyset^A \propto (\emptyset - \emptyset_c)^\beta \; ; \tag{1.7a}$$

where β is the universal network exponent[33] assumed equal to 0.4. No explicit relationship exists for $\emptyset^S$; in fact, no mention of such a quantity appears anywhere in the percolation literature. Thus, the manner in which $\emptyset^S$ varies over the entire range of total porosity ($0 \le \emptyset \le 1$) must be assumed in order to calculate its value, and then the resulting value of $\emptyset^A$, for each experimental value of $\emptyset^I$.

In this work, the value of $\emptyset^S$ was taken to be a constant fraction (δ) of $\emptyset^I$ for all $\emptyset$:

$$\delta = \frac{\emptyset^S}{\emptyset^I} \; ; \; 0 \le \emptyset \le 1 \; . \tag{4.2}$$

Physically, this means that the surface pores are assumed to be simply isolated pores that are exposed to the exterior, so these two types of pores taken together should follow the same behavior as the true volume fraction isolated modeled in Figure 1.11 for the infinite lattice, as follows:

$$\left(\emptyset^I + \emptyset^S\right)_{\text{real system}} = \emptyset^I_{\text{infinite lattice}} \; . \tag{4.3}$$

Since $\emptyset^A$ is zero below the percolation threshold, $\emptyset^S$ (and thus δ by extension) can be obtained directly in this region if $\emptyset$ and $\emptyset^I$ are known. This value of δ may then be used to estimate $\emptyset^S$ for every $\emptyset^I$ above $\emptyset_c$, for determining the true values of $\emptyset^A$. Unfortunately, the value of δ must be used to estimate values of $\emptyset^A$ before $\emptyset_c$ can be obtained from equation (1.7a), so how can one tell *a priori* where the region below $\emptyset_c$ lies?. To overcome this problem, the trend in $\emptyset^I$ with decreasing $\emptyset$ for a series of disks of varying porosity is observed to see if these $\emptyset^I$ fall below some apparent threshold value. If so,

these $\emptyset^I$ will be used to find δ. Specifically, if the experimental volume fraction isolated increases linearly with increasing total porosity, then $\emptyset$ is less than $\emptyset_c$ as shown in Figure 1.11. The surface volume fraction is then obtained from the difference ($\emptyset$ - $\emptyset^I$), and δ is found from the ratio of the slope of a line passing through a plot of $\emptyset^S$ versus $\emptyset$ (below $\emptyset_c$) to the slope of a line passing through a plot of $\emptyset^I$ versus $\emptyset$.

Experimentally, all polydisperse disks made in this work exhibited isolated volume fractions that increased with decreasing total porosity (implying that $\emptyset$ was above $\emptyset_c$), so no data could be obtained for $\emptyset^I$ at $\emptyset \leq \emptyset_c$ using these disks. Thus, a further assumption was made that volume fraction isolated data from monodisperse disks could be used to estimate δ, since these data all appeared to fall below the unknown value of $\emptyset_c$ (i.e. $\emptyset^I$ increased with increasing $\emptyset$ for these disks). The assumption that δ obtained from monodisperse disks could be applied to determine $\emptyset^S$ for polydisperse disks seems reasonable, because both microstructures are similar in terms of shapes of both the ceramic grains and the interweaving pore structure.

Values of $\emptyset^I$ and $\emptyset^S$ obtained for the sets of monodisperse disks described in Chapter III are shown in Figure 4.5. Use of these data to fit a line whose slope can be used to find δ is shaky at best, due to the small total porosity range covered and large amount of scatter within this range. Nonetheless, a line may be fit by using the constraint that the volume fraction isolated must be zero at zero total porosity. Best-fit lines were generated for both $\emptyset^I$ and $\emptyset^S$ using this constraint, and are shown on the figure for clarification. These lines have the following profiles:

$$\emptyset^I = 0.68\,\emptyset \;;$$

$$\emptyset^S = 0.32\,\emptyset \;.$$

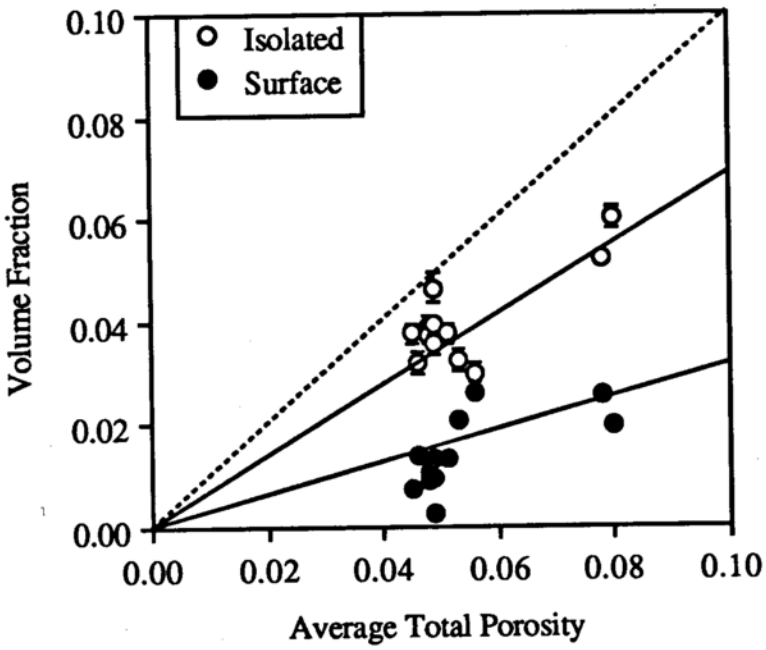

Figure 4.5. Helium pycnometry results, monodisperse 5% PVP disks.
Dotted line represents the required 1:1 relationship between total porosity and the sum of the individual volume fractions.
(Data from Tables 4.2(a), (b), and (c).)

Table 4.2(a). Helium pycnometry, firing time study, Thermolyne furnace, 5% PVP monodisperse alumina disks.

Time/ hrs[a]	Sintered Porosity[b] (Archimedes)	Volume Fraction Isolated[c]	Volume Fraction Surface[c]
1	0.056 (0.002)	0.030 (0.002)	0.026 (0.002)
2	0.046 (0.001)	0.032 (0.002)	0.014 (0.001)
4	0.051 (0.001)	0.038 (0.002)	0.013 (0.001)
8	0.049 (0.002)	0.035 (0.002)	0.014 (0.002)
12	0.048 (0.001)	0.037 (0.002)	0.011 (0.001)

[a]Compaction pressure 10,000 psi, firing temperature 1600°C, heating rate $10°C/_{min}$.

[b]Values in parentheses represent standard error of five samples.

[c]Values in parentheses represent standard error of ten samples.

Table 4.2(b). Helium pycnometry, firing temperature study, Thermolyne furnace, 5% PVP monodisperse alumina disks.

Temp./ °C[a]	Sintered Porosity[b] (Archimedes)	Volume Fraction Isolated[c]	Volume Fraction Surface[c]
1450	0.080 (0.001)	0.060 (0.002)	0.020 (0.001)
1500	0.078 (0.001)	0.052 (0.001)	0.026 (0.001)
1550	0.053 (0.001)	0.032 (0.002)	0.021 (0.001)
1600	0.051 (0.001)	0.038 (0.002)	0.013 (0.001)
1670	0.045 (0.003)	0.038 (0.002)	0.007 (0.002)

[a]Compaction pressure 10,000 psi, firing time 4 hours, heating rate $10°C/_{min}$.

[b]Values in parentheses represent standard error of five samples.

[c]Values in parentheses represent standard error of ten samples.

Table 4.2(c). Helium pycnometry, heating rate study, Thermolyne furnace, 5% PVP monodisperse alumina disks.

Rate/ °C/min[a]	Sintered Porosity[b] (Archimedes)	Volume Fraction Isolated[c]	Volume Fraction Surface[c]
5	0.049 (0.002)	0.039 (0.001)	0.010 (0.001)
10	0.051 (0.001)	0.038 (0.002)	0.013 (0.001)
20	0.048 (0.001)	0.039 (0.002)	0.009 (0.001)
30	0.049 (0.002)	0.046 (0.003)	0.003 (0.002)

[a]Compaction pressure 10,000 psi, firing time 4 hours, firing temperature 1600°C.

[b]Values in parentheses represent standard error of five samples.

[c]Values in parentheses represent standard error of ten samples.

The ratio of the $\emptyset^S$ slope to the $\emptyset^I$ slope then results in the following constant value of δ:

$$\delta = 0.47 \ .$$

Finally, $\emptyset^A$ values for all polydisperse disks analyzed by helium pycnometry in this work were found using the following equation:

$$\emptyset^A = \emptyset - (1 + \delta)\emptyset^I \ ; \ \emptyset \geq \emptyset_c \ . \tag{4.3}$$

Note that the surface porosity does not appear in equation (4.3), because once δ has been determined explicit representation of $\emptyset^S$ is no longer necessary due to the manner in which it was defined. Alternatively, a plot of $\emptyset^S = (\emptyset - \emptyset^I)$ versus $\emptyset^I$ for $\emptyset < \emptyset_c$ will yield a line of slope equal to δ directly; the method shown in Figure 4.5 was used for illustration of the dependence of the surface volume fraction on $\emptyset^I$.

Most polydisperse disks made in the studies outlined in Chapter III were analyzed by helium pycnometry to find $\emptyset^I$ and $\emptyset^A$. The results of these studies appear in the following figures. In all cases, the isolated porosity was observed to increase with decreasing total porosity as mentioned. With the exceptions of the results shown in Figures 4.4(a) and (b), all total porosities were obtained by varying the firing time at 1670°C.

Figure 4.6 summarizes the results obtained for the polydisperse disks made in the same study as the monodisperse disks shown in Figure 4.5. It is important to note from Figure 4.6 that, even though firing time, firing temperature, and heating rate were varied in this study, the resultant data all follow the same profile, suggesting that the microstructure retained the same general form irrespective of the conditions used in processing. This observation can be used to justify grouping all $\emptyset^A$ data generated in this work together for

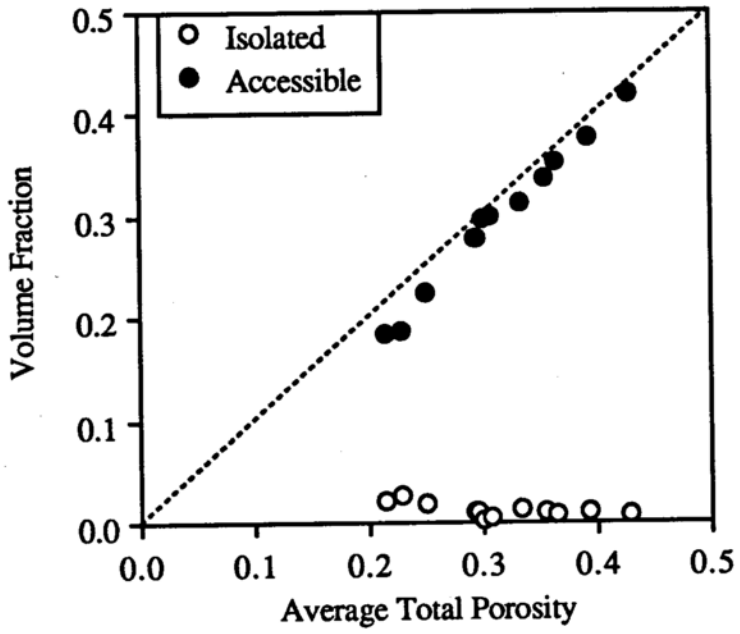

Figure 4.6. Helium pycnometry results, polydisperse 5% PVP disks.
(Data from Tables 4.3(a), (b), and (c).)

Table 4.3(a). Helium pycnometry, firing time study, Thermolyne furnace, 5% PVP polydisperse alumina disks.

Time/ hrs[a]	Sintered Porosity[b] (Archimedes)	Volume Fraction Isolated[c]	Volume Fraction Accessible[c]
1	0.364 (0.001)	0.007 (0.002)	0.354 (0.001)
2	0.333 (0.002)	0.013 (0.003)	0.314 (0.003)
4	0.293 (0.003)	0.011 (0.003)	0.276 (0.003)
8	0.251 (0.001)	0.018 (0.003)	0.224 (0.002)
12	0.228 (0.003)	0.027 (0.002)	0.189 (0.003)

[a]Compaction pressure 10,000 psi, firing temperature 1600°C, heating rate $10°C/_{min}$.

[b]Values in parentheses represent standard error of five samples.

[c]Values in parentheses represent standard error of ten samples.

Table 4.3(b). Helium pycnometry, firing temperature study, Thermolyne furnace, 5% PVP polydisperse alumina disks.

Temp./ °C[a]	Sintered Porosity[b] (Archimedes)	Volume Fraction Isolated[c]	Volume Fraction Accessible[c]
1450	0.429 (0.002)	0.007 (0.003)	0.419 (0.003)
1500	0.394 (0.002)	0.012 (0.003)	0.376 (0.002)
1550	0.354 (0.001)	0.012 (0.003)	0.336 (0.002)
1600	0.293 (0.003)	0.011 (0.003)	0.276 (0.003)
1670	0.215 (0.002)	0.021 (0.005)	0.184 (0.003)

[a]Compaction pressure 10,000 psi, firing time 4 hours, heating rate $10°C/_{min}$.

[b]Values in parentheses represent standard error of five samples.

[c]Values in parentheses represent standard error of ten samples.

Table 4.3(c). Helium pycnometry, heating rate study, Thermolyne furnace, 5% PVP polydisperse alumina disks.

Rate/ °C/min[a]	Sintered Porosity[b] (Archimedes)	Volume Fraction Isolated[c]	Volume Fraction Accessible[c]
5	0.296 (0.001)	0.012 (0.002)	0.279 (0.002)
10	0.293 (0.003)	0.011 (0.003)	0.276 (0.003)
20	0.301 (0.001)	0.003 (0.003)	0.296 (0.002)
30	0.306 (0.001)	0.005 (0.002)	0.298 (0.001)

[a]Compaction pressure 10,000 psi, firing time 4 hours, firing temperature 1600°C.

[b]Values in parentheses represent standard error of five samples.

[c]Values in parentheses represent standard error of ten samples.

use in determining $\emptyset_c$ from equation (1.7a), as will be seen shortly.

Figure 4.7 shows $\emptyset^A$ information for 5% PVP slurry mixed disks. These data were generated before and after aqueous pycnometry was performed on the disks, in order to determine if the observed weight loss from sonicating in water resulted in a change in the accessible porosity. The accessible porosity was seen to drop slightly after sonication, which could reflect some pore blockage due to disrupting the microstructure. However, the decrease in $\emptyset^A$ is simply thought to be an artifact of the weight loss, since the observed weight after sonication was used to re-calculate a new value for $\emptyset$ before estimating $\emptyset^I$. The small change in $\emptyset^A$ before and after sonication makes view of the loss as an artifact more likely, so it may be assumed that no significant change in the microstructure occurs through sonication. With this assumption, values of $\emptyset^A$ before and after sonication can both be used in estimation of $\emptyset_c$.

Similarly, Figure 4.8 depicts $\emptyset^A$ and $\emptyset^I$ before and after sonication for 5% PVP ball milled disks. The same decrease in $\emptyset^A$ after sonication is observed. The disk sample with the lowest total porosity ($\emptyset = 0.130$, firing time 36 hours) was seen to attain a volume fraction accessible of zero, so the value of $\emptyset_c$ obtained by fitting equation (1.7a) should be very close to $\emptyset = 0.130$. Values of $\emptyset^A$ for slurry mixed disks and ball milled disks are very similar, so these data also may be used together to obtain $\emptyset_c$.

Volume fraction accessible results for 10% PVP slurry mixed disks are shown in Figure 4.9. These results are not significantly different than those obtained for the 5% PVP disks, which may be due to the small change in total porosity resulting from increasing the weight percentage of PVP used in the initial powder from 5% to 10% (as shown in Figure 3.2). Raising the amount of PVP used to 20% could possibly have a more pronounced effect on $\emptyset^A$. Thus, $\emptyset^A$ data for disks made from both 5% and 10% PVP are similar enough to be applied together to determine $\emptyset_c$.

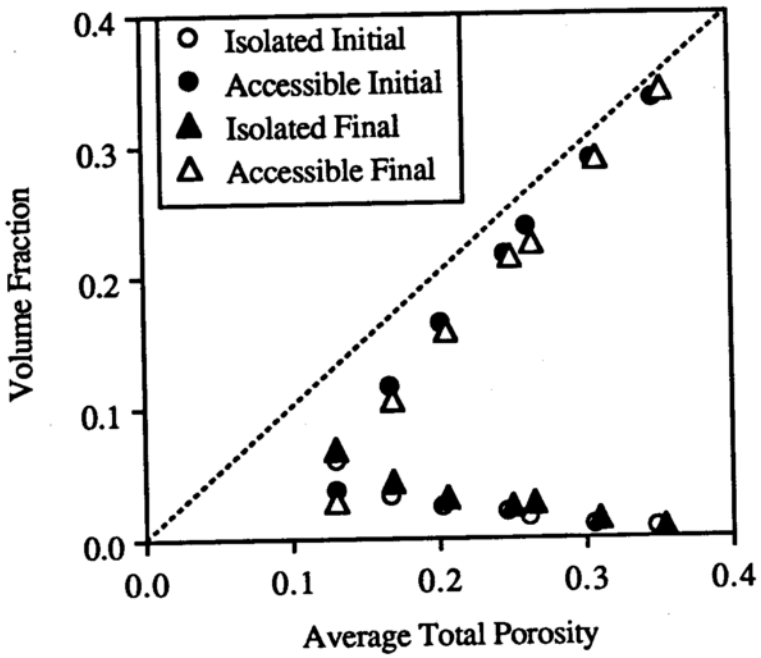

Figure 4.7. Helium pycnometry results, before and after disk sonication, slurry mixed 5% PVP disks.
(Data from Tables 4.4(a) and (b).)

Table 4.4(a). Helium pycnometry, 5% PVP slurry mixed disks, before sonication.

Time/ hrs[a]	Sintered Porosity[b]	Volume Fraction Isolated[c]	Volume Fraction Accessible[c]
1	0.349 (0.008)	0.009 (0.003)	0.336 (0.005)
2	0.306 (0.011)	0.011 (0.003)	0.290 (0.007)
4	0.262 (0.006)	0.017 (0.003)	0.237 (0.004)
8	0.247 (0.012)	0.020 (0.003)	0.217 (0.007)
12	0.201 (0.006)	0.025 (0.003)	0.164 (0.004)
24	0.167 (0.013)	0.034 (0.004)	0.117 (0.009)
36	0.129 (0.016)	0.061 (0.003)	0.038 (0.010)

[a]Compaction pressure 10,000 psi, firing temperature 1670°C.

[b]Values in parentheses represent standard error of six samples.

[c]Values in parentheses represent standard error of ten samples.

Table 4.4(b). Helium pycnometry, 5% PVP slurry mixed disks, after sonication.

Time/ hrs[a]	Sintered Porosity[b]	Volume Fraction Isolated[c]	Volume Fraction Accessible[c]
1	0.354 (0.008)	0.008 (0.002)	0.342 (0.005)
2	0.310 (0.011)	0.014 (0.002)	0.289 (0.007)
4	0.265 (0.006)	0.027 (0.001)	0.225 (0.004)
8	0.250 (0.012)	0.024 (0.001)	0.215 (0.006)
12	0.205 (0.006)	0.032 (0.001)	0.158 (0.003)
24	0.169 (0.013)	0.043 (0.001)	0.106 (0.007)
36	0.130 (0.016)	0.069 (0.001)	0.028 (0.009)

[a]Compaction pressure 10,000 psi, firing temperature 1670°C.

[b]Values in parentheses represent standard error of six samples.

[c]Values in parentheses represent standard error of ten samples.

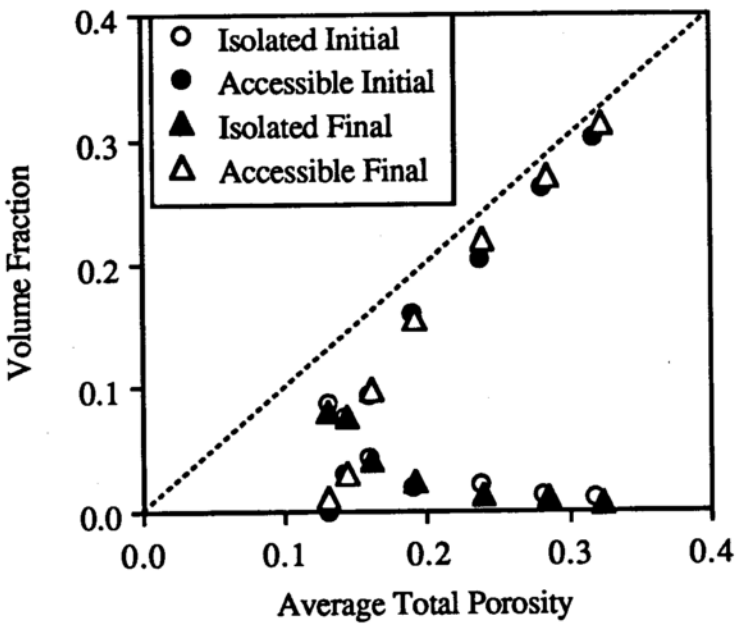

Figure 4.8. Helium pycnometry results, before and after disk sonication, ball milled 5% PVP disks.
(Data from Tables 4.5(a) and (b).)

Table 4.5(a). Helium pycnometry, 5% PVP ball milled disks, before sonication.

Time/ hrs[a]	Sintered Porosity[b]	Volume Fraction Isolated[c]	Volume Fraction Accessible[c]
1	0.318 (0.007)	0.012 (0.002)	0.300 (0.005)
2	0.281 (0.007)	0.013 (0.002)	0.262 (0.005)
4	0.237 (0.008)	0.022 (0.003)	0.205 (0.005)
8	0.189 (0.009)	0.020 (0.003)	0.160 (0.006)
12	0.159 (0.007)	0.044 (0.003)	0.094 (0.005)
24	0.141 (0.006)	0.076 (0.003)	0.030 (0.005)
36	0.130 (0.016)	0.089 (0.003)	0.000 (0.009)

[a]Compaction pressure 10,000 psi, firing temperature 1670°C.

[b]Values in parentheses represent standard error of six samples.

[c]Values in parentheses represent standard error of ten samples.

Table 4.5(b). Helium pycnometry, 5% PVP ball milled disks, after sonication.

Time/ hrs[a]	Sintered Porosity[b]	Volume Fraction Isolated[c]	Volume Fraction Accessible[c]
1	0.323 (0.007)	0.007 (0.000)	0.313 (0.004)
2	0.286 (0.007)	0.011 (0.001)	0.270 (0.004)
4	0.240 (0.008)	0.014 (0.000)	0.219 (0.004)
8	0.192 (0.009)	0.024 (0.000)	0.157 (0.005)
12	0.161 (0.007)	0.041 (0.000)	0.100 (0.004)
24	0.143 (0.006)	0.076 (0.000)	0.031 (0.003)
36	0.130 (0.016)	0.081 (0.002)	0.011 (0.009)

[a]Compaction pressure 10,000 psi, firing temperature 1670°C.

[b]Values in parentheses represent standard error of six samples.

[c]Values in parentheses represent standard error of ten samples.

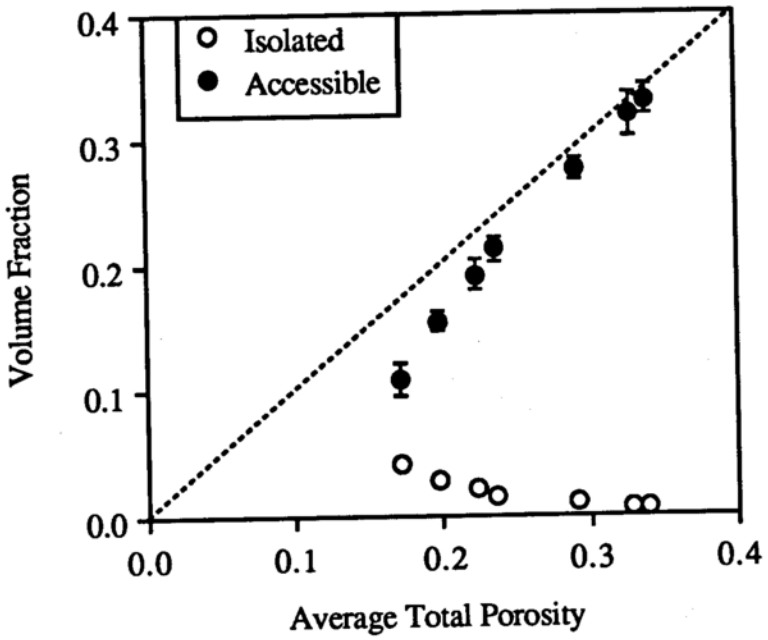

Figure 4.9. Helium pycnometry results, slurry mixed 10% PVP disks.
(Data from Table 4.6.)

Table 4.6. Helium pycnometry, 10% PVP slurry mixed disks.

Time/ hrs[a]	Disks	Sintered Porosity[b]	Trials	Volume Fraction Isolated[c]	Volume Fraction Accessible[c]
1	5	0.340 (0.021)	36	0.006 (0.003)	0.331 (0.012)
2	5	0.329 (0.032)	22	0.006 (0.003)	0.320 (0.018)
4	4	0.291 (0.013)	10	0.010 (0.004)	0.276 (0.009)
8	8	0.236 (0.016)	21	0.016 (0.003)	0.212 (0.009)
12	6	0.223 (0.020)	21	0.021 (0.003)	0.192 (0.011)
24	9	0.198 (0.012)	21	0.029 (0.002)	0.155 (0.007)
36	10	0.171 (0.025)	21	0.042 (0.002)	0.109 (0.014)

[a]Compaction pressure 10,000 psi, firing temperature 1670°C.

[b]Values in parentheses represent standard error of number of disks listed.

[c]Values in parentheses represent standard error of number of trials listed.

Having made arguments for grouping all $\emptyset^A$ data together, an estimate of $\emptyset_c$ can now be obtained using equation (1.7a). (Even if these arguments are invalid, in this case the overall scatter in the complete set of data is expected to be within the experimental error of the pycnometry method, so grouping the data should not increase the randomness of the model.).

A summary of the Aldrich polydisperse ($\emptyset^A$,$\emptyset$) data set used to obtain $\emptyset_c$ is shown in Figure 4.10. These data are fit to Equation (1.7a) using the following approximation:

$$\emptyset^A = a\,(\emptyset - \emptyset_c)^{0.4} \;; \tag{4.4}$$

where a is a pre-exponential factor that is fit along with $\emptyset_c$. This equation is fit to $\emptyset^A$ and $\emptyset$ by a nonlinear regression analysis package (Systat Inc., Evanston, IL). The parameters obtained are as follows:

$$\emptyset_c = 0.129 \pm 0.00 \;;$$

$$a = 0.56 \pm 0.01 \;;$$

where the errors represent the standard error of fit. The value 0.129 thus represents the total porosity at which a pore becomes sample-spanning, and the resulting scaling relationship describes the way in which the sample-spanning porosity increases above the threshold. This scaling relationship only describes how the distribution of pore space varies between accessible and isolated, and not how this distribution influences transport.

The percolation scaling laws are only strictly valid near the critical percolation threshold, and deviate from the behavior exhibited by a real system as the total porosity

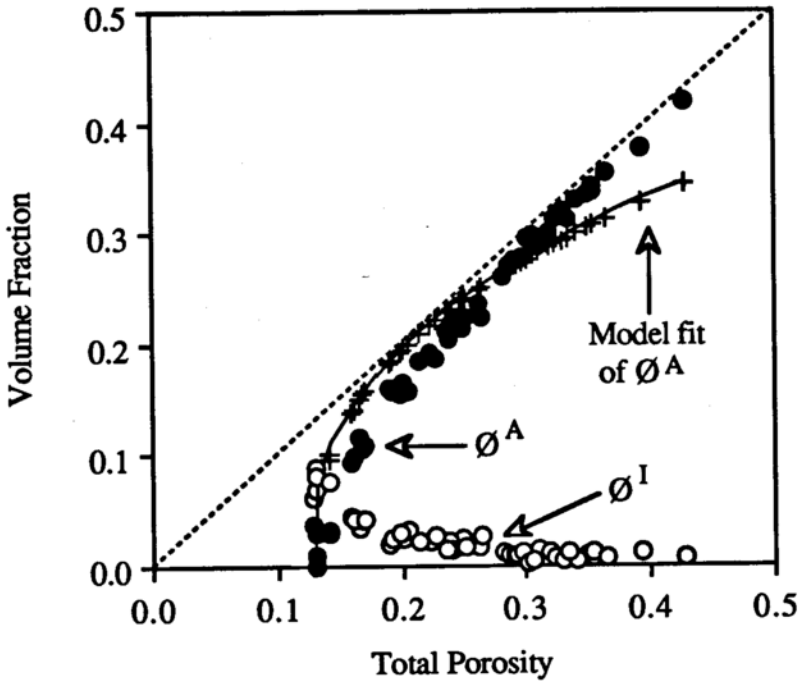

Figure 4.10. Summary of helium pycnometry results for polydisperse 5% and 10% PVP disks.

Model fit of $\emptyset^A$ using equation (4.4) is shown, note generally poor model fit using the critical exponent $\beta = 0.4$.

increases above $\emptyset_c$ and the sizes of the individual pores become less important in controlling the distribution of void space[30]. The experimental total porosities shown in Figure 4.10 can be used in equation (4.4) to obtain model values of $\emptyset^A$, in order to determine the range of total porosities over which equation (4.4) is valid. The resulting profile, also shown in Figure 4.10, indicates that the model should not be used to predict the volume fraction accessible for total porosities greater than about 0.250, and does not generally fit the data well at any value of $\emptyset$. Above $\emptyset = 0.250$, experimental values of $\emptyset^A$ approach a 1:1 relationship with the total porosity in a manner independent of the distribution of void space in the matrix, while the fitted scaling law predicts that they will level off. Although in some respects the usefulness of the volume fraction accessible model is diminished by its small range of application and poor fit, it is this same range that is most important in control of transport through the matrix. More will be said regarding the structural percolation model once the similar transport-dependent model has been derived for comparison, after the results obtained by aqueous pycnometry have briefly been discussed.

2. AQUEOUS PYCNOMETRY

This type of pycnometry was not pursued in more than one study in this work, for three reasons. First, helium pycnometry was easier to perform, and proved to be more precise, than aqueous pycnometry. Also, it was not clear what changes occurred in the disk microstructure that were responsible for weight loss during sonication. Finally, invasion of the entire pore space by water seemed to be hindered by capillary pressure, such that water may not have been able to enter very small or dead-end pores. Sonication was performed to facilitate intrusion of water into dead-end pores by disrupting the air trapped in those pores, but whether or not this occurred in all the pores, some of the pores,

or no pores could not be determined from the results.

Variation of $\emptyset^A$ with total porosity for slurry mixed and ball milled 5% PVP disks is shown in Figures 4.11 and 4.12, respectively. The useful observation that may be obtained from this aqueous pycnometry study is that disks with higher total porosity appear to contain a greater number of very small and/or dead-end pores than those with porosities close to $\emptyset_c$, since the volume fraction accessible found by aqueous pycnometry deviated more drastically from that found by helium pycnometry as the total porosity increased. Disks with high total porosities were fired for shorter periods of time that may not have been sufficient for elimination of very small pores to take place, resulting in a larger number of small pores that were inaccessible to water due to capillary pressure, but were accessible to helium. The contribution of these small pores to the total pore volume became negligible as the threshold was approached. Unfortunately, the data shown in Figures 4.11 and 4.12 do not allow for estimation of the fraction of dead-end pore space, because some unknown fraction of this pore space was probably intruded by water during sonication. Thus, only limited insight into how the microstructure is affected by firing time was possible from these results.

An idea of the extent to which firing time affects adherence between grains in the microstructure can be obtained from a plot of the fraction of initial disk weight lost through sonication versus firing time. Such a plot is shown in Figure 4.13, and illustrates that more weight was lost at short firing times. Weight loss at short firing times is probably a result of removing small grains, mainly on the surface, that had only weakly adhered to other grains through surface forces. These grains are eventually incorporated into the solid matrix at longer firing times. Removal of these particles would thus not result in any noticeable change in the internal microstructure.

This concludes discussion of the structural percolation properties of the porous

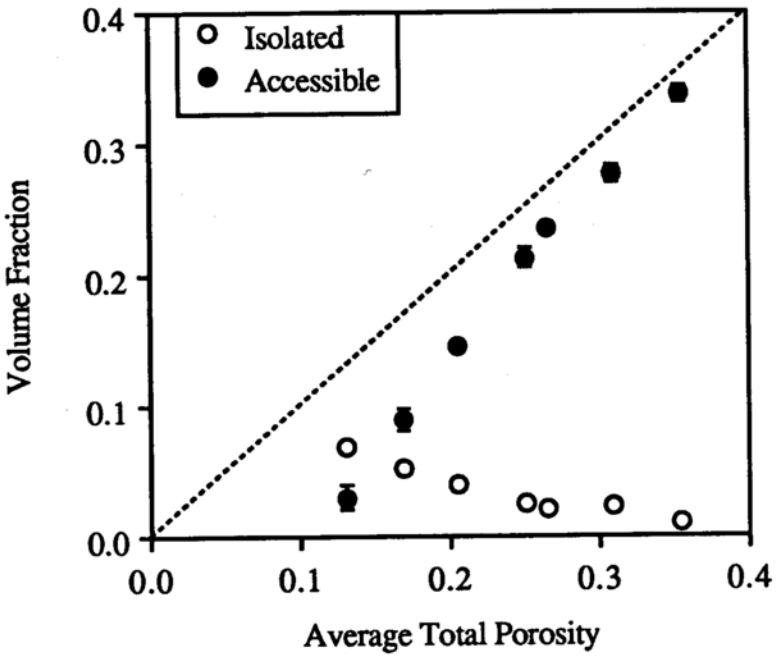

Figure 4.11. Aqueous pycnometry results, slurry mixed 5% PVP disks.
(Data from Table 4.7(a).)

Table 4.7(a). Aqueous pycnometry, 5% PVP slurry mixed disks, after sonication. Values in parentheses represent standard error of six samples.

Time/ hrs[a]	Weight loss due to sonication	Sintered Porosity	Volume Fraction Isolated	Volume Fraction Accessible
1	0.0041	0.354 (0.008)	0.011 (0.004)	0.338 (0.006)
2	0.0028	0.310 (0.011)	0.022 (0.001)	0.277 (0.006)
4	0.0018	0.265 (0.006)	0.021 (0.002)	0.235 (0.004)
8	0.0013	0.250 (0.012)	0.025 (0.003)	0.213 (0.008)
12	0.0010	0.205 (0.006)	0.040 (0.002)	0.146 (0.004)
24	0.0007	0.169 (0.013)	0.053 (0.003)	0.090 (0.008)
36	0.0004	0.130 (0.016)	0.068 (0.003)	0.030 (0.009)

[a]Compaction pressure 10,000 psi, heating temperature 1670°C.

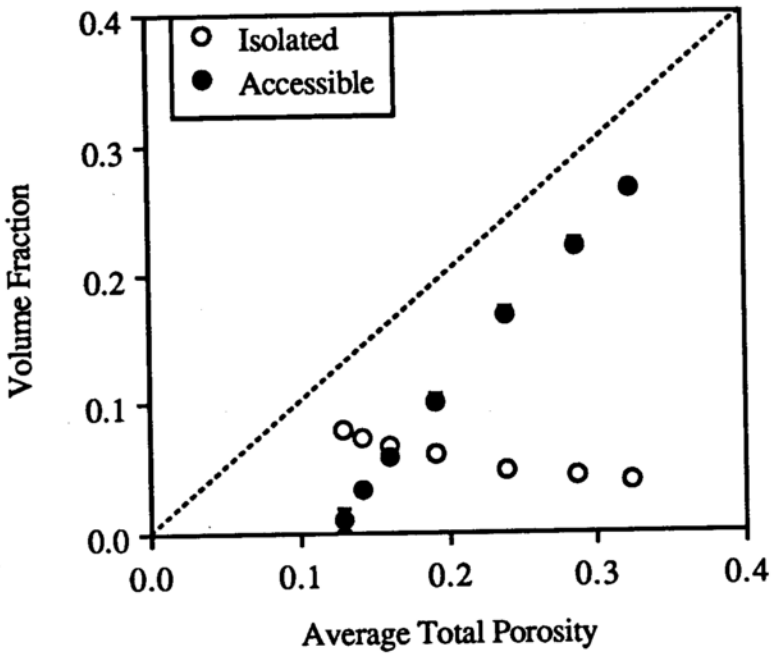

Figure 4.12. Aqueous pycnometry results, ball milled 5% PVP disks.
(Data from Table 4.7(b).)

Table 4.7(b). Aqueous pycnometry, 5% PVP ball milled disks, after sonication. Values in parentheses represent standard error of six samples.

Time/ hrs[a]	Weight loss due to sonication	Sintered Porosity	Volume Fraction Isolated	Volume Fraction Accessible
1	0.0032	0.323 (0.007)	0.040 (0.002)	0.265 (0.005)
2	0.0023	0.286 (0.007)	0.044 (0.002)	0.222 (0.004)
4	0.0020	0.240 (0.008)	0.048 (0.002)	0.169 (0.005)
8	0.0012	0.192 (0.009)	0.061 (0.002)	0.102 (0.005)
12	0.0010	0.161 (0.007)	0.068 (0.001)	0.060 (0.004)
24	0.0009	0.143 (0.006)	0.074 (0.003)	0.034 (0.004)
36	0.0003	0.130 (0.016)	0.081 (0.001)	0.011 (0.009)

[a]Compaction pressure 10,000 psi, heating temperature 1670°C.

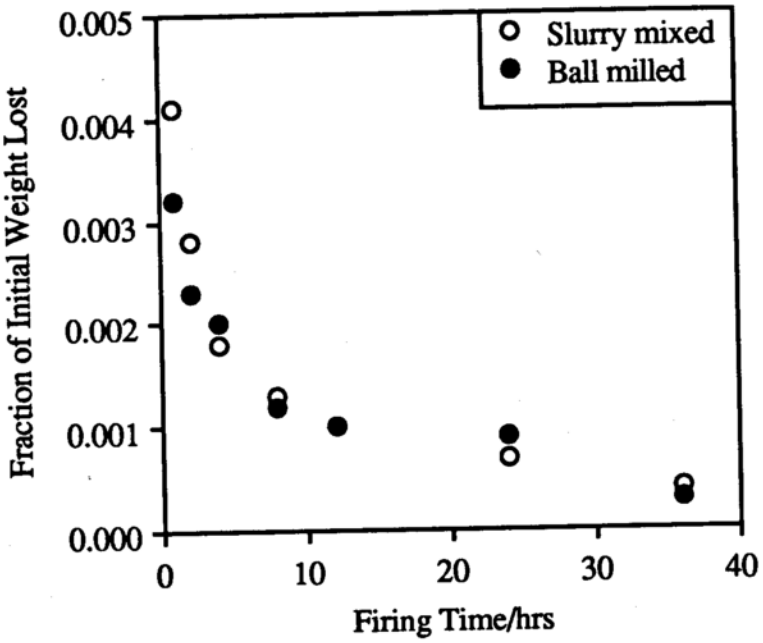

Figure 4.13. Fraction of initial disk weight lost from sonication, 5% PVP disks. (Data from Tables 4.7(a) and (b).)

alumina matrix. Next, the manner in which these pores control transport of a small model molecule will be reviewed.

C. The Transport-Dependent Percolation Model

Unlike the structural percolation model, the transport-dependent model is expected to be influenced by both the pore throat diameter and the tortuous nature of the pore space. The diameter of a pore throat will dictate, through capillary pressure considerations, whether or not an aqueous medium (the "solvent" in this discussion) will be able to flow through this throat and into remainder of the pore, in analogy to the uptake of water during aqueous pycnometry. The tortuous nature of the pore space will govern the length of time required to completely perfuse the accessible pores with solvent, and also will control the time required for a solute molecule to diffuse through a sample-spanning pore. The volume distribution of pores that are perfused with solvent will determine the mass flux of solute through the disk. The fraction of the total pore space that is filled with solvent and thus available for transport (the volume fraction effective, $\emptyset^E$) of benzoic acid may be modeled using both the infinite lattice model and the finite-size scaling correction, as is the subject of this section.

1. Diffusion on the Infinite Lattice

The assumption of the infinite lattice may be applied to the study of diffusion of benzoic acid across a ceramic disk if the diameter of an individual pore throat is negligible compared to the linear disk thickness. In this study, the throat diameter of 1 μm obtained by porosimetry was assumed to be negligibly small compared to the overall disk thickness of about 2.5 mm. Use of a very small molecule such as benzoic acid as the solute allows the further assumption to be made that the pore diameter does not influence transport at

steady-state through Knudsen diffusion. The total water-filled pore space, and the tortuous nature of this pore space, will be the only parameters controlling the time required for the molecule to diffuse from one side of the disk to the other.

As discussed in Chapter I, the bulk diffusivity (D_B) of benzoic acid through a disk of total porosity Ø may be obtained from observing the steady-state concentration gradient across the disk as a function of time. The fraction of total porosity effective for transport ($Ø^E$) is then equal to the ratio of D_B to the diffusivity (D_{aq}) that would be expected if the total porosity were 100%:

$$Ø^E = \frac{D_B}{D_{aq}} . \qquad (1.12)$$

Recall from Chapter II that $D_{aq} = 1.45 \times 10^{-5}$ cm^2/s.

A very chaotic unsteady-state period that can last several days is exhibited at the beginning of each transport experiment. The difference in benzoic acid concentration between the donor and receptor compartments during this period is almost random, so no useful information can be obtained during this time. This period is probably caused by accumulation, and occasional release, of benzoic acid in dead-end pore spaces that have been filled with solvent. The unsteady-state period ends when equilibrium is established between the benzoic acid concentration in the backbone pore structure and the concentration in the dead-end pores. Thus, at steady-state the backbone porosity ($Ø^B$) governs diffusion of benzoic acid through the disk; however, it must be kept in mind that $Ø^B$ is a structural parameter in the same sense as $Ø^A$, and so cannot be determined through a transport experiment. $Ø^B$ and $Ø^E$ can be obtained from the same set of data only if the assumption is made that the entire backbone pore space is available for transport, which cannot be done in this system.

The values of D_B used to calculate each $\emptyset^E$ in this study were obtained with the Stokes diaphragm cell apparatus described in Chapter II. Two experiments were performed with 5% PVP slurry mixed polydisperse disks; all others used 10% PVP slurry mixed polydisperse disks. The total porosities of the disks used were controlled by varying the firing time from 1 to 24 hours. The chamber containing the donor solution was routinely varied between top and bottom to determine if D_B was affected by convection due to gravity, but no such effect was observed.

The values of $\emptyset^E$ obtained in this study are summarized in Figure 4.14. The data exhibit a parabolic profile, analogous to the simulated $\emptyset^E$ profile shown in Figure 1.11. The slight initial rate of increase in $\emptyset^E$ with total porosity illustrates the difficulty involved in obtaining accurate estimates of $\emptyset^E$ in the immediate region of the percolation threshold, in the respect that transport in a disk with total porosity near or at this threshold can occur, but so slowly and to such a small extent as to not be observable. The large amount of scatter in $\emptyset^E$ at larger values of $\emptyset$ is thought to be a result of the declining influence of individual pores on the diffusivity at higher porosity. Near $\emptyset^E = 0$, however, the data increase smoothly with increasing total porosity, which should result in close approximation to the infinite lattice assumption.

To find $\emptyset_c$ on the infinite lattice, the following scaling relationship for the volume fraction effective above the percolation threshold is assumed:

$$\emptyset^E \propto (\emptyset - \emptyset_c)^{\mu} \; ; \qquad (1.11a)$$

where μ is the universal conductivity exponent, taken to be equal to the value of 2.0 commonly cited in the literature[38], and $\emptyset_c$ is the transport-dependent percolation threshold. The values of $\emptyset^E$ and $\emptyset$ determined experimentally are then used to fit $\emptyset_c$ as follows:

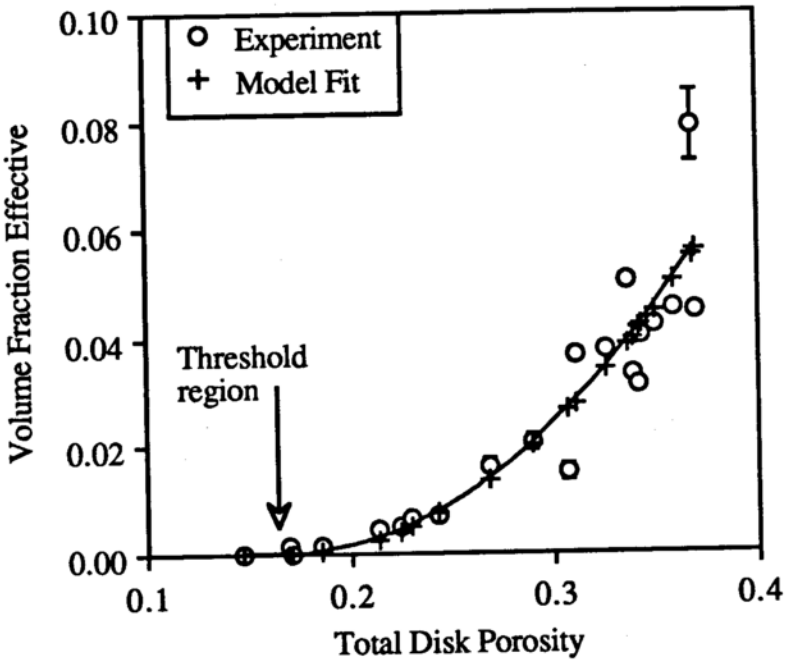

Figure 4.14. Volume fraction effective ($Ø^E$) data, slurry mixed disks. Line represents fit of scaling law for $Ø^E$ using total porosities shown. (Data from Table 4.8.)

Table 4.8. Volume fraction effective data, Stokes diaphragm cell results, slurry mixed disks.

Fired Porosity	Volume Fraction Effective[a]	Firing Time/hrs[b]
0.147[c]	0.000 (0.000)	4
0.170[c]	0.001 (0.000)	4
0.171	0.000 (0.000)	24
0.185	0.002 (0.000)	4
0.213	0.004 (0.000)	12
0.224	0.005 (0.000)	4
0.229	0.006 (0.001)	12
0.243	0.007 (0.000)	8
0.267	0.016 (0.001)	4
0.289	0.021 (0.002)	8
0.307	0.015 (0.002)	2
0.310	0.037 (0.001)	2
0.326	0.038 (0.001)	2
0.336	0.050 (0.001)	1
0.338	0.034 (0.000)	2
0.342	0.031 (0.000)	1
0.343	0.040 (0.000)	2
0.349	0.042 (0.001)	1
0.359	0.046 (0.000)	2
0.368	0.079 (0.007)	1
0.369	0.045 (0.001)	1

[a]Values in parentheses represent standard error of linear regression fit.

[b]Compaction pressure 10,000 psi, sintering temperature 1670°C.

[c]5% ($^{w}/_{w}$) PVP disks; all others 10% ($^{w}/_{w}$) PVP disks.

$$\varnothing^E = b\,(\varnothing - \varnothing_c)^{2.0} \;; \qquad (4.5)$$

where b is a pre-exponential factor. Nonlinear regression fitting of equation (4.5) yields the following parameters:

$$\varnothing_c = 0.169 \pm 0.02 \;;$$

$$b = 1.40 \pm 0.32 \;.$$

This value of $\varnothing_c$ is substantially higher than that obtained from volume fraction accessible data.

Model values of $\varnothing^E$ for the experimental total porosities shown in Figure 4.14 can be calculated from equation (4.5). These values are also plotted in Figure 4.14, for comparison to the experimental results. The model profile fits the data well up to a total porosity of about 0.350, but some deviation seems to be manifest at higher porosities. Nonetheless, the range of application of the $\varnothing^E$ model is larger than that of the $\varnothing^A$ model.

A plot of the volume fraction effective versus firing time is shown in Figure 4.15. In a fashion analogous to the behavior of the total porosity, the value of $\varnothing^E$ drops off drastically at short firing times, indicating that the large decrease in total porosity during initial stages of sintering also affects the value of $\varnothing^E$.

Equation (4.5) may thus be successfully applied to modeling of transport near the percolation threshold on the infinite lattice. It is also instructive to see what happens when the infinite lattice assumption breaks down, which is the subject of the remainder of this section.

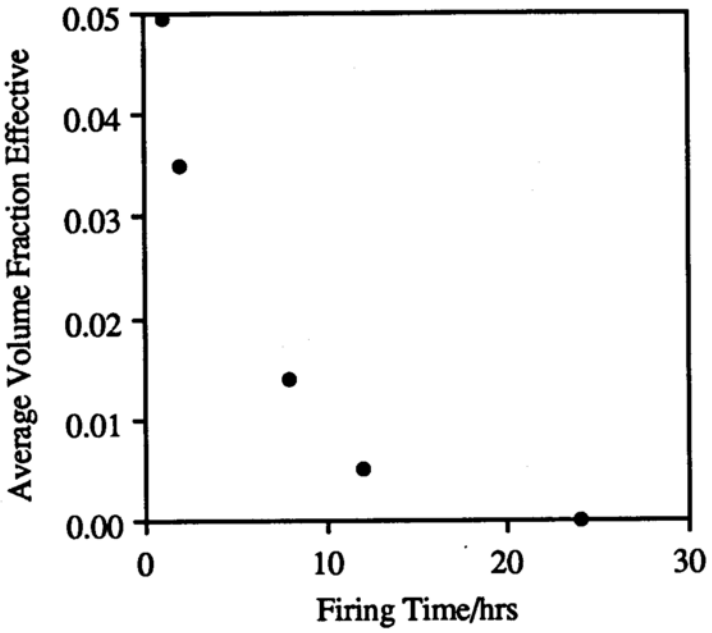

Figure 4.15. Relationship of $Ø^E$ to disk firing time.
(Data from Table 4.8.)

2. FINITE-SIZE SCALING

Finite-size scaling is possible in any system in which the pore diameter is the same order of magnitude as the linear thickness of the disk. Such a system will exhibit transport that is anomalously high as compared to that expected on the infinite lattice. This effect can only be seen near (i.e. within ± 10% of) the percolation threshold, because it will be swamped out at higher porosities. The percolation threshold obtained for the infinite lattice is also assumed to hold in a finite-size system for the purposes of modeling, but $\emptyset^E$ will not necessarily be equal to zero at this threshold.

An increase in the experimental value of $\emptyset^E$ above the value that would be expected on the infinite lattice for a given total porosity is an indication of finite-size scaling. Also, making disks with a range of pore bulb sizes, while maintaining the total disk porosity constant, should cause the value of $\emptyset^E$ to increase with increasing bulb diameter if such scaling has occurred. In this study, finite-size scaling was implemented by using polymer microspheres that, after burn-out, left large pore bulbs in the disk structure. The total disk porosity was held approximately constant by varying the sphere concentration in accordance with the sphere diameter. In this manner, the bulb diameter could be increased without increasing the total disk porosity. A slight increase in total porosity with increasing sphere diameter was observed for the series of diameters studied, but this was assumed not to be significant compared to the effect of changing bulb volume.

Transport studies to determine $\emptyset^E$ were performed on disks made from the four powders listed in Table 2.2(b) and were fired at 1670°C for 4 hours. Shrinkage during disk firing of the bulbous voids left by the spheres after burn-out was assumed to be about 31% of initial volume, based on results outlined in Chapter III for shrinkage of 5% PVP slurry mixed polydisperse disks. After firing, the number of bulb diameters (after shrinkage) required to cross the linear thickness of each disk was calculated, and denoted

as L.

It is important to note that L is determined using the bulb diameter, even though it has been argued that the pore throat diameter controls perfusion of the pore structure by solvent. This discrepancy may be justified by the observation that transport of a single benzoic acid molecule is not influenced by the size of an individual pore. Thus, mass flux of solute in either an infinite or a finite-sized disk depends on the total pore volume and the tortuosity of this volume, and not on the diameter of a pore throat. Since a small pore will (generally) be more tortuous than a large pore, if most of the pore volume is concentrated in one large pore rather than in several small pores the degree of tortuosity of the pore will be lower, resulting in a higher diffusion coefficient of solute through that pore. The infinite lattice approximation, as well as the finite-size assumption, should both thus be valid regardless of whether the throat or bulb diameter is used to determine L.

Transport studies to determine D_B were performed in Stokes diaphragm cells as before, and estimates of $\emptyset^E$ were calculated from these D_B values using equation (1.12). Values of $\emptyset^E$ for the four disks studied are shown in Figure 4.16 as functions of the system length L. $\emptyset^E$ decreases rapidly with increasing system length at first, and then levels off somewhat. Eventually, as L approaches infinity, $\emptyset^E$ will assume its limiting value for the infinite lattice.

The correction discussed in Chapter I to the volume fraction effective scaling law appears as follows:

$$\emptyset^E \propto L^{-\mu/\nu} \Phi\left[(\emptyset - \emptyset_c) L^{1/\nu}\right] ; \qquad (1.15)$$

where ν is the universal correlation length exponent assumed to equal 0.9[69], and $\emptyset_c$ is the percolation threshold obtained from volume fraction effective data on the infinite lattice. A

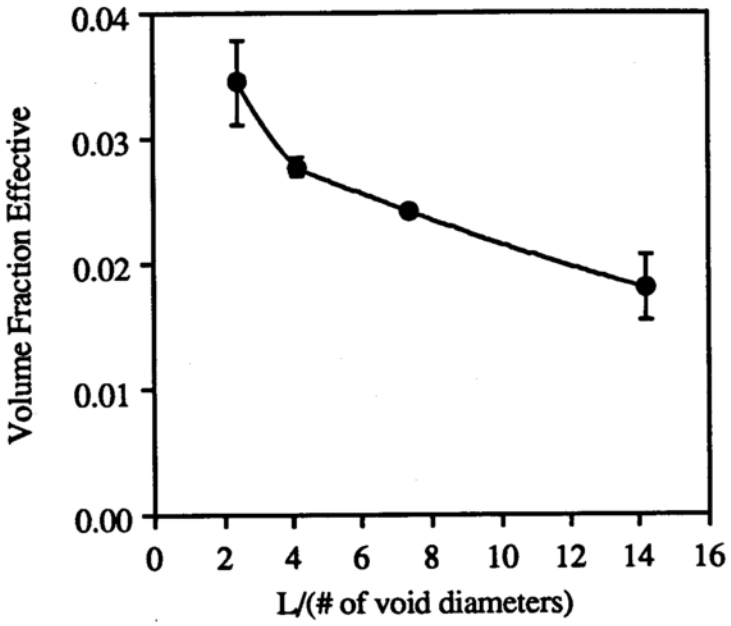

Figure 4.16. Finite-size scaling study, dependence of $\emptyset^E$ on system length.
(Data from Table 4.9.)

Table 4.9. Finite-size scaling study, Stokes diaphragm cell results, slurry mixed disks. Values in parentheses represent standard error of linear regression fit.

Fired Porosity[a]	Fired Void Diameter/μm[b]	System Length (L)/ (voids per disk)[c]	Volume Fraction Effective
0.178	121	14.170	0.018 (0.003)
0.185	250	7.359	0.024 (0.000)
0.188	415	4.195	0.028 (0.001)
0.190	685	2.468	0.034 (0.003)

[a]Compaction pressure 10,000 psi, firing time 12 hours, firing temperature 1670°C.

[b]Void diameter due to spheres, taking volume shrinkage (30%) into account.

[c]Linear thickness of disk divided by number of voids required to cross that thickness.

plot of $y = \Phi^E(L^{\mu/\nu})$ versus $z = (\Phi - \Phi_c)L^{1/\nu}$ can be used to estimate the form of the function $\Phi(\Phi,L)$, as outlined by Pandey et al.[39]. This plot appears in Figure 4.17, which indicates that y appears to increase exponentially with increasing z. Thus, the dependence of Φ^E on total porosity and system length may be postulated as follows:

$$\Phi^E \propto L^{-\mu/\nu} \exp\left[(\Phi - \Phi_c) L^{1/\nu}\right] . \qquad (4.6)$$

At the limit of $\Phi \rightarrow \Phi_c$, the exponential becomes equal to one, at which point $\Phi^E \propto L^{-\mu/\nu}$ as demonstrated by Pandey et al. and others[38,40]. Variation of L by computer simulation at this limit is the method commonly used to obtain an estimate of μ. Equation (4.6) is not valid in the case of $L \rightarrow \infty$, because the exponential becomes infinite.

This study has successfully shown that transport through disks of constant total porosity may be increased, by redistributing the pore volume from many small pores into a few large pores, without altering the random distribution of the pore space required to apply percolation theory. In a real delivery device, finite-size scaling behavior may be used to advantage as a means of increasing the release rate of a molecule without increasing the total device porosity. Greater release rates may thus be achieved without sacrificing mechanical strength for higher device porosity.

D. Comparison of Percolation Thresholds

The percolation threshold obtained from volume fraction accessible data was 0.129, and that obtained from volume fraction effective data was 0.169. These thresholds give coordination numbers (z) of 19 and 14, respectively. A z value of 14 is exactly that expected for a tetrakaidecahedral lattice. Comparison between these substantially different percolation thresholds can yield insight into the manner in which the microstructure

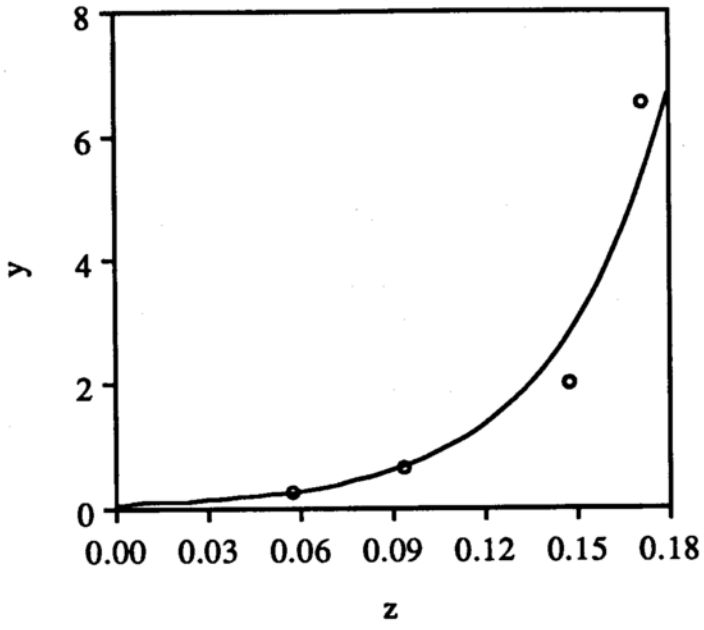

Figure 4.17. Finite-size scaling study, plot of $y = \emptyset^{E}(L^{\mu/\nu})$ vs. $z = (\emptyset-\emptyset_c)L^{1/\nu}$.
(Used to determine form of scaling function Φ in equation (1.15).)
(Data from Table 4.10.)

Table 4.10. Finite-size scaling study, quantities for use with Figure 4.17. Values in parentheses represent standard error of linear regression fit.

Volume Fraction Effective	$\emptyset - \emptyset_c /$ ($\emptyset_c = 0.169$)[a,b]	$\emptyset^E L^{\mu/\nu}$ (ordinate)[c]	$(\emptyset - \emptyset_c) L^{1/\nu}$ (abscissa)
0.018 (0.003)	121	14.170	0.018 (0.003)
0.024 (0.000)	250	7.359	0.024 (0.000)
0.028 (0.001)	415	4.195	0.028 (0.001)
0.034 (0.003)	685	2.468	0.034 (0.003)

[a]Value of $\emptyset_c$ obtained by nonlinear regression using data in Table E.8.

[b]$\emptyset$ = total disk porosity.

[c]Universal exponents used: $\mu = 2.0$, $\nu = 0.9$.

governs transport. The critical percolation threshold that is determined by study of molecular transport may reflect the amount of the sample-spanning pore space accessible to the solvent, and thus will not necessarily equal the true threshold porosity found through structural studies using helium pycnometry but may be analogous to one that would be obtained by aqueous pycnometry.

Volume fraction accessible data are assumed to be completely independent of the shape of the pore space, since flow of helium is not influenced by pore throats. Thus, the helium pycnometry method can access all portions of a sample-spanning cluster, no matter how tortuous or constricted this cluster may be. Conversely, perfusion of the pore space through filling by gravity-driven flow of an aqueous solvent (the method that is used to fill the disks used in the Stokes diaphragm cells prior to experiment) will result in only those pores being filled that exhibit the least tortuous pathways through the disk. Backbone pores that wind back on themselves may then be left empty of solvent, with the effect that not all of the pore space will be available for transport. A higher observed percolation threshold will thus result.

On the other hand, the value of $\emptyset_c = 0.169$ is exactly that predicted by Jerauld et al.[38] from computer simulation of transport on the tetrakaidecahedral lattice, which suggests that the tetrakaidecahedral lattice approximation is a valid description of the pore structure "seen" by a diffusing molecule. Thus, it is possible that the discrepancy between the two observed thresholds in this work is simply due to the different mechanisms involved in filling the pore space with helium versus transporting a molecule through it. This is a more plausible argument than the one given above because, as discussed in terms of aqueous pycnometry, dead-ends and small throats should not be prevalent enough near the threshold to significantly influence solvent uptake. A way of testing this hypothesis will be presented in the next chapter.

Overall, the studies outlined in this chapter have shown that the morphological and transport properties of the porous alumina disks made in this work may be successfully modeled using percolation theory. Some general conclusions based on these studies, and some suggestions for future work in lieu of these results, will be presented in Chapter V.

V. CONCLUSIONS AND SUGGESTIONS

This chapter summarizes the results discussed in Chapters III and IV, and outlines some conclusions based on these results regarding use of the material and application of the modeling technique. Some suggestions regarding future studies that can be undertaken to further define both the ceramic microstructure and the percolation model are also presented to close the thesis.

A. Production of Porous Ceramics

Polydisperse aluminum oxide was determined to be an ideal material for use in manufacturing devices of controlled porosity and low shrinkage. Firing temperature and powder polydispersity were found to be the variables exerting the greatest control over the final porosity of a ceramic disk, since the total porosity of the device could be decreased most easily by either raising the temperature or decreasing the polydispersity (while maintaining a small average particle size) of the powder. Compaction pressure, percent binder used, firing time, and heating rate were seen to have less pronounced effects on porosity and shrinkage. Firing time was used in this work to control the final porosity, because the range of firing temperatures (1450°C and above) over which the porosity of the polydisperse material could be varied was too high to effectively manipulate using the equipment available.

Total porosities of 15% to 40% could be easily obtained and reproduced using the polydisperse powder, while very low porosities (4% to 10%) could only be achieved by using a monodisperse (0.5 μm diameter) powder. Thus, it may be seen from this work that some degree of polydispersity in the ceramic powder is needed to retain a significant pore size and amount of void space in the final device. It is important to note that the

observed behavior is pertinent to monodisperse and polydisperse powders of moderate sizes only, as very small polydisperse powder compacts could exhibit a very large amount of shrinkage and very large monodisperse powder compacts could shrink very little.

As the void space in a fired ceramic device increases, its mechanical strength decreases drastically[70]. The disks made in this work, while not presumed to be as strong as completely nonporous disks of similar size, are anticipated to be sufficiently resistant to mechanical breakage for use in the body. Nonetheless, characterizing both compressive and shear strengths of a porous disk should be an important next phase in this research scheme. An implanted ceramic delivery device must be able to withstand a certain amount of shock, so that it does not break and release its contents into the body in one giant dose when subjected to external stress.

B. The Percolation Theory Model

1. The Infinite Lattice

The percolation theory approach was found to successfully approximate the pore structure and transport properties of ceramic disks for total porosities near the percolation threshold. The scaling law for volume fraction effective ($\emptyset^E$), using a universal exponent of $\mu = 2.0$, was found to successfully represent the relationship between $\emptyset^E$ and total disk porosity up to a total porosity of about 30%. The scaling law for volume fraction accessible ($\emptyset^A$), however, did not fit the experimental values of $\emptyset^A$ very well at any total porosity if the universal exponent of $\beta = 0.4$ was used.

In the case of $\emptyset^E$, deviations from the model at higher total porosities were thought to occur as individual pores became less important in their contributions to transport, because the tortuosity of each individual pore decreases as the total porosity increases, resulting in accelerated transport through the disk. Porosities near the threshold thus appeared to offer

the greatest control over transport of small molecules, as is desired for manipulation of drug release, so in this respect the percolation theory model is very useful for description of transport in the system studied in this work.

On the other hand, the reason for deviation of the $\emptyset^A$ model from the experimental values of $\emptyset^A$ at all porosities is not known. The use of a different universal exponent than $\beta = 0.4$ may result in a better fit of the experimental data, but no suggestion exists in the literature of a different exponent to try. The $\emptyset^A$ data obtained in this work were not used to arrive at a new value of β, because determination of β requires information regarding the cluster size distribution at the percolation threshold that is not necessarily contained in the relation between $\emptyset$ and $\emptyset^A$. Rather, β must be found by computer simulation of the pore structure at the threshold. A possible way to estimate β will be discussed shortly.

The percolation thresholds found by morphological analysis ($\emptyset_c = 0.129$) and transport study ($\emptyset_c = 0.169$) differ substantially. Two possibilities for this disagreement are incomplete filling of sample-spanning pores by the liquid solvent used in transport, or alternatively a fundamental deficiency in the model used to describe the morphology. Because the backbone porosity is that fraction of the accessible porosity thought to be used in transport at steady-state, and also because this backbone should consist of the largest and least tortuous pores in the accessible cluster, it is reasonable to assume that the entire backbone cluster is filled with liquid. Thus, incomplete filling is not expected to affect transport, so $\emptyset_c = 0.169$ may be taken as the correct threshold for the transport model. The difference in observed thresholds indicates that the pore structure reflected by the transport scaling law is not the same as that reflected by the morphological scaling law, an argument that may also explain the poor fit of the morphological scaling law. This is an important subject for further study, so possible methods of solving this problem will be discussed shortly.

The primary strength of the transport model is that it does not require explicit use of a tortuosity "fudge factor" as is commonly employed in the description of diffusion through porous systems. Rather, the tortuosity of the system is implicit in the observed volume fractions and the percolation threshold, through the coordination number (z) of the system. The higher the value of z, the more complicated the system, and thus the more tortuous the pore structure.

The coordination numbers corresponding to morphological and transport thresholds were found to be 19 and 14, respectively, using equation (1.4). The pore space used in transport appears to follow the tetrakaidecahedral lattice approximation ($z = 14$), but morphological results indicate that helium pycnometry accesses a more complicated pore structure. This is a reasonable assumption, since helium is thought to enter dead-end pores and other small void spaces that liquid (such as used in aqueous pycnometry or the diffusion study) cannot enter. The "transport lattice" that governs the volume fraction effective scaling law is thus a less-complicated subset of the "true" lattice described by the volume fraction accessible. Although the average structure of the solid portion of the ceramic matrix has been shown to be approximated by the tetrakaidecahedron, the pore space that surrounds the solid structure may be more complex.

Mercury porosimetry and scanning electron microscopy were found to be of some use in developing an understanding of the real system that was being modeled by percolation theory. However, they were not very important in developing the models themselves, which do not rely on detailed knowledge of the microstructure for their construction. The primary purpose of these techniques in future work should simply be in elucidating a clear picture of the system under study. Some modifications to the porosimetry model that may make it more attractive for use in describing the pore structure will be considered shortly.

2. Finite-Size Scaling

Finite-size scaling results showed that the void space could be redistributed and consolidated, without significantly affecting the total porosity, in order to increase the transport rate of benzoic acid through the disk. Thus, this may be a useful means of manipulating the release rate of a ceramic device while simultaneously taking advantage of the added strength imparted by low porosity. It appears that an exponential relationship exists between the quantity $(\emptyset-\emptyset_c)L^{1/\nu}$ and the value $\emptyset^E L^{\mu/\nu}$, with the latter increasing in magnitude as L increases toward a value above which the infinite lattice approximation can be applied.

C. Suggestions for Continued Work

Some ideas as to further experiments that should be undertaken to complete the percolation theory models investigated in this work may be given in order to close this thesis. Aside from determination of mechanical strength, no other work regarding characterization of the ceramic material itself is needed at this point.

1. Alternate Methods of Volume Fraction Effective Estimation

Other methods besides diffusivity estimation may be used to determine the value of $\emptyset^E$. This section considers two such methods, namely electrical conductivity of a liquid-filled pore structure, and permeability of the pore structure to a gas or liquid stream.

a) Conductivity

The most common experimental means of obtaining volume fraction effective information is by measuring electrical conductivity across a composite system. The system may consist of a mixture of conducting and nonconducting solids[44,71], or may alternatively

be a porous nonconducting solid perfused with an aqueous electrolyte solution[45,46]. The conductivity as a function of percent conductor or of total porosity is used to find the critical percolation threshold of the system in the same manner as the bulk diffusivity (D_B) previously discussed.

Alumina is a good insulating material at room temperature. Thus, it should be possible to estimate $\emptyset^E$ and $\emptyset_c$ in a porous alumina ceramic by perfusing with electrolyte and measuring the solution conductivity. Other authors[45,46] have used such a system to obtain $\emptyset_c$, and have observed no percolation threshold (i.e. the conductivity of the system appeared to be finite above a total porosity of zero), suggesting that the pore space in an alumina ceramic is connected even at very low porosities. Unfortunately, the lowest total porosity system these authors investigated was $\emptyset = 0.179$, so their assertion that $\emptyset_c = 0$ is not based on experimental data. These authors do not show whether their data extrapolate to $\emptyset_c = 0$.

It is important to determine the conductivity as a function of total porosity for the devices made in this work so that comparisons may be made to conductivity studies appearing in the literature, since no published results exist that may be correlated with the diffusivity data obtained here. The only drawback to such a study is the same as that encountered in aqueous pycnometry, involving the complete perfusion of all pores of the device with electrolyte. Introduction of electrolyte to a chamber in which the device is contained under high vacuum, so that no capillary pressure exists in the dead-end pore space to hinder liquid uptake, is a possible way to avoid this problem.

Comparison between percolation thresholds obtained by diffusivity and conductivity methods can be performed to develop an idea of the pathways used in electron flow versus those used in molecular transport. Little difference is expected between thresholds obtained from these two methods, unless some degree of dielectric breakdown occurs in the ceramic

at high current flow.

b) Gas and Liquid Permeability

Another approach that may be taken in estimation of the effective volume fraction is that of flow-through permeametry, wherein the pressure drop of a gas or liquid stream across a disk mounted in a flow cell is taken as a reflection of the porosity available for bulk flow through the disk. The porosity and pressure drop are inversely related in such a system. At steady-state, the flow will take place predominantly in those sample-spanning pores with the lowest tortuosity, resulting in an effective volume fraction that should be analogous to that obtained from diffusivity or conductivity measurements. Care must be taken to ensure that the flow rate is not so high as to cause the fluid stream to pass by some pores that would otherwise be entered if the flow rate were lower. This method, along with the conductivity technique, offers the advantage of speed over the diffusivity estimation method used in this work, which was found to be very slow and prone to error. Nonetheless, conductivity and permeability are only suggested for use as checks on the data obtained by diffusivity, since the molecular transport study will best approximate the actual transport properties of a real release device.

2. VOLUME FRACTION BACKBONE ESTIMATION

Knowledge of the backbone volume fraction ($\emptyset^B$) is useful for modeling of the accessible volume fraction that is occupied in steady-state transport. Since $\emptyset^B$ is a property of the pore structure and not a transport property, even though transport may occur only in the backbone the results obtained by transport studies cannot be directly applied to estimation of the backbone size. The value of $\emptyset_c$ determined for a transport system may be used in the scaling relationship for $\emptyset^B$,

$$\emptyset^B = \alpha (\emptyset - \emptyset_c)^{\gamma_B} \; ; \qquad (5.1)$$

if the assumption is made that the entire backbone pore space is available for transport (for example, if it is true that all sample-spanning pores have been filled with electrolyte). This assumption is reasonable if, as has been argued, the low value of $\emptyset_c$ obtained by volume fraction accessible data is a result of small dead-end pores that do not contribute to transport. Unfortunately, the pre-exponential factor α cannot be determined simply from knowledge of $\emptyset$, $\emptyset_c$, and γ_B (the universal exponent for the backbone), so $\emptyset^B$ cannot be found from the data obtained in this work.

It should be possible to estimate the value of $\emptyset^B$ by assuming that the volume fraction accessible to gas in a permeability experiment is approximately equal to the true backbone volume fraction. Study of the observed volume fraction as a function of the gas flow rate may be used to determine that flow rate high enough to bypass the dead-end pores, but low enough to access the more tortuous sample-spanning pores. This flow rate will then give the best estimate of $\emptyset^B$. Also, the difference between the volume fraction accessible ($\emptyset^A$) obtained by helium pycnometry and the value of $\emptyset^B$ will yield an estimate of the fraction of $\emptyset^A$ that consists of dead-end pore space.

3. Mercury Porosimetry

As discussed in Chapter IV, the pore size information resulting from a mercury porosimetry experiment is of limited use because it only reflects the sizes of the pore throats and not the pore bulbs. Some additional information may be obtained from a porosimetry run by, in addition to analyzing the volume change of mercury during intrusion, recording the increase in volume observed due to lowering of the pressure in the sample cell.

Mercury that has entered the sample during intrusion is drawn out when the pressure is lowered, and the rate at which mercury leaves the sample reflects the volumes of the pore bulbs (because they will act as reservoirs and slow the emptying process). This sort of intrusion-extrusion experiment produces a hysteresis curve, where the upper (intrusion) profile shows the rate at which mercury invades the sample, and the lower (extrusion) curve indicates the rate at which mercury escapes the sample. The difference between these two curves reflects the contribution of bulb size to uptake of mercury, but is not generally a good indication of the actual bulb volume since it cannot be assumed that mercury has completely filled all bulbs during intrusion.

Alternatively, it may be possible to use a different model to analyze the $^{dV}/_{d(\log p)}$ data in order to obtain some estimate of the bulb size. Other models are available[72] that attempt to account for the nonuniform sizes of pores by using distribution functions to build a range of pore diameters into the solution. Although these models use the same data as the cylindrical pore model to arrive at their conclusions, they are not as straightforward to use. It does not appear that mercury porosimetry is crucial to the development of models for drug delivery through porous ceramics, so not too much should be made of this particular method of analysis. Rather, computer simulation of the predicted pore morphology is thought to be more useful in understanding the properties of the ceramic structure.

4. PORE STRUCTURE MODELING

Computer simulation of the pore structure is a useful means of obtaining a better idea of the true influence of the microstructure on the scaling relationships. Also, such modeling can be employed to directly estimate the values of the universal exponents μ and β in order to produce better fits to these scaling laws. Two methods of simulating the pore structure are outlined next.

a) Randomly-Stacked Plates

As noted previously, the ceramic grain structure inside a disk appears to be better approximated by a system of randomly-stacked plates than by groups of tetrakaidecahedra. Determination of the average coordination number of the plate system may result in a calculated threshold which more closely matches the fit from volume fraction accessible data. It may be possible to model the system by using a fractal approach[46] to obtain an average spatial dimension more representative of the pore structure than is the case if the structure is simply assumed to be three-dimensional. Also, since $\beta = 0.4$ is true in three dimensions only, a fractal dimension may yield a better value of β for use in fitting the volume fraction accessible data.

b) The Mixed Site-Bond Model

A recent development in the modeling of random pore structures is the mixed site-bond model[32], in which the ability of an ant to travel between two sites is influenced by the size of the bond between them. In other words, it is easier for the ant to travel from site A to site B than from site A to site C if the bond between A and B is larger than the bond between A and C. A structure such as this is simulated by fixing the sites at one size and allowing the sizes of the bonds to vary at random. The resulting system possess properties that fall between those of bond-only and site-only models, depending on the sizes of the bonds.

An approximation such as the site-bond model could possibly explain the low critical percolation threshold observed in volume fraction accessible studies, because it may account for the contribution of very small dead-end pore volume to the sample-spanning cluster. Any Monte Carlo simulation of this structure could use the accessible data already

obtained in this work. Also, this method may be used to obtain a value of β more representative of the experimental $\emptyset^A$ data.

In closing, this work has successfully shown that transport of small molecules through ceramic disks of controlled porosity can be modeled using the technique of percolation theory, and that such transport can be manipulated through modification of both the total void space and its distribution within the disk.

APPENDIX A. HELIUM PYCNOMETRY DERIVATIONS

1. Derivation of Sample Volume from Helium Pycnometry

Let: p_1 = reference cell pressure (psi);

p_2 = (reference cell + sample cell) pressure (psi);

V_{ref} = reference cell volume (cm^3);

V_{cell} = sample cell volume (cm^3);

Vs = sample volume (cm^3).

Use the ideal gas law as given in equation (A1.1):

$$p\,V = n\,R\,T\ ; \tag{A1.1}$$

where n, R, and T are constant.

With a sample in the micro cell, equation (A1.2) is used:

$$p_1\,V_{ref} = n\,R\,T = p_2\,(V_{ref} + V_{cell} - V_s)\ . \tag{A1.2}$$

Solve equation (A1.2) for V_s as follows to obtain equation (2.5):

$$\frac{p_1}{p_2}\,V_{ref} = (V_{ref} + V_{cell} - V_s)\ ;$$

$$V_{ref}\left(\frac{p_1}{p_2} - 1\right) = V_{cell} - V_s\ ;$$

$$V_s = V_{cell} - V_{ref}\left(\frac{p_1}{p_2} - 1\right)\ . \tag{2.5}$$

2. Derivation of Expression for Volume Fraction Isolated

Let: V_s = sample volume (cm^3), (from equation (2.5));

V_{solid} = total volume of solid in sample (cm^3);

V^I = total volume of isolated pore space in sample (cm^3);

M_{bulk} = weight of sample (g), (assumed equal to weight of solid)

V_{bulk} = bulk volume of disk sample (cm^3), (= V_t);

ρ_{bulk} = bulk density of disk sample (g/cm^3);

ρ_{theor} = theoretical density of aluminum oxide (g/cm^3).

Define V_s as the sum of V_{solid} and V^I:

$$V_s = V_{solid} + V^I \ . \qquad \text{(A2.1)}$$

Redefine V_{solid} in terms of measureable quantities:

$$V_{solid} = \frac{M_{bulk}}{\rho_{theor}} = V_{bulk} \frac{\rho_{bulk}}{\rho_{theor}} \ . \qquad \text{(A2.2)}$$

Rearrange equation (A2.1) to solve for V^I in terms of V_s and V_{solid}:

$$V^I = V_s - V_{bulk} \frac{\rho_{bulk}}{\rho_{theor}} \ . \qquad \text{(A2.3)}$$

The volume fraction isolated ($\emptyset^I$) may be defined as in equation (A2.4):

$$\emptyset^I = \frac{V^I}{V_{bulk}} \ . \qquad \text{(A2.4)}$$

Substitute equation (A2.3) into equation (A2.4) to obtain equation (A2.5):

$$\emptyset^I = \frac{V_s}{V_{bulk}} - \frac{\rho_{bulk}}{\rho_{theor}} \quad . \qquad \text{(A2.5)}$$

The total porosity may be defined as follows:

$$\emptyset = 1 - \frac{\rho_{bulk}}{\rho_{theor}} \quad . \qquad \text{(2.2)}$$

Substitute equation (2.2) into equation (A2.5) to obtain the expression for volume fraction effective, equation (2.6):

$$\emptyset^I = \frac{V_s}{V_{bulk}} - (1 - \emptyset) \quad . \qquad \text{(2.6)}$$

APPENDIX B. DERIVATION OF THE MEMBRANE TRANSPORT MODEL USED WITH THE STOKES DIAPHRAGM CELL

Define Fick's first law of steady-state diffusion as follows[73]:

$$j_1 = - D_B \frac{dC}{dx} \; ; \qquad \text{(B.1)}$$

where j_1 is the mass flux across the membrane at position x, and D_B is the bulk diffusion coefficient of solute in the membrane in $^{cm^2}/_{sec}$.

Apply the pseudosteady-state approximation, which assumes that the concentration gradient is linear with respect to position in the membrane, to equation (B.1) to re-define the flux:

$$j_1 = \frac{D_B}{l}(C_1 - C_2) \; ; \qquad \text{(B.2)}$$

where l is the thickness of the membrane (cm), C_1 is the concentration of solute in the donor compartment ($^g/_{cm^3}$), and C_2 is the concentration of solute in the receptor compartment ($^g/_{cm^3}$).

Define the change in solute concentration in each cell at steady-state:

$$V_1 \frac{dC_1}{dt} = - A_{cs} j_1 \; ; \qquad \text{(B.3a)}$$

$$V_2 \frac{dC_2}{dt} = A_{cs} j_1 \; ; \qquad \text{(B.3b)}$$

where A_{cs} is the surface area of the membrane available for diffusion (cm^2), V_1 is the

donor compartment volume (cm^3), and V_2 is the receptor compartment volume (cm^3). Note that j_1 is negative in equation (B.3a) since solute is escaping from the donor cell.

Next, subtract equation (B.3a) from (B.3b) and equate the result with equation (B.2) to obtain equation (B.4):

$$\frac{d}{dt}(C_1 - C_2) = D_B \beta (C_2 - C_1) \; ; \qquad (B.4)$$

where β is a geometric constant (cm^{-2}), as follows:

$$\beta = \frac{A_{cs}}{l}\left(\frac{1}{V_1} + \frac{1}{V_2}\right) .$$

Equation (B.4) is subject to the following initial condition:

$$@\ t = 0,\ C_1 - C_2 = C_1^0 - C_2^0 .$$

Usually, $C_2^0 = 0$ at $t = 0$. Solving equation (B.4) and applying this initial condition results in equation (2.10) after solving for D_B:

$$D_B = \frac{1}{\beta t} \ln\left[\frac{(C_1 - C_2)^0}{(C_1 - C_2)^t}\right] . \qquad (2.10)$$

Note that C_{bottom} is analogous to C_1, and C_{top} is analogous to C_2 in the form of the equation appearing in Chapter II.

APPENDIX C. THE TAYLOR DISPERSION APPARATUS

Equations (2.12a) and (2.12b) were used to obtain the aqueous diffusivity of ionized benzoic acid:

$$c = \frac{M}{A_{cs}\sqrt{4\pi E_z t}} \exp\left[\frac{-(z - v_0 t)^2}{4 E_z t}\right]; \qquad (2.12a)$$

$$E_z = \frac{(R_0 v^0)^2}{48 D}; \qquad (2.12b)$$

where the terms may be defined as follows:

c = concentration of solute at maximum of dispersion profile (g/cm^3);

M = total mass of solute in sample = 4.98×10^{-6} g;

A_{cs} = cross-sectional area of dispersion tube 2.48×10^{-4} cm^2;

E_z = dispersion coefficient (cm^2/s);

z = length of dispersion tube = 457.2 cm;

v_0 = maximum velocity during laminar flow = 6.72 cm/s;

t = time to reach concentration c (sec);

R_0 = radius of dispersion tube = 8.89×10^{-3} cm;

D = diffusion coefficient of solute (cm^2/s).

Complete derivations of the above equations may be found elsewhere[74].

Using the above constant values in equation (2.12a), the simplified form may be obtained as shown in equation (C.1):

$$c = \frac{.005659}{\sqrt{E_z t}} \exp\left[-\frac{(457.2 - 6.72 t)^2}{4 E_z t}\right]. \qquad (C.1)$$

Determination of c as a function of t allows for solution of E_z.

The reduced form of equation (C.1) may be given as equation (C.2):

$$0.2404 = \frac{1}{\sqrt{E_z}} \exp\left[-\frac{0.3917}{E_z}\right] . \qquad \text{(C.2)}$$

The following values were assumed for c and t:

$c = 1.1625 \times 10^{-4}$ g/cc;

t = 136.97 sec.

These values were obtained from an average of eleven dispersion curves obtained from the system shown in Figure C.1.

The exponential term in equation (C.2) is effectively equal to one, so E_z may be easily determined for use in equation (2.12b) to solve for D, which is given in Chapter II.

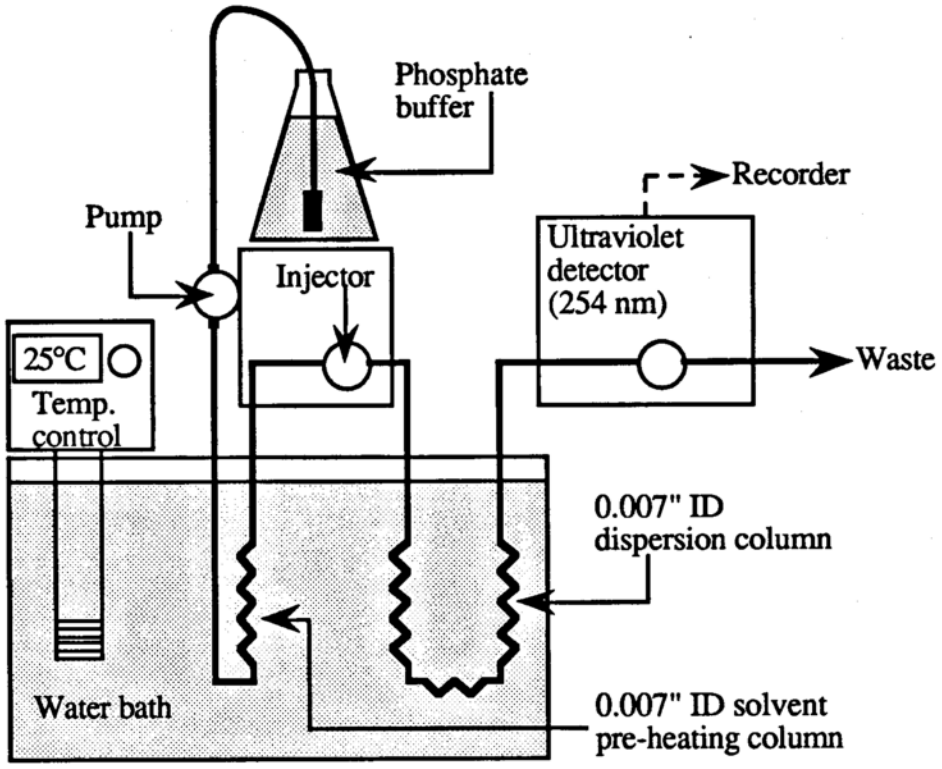

Figure C.1. Experimental Taylor Dispersion Apparatus.

REFERENCES

1. Kingery WD, Bowen HK, and Uhlmann DR, **Introduction to Ceramics**, 2nd Ed., John Wiley and Sons, Inc., New York (1976), p.21.

2. Anderson JC, Leaver KD, Rawlings RD, and Alexander JM, **Materials Science**, 3rd Ed., Van Nostrand Reinhold (UK) Co. Ltd. (1985), p.91.

3. Reference 2, pp.94-95.

4. Verhoeven JD, **Fundamentals of Physical Metallurgy**, John Wiley and Sons, Inc., New York (1975), p.133.

5. Reference 4, p.181.

6. Reference 4, p.198.

7. Reference 1, p.186.

8. Reference 1, p.450.

9. Siegel RA, and Langer R, "A new Monte Carlo approach to diffusion in constricted porous geometries", *J. Colloid Interface Sci.* **109** [2] 426-440 (1986).

10. Rice RW, "Ceramic processing: An overview", *AIChE J.* **36** [4] 481-510 (1990).

11. Van Vlack LH, **Physical Ceramics for Engineers**, Addison-Wesley Publishing Co., Reading, Massachusetts (1964), pp.227-277.

12. Ryshkewitch E, and Richerson DW, **Oxide Ceramics**, 2nd Ed., Academic Press, Inc., Orlando, Florida (1985), pp.12-68.

13. Davey RJ, and Dobbs B, "On the morphology of ceramic powders", *Chem. Eng. Sci.* **42** [4] 631-637 (1987).

14. Kendall K, "Influence of powder structure on processing and properties of advance ceramics", *Powder Technol.* **58** 151-161 (1989).

15. Cameron CP, and Raj R, "Grain-growth transition during sintering of colloidally prepared alumina powder compacts", *J. Am. Ceram. Soc.* **71** [12] 1031-1035 (1988).

16. Topolevsky R, and Caligaris RE, "Compaction behaviour of ceramic powders. Correlation functions between processing variables and fired properties", *Powder Technol.* **46** 215-218 (1986).

17. Reference 11, p.242.

18. Reference 1, p.469.

19. Reference 1, pp.474-476.

20. Kwon ST, Kim DY, Kang TK, and Yoon DN, "Effect of sintering temperature on the densification of Al_2O_3", *J. Am. Ceram. Soc.* **70** [4] c69-c70 (1987).

21. Evans AG, and Hsueh CH, "Behavior of large pores during sintering and hot isostatic pressing", *J. Am. Ceram. Soc.* **69** [6] 444-448 (1986).

22. Yeh T-S, and Sacks MD, "Effect of particle size distribution on the sintering of alumina", *J. Am. Ceram. Soc.* **71** [12] c484-c487 (1988).

23. Chappell JS, Ring TA, and Birchall JD, "Particle size distribution effects on sintering rates", *J. Appl. Phys.* **60** [1] 383-391 (1986).

24. Berry KA, and Harmer MP, "Effect of MgO solute on microstructure development in Al2O3", *J. Am. Ceram. Soc.* **69** [2] 143-148 (1986).

25. Shaw NJ, and Brook RJ, "Structure and grain coarsening during the sintering of alumina", *J. Am. Ceram. Soc.* **69** [2] 107-110 (1986).

26. Reference 12, p.119.

27. Robie RA, Hemingway BS, and Fisher JR, **Thermodynamic Properties of Minerals and Related Substances at 298.15 K and 1 Bar (105 Pascals) Pressure and at Higher Temperatures, Geological Survey Bulletin 1452,** US Government Printing Office, Washington DC (1978), p.137.

28. Weast RW Ed., **CRC Handbook of Chemistry and Physics,** 62nd Ed., CRC Press, Inc., Boca Raton, Florida (1981), p.E-58.

29. Reference 12, pp.109-256.

30. Essam JW, "Percolation theory", *Rep. Prog. Phys.* **43** 834-912 (1980).

31. Stauffer D, **Introduction to Percolation Theory,** Taylor and Francis Ltd., London (1985).

32. Yanuka M, "The mixed bond-site percolation problem and its application to capillary phenomena in porous media", *J. Colloid Interface Sci.* **134** [1] 198-205 (1990).

33. Mohanty KK, Ottino JM, and Davis HT, "Reaction and transport in disordered composite media: Introduction of percolation concepts", *Chem. Eng. Sci.* **37** [6] 905-924 (1982).

34. Grimmett G, **Percolation,** Springer-Verlag New York Inc. (1989), p.227.

35. Nagatani T, "A regular model for cluster numbers and structure just below percolation threshold", *J. Phys. A: Math. Gen.* **20** [4] 961-970 (1987).

36. Reyes S, and Jensen KF, "Estimation of effective transport coefficients in porous solids based on percolation concepts", *Chem. Eng. Sci.* **40** [9] 1723-1734 (1985).

37. Havlin S, Ben-Avraham D, and Sompolinsky H, "Scaling behavior of diffusion on percolation clusters", *Phys. Rev. A* **27** [3] 1730-1733 (1983).

38. Jerauld GR, Scriven LE, and Davis HT, "Percolation and conduction on the 3D Voronoi and regular networks: A second case study in topological disorder", *J. Phys. C: Solid State Phys.* **17** [19] 3429-3439 (1984).

39. Pandey RB, Stauffer D, Margolina A, and Zabolitzky JG, "Diffusion on random systems above, below, and at their percolation threshold in two and three dimensions", *J. Stat. Phys.* **34** [3/4] 427-449 (1984).

40. Sahimi M, Hughes BD, Scriven LE, and Davis HT, "Critical exponent of percolation conductivity by finite-size scaling", *J. Phys. C: Solid State Phys.* **16** L521-L527 (1983).

41. Margolina A, Nakanishi H, Stauffer D, and Stanley HE, "Monte Carlo and series study of corrections to scaling in two-dimensional percolation", *J. Phys. A: Math. Gen.* **17** [8] 1683-1701 (1984).

42. Larson RG, and Davis HT, "Conducting backbone in percolating Bethe lattices", *J. Phys. C: Solid State Phys.* **15** [11] 2327-2331 (1982).

43. Efros AL, **Physics and Geometry of Disorder**, Mir Publishers Moscow (1986), p.68.

44. Lee S-I, Song Y, Noh TW, Chen X-D, and Gaines JR, "Experimental observation of nonuniversal behavior of the conductivity exponent for three-dimensional continuum percolation systems", *Phys. Rev. B* **34** [10] 6719-6724 (1986).

45. Brouers F, and Ramsamugh A, "Relation between conductivity and fluid flow permeability in porous alumina ceramics", *Solid State Commun.* **60** (12) 951-953 (1986).

46. Brouers F, and Ramsamugh A, "Percolation and anomalous conduction on fractals in fluid-saturated porous media", *J. Phys. C: Solid State Phys.* **21** [9] 1839-1847 (1988).

47. Hastedt JE, and Wright JL, "Diffusion in porous materials above the percolation threshold", *Pharm. Res.*, in press.

48 Skwierczynski RD, **Characterization of Porous Hydroxyapatite and β-Whitlockite Ceramic Disks: An Application of Percolation Theory**, Master's Thesis, University of Wisconsin-Madison (1989).

49. Reference 4, p.199.

50. Hench LL, and Wilson J, "Surface-active biomaterials", *Science* Nov. 9, 630-636

(1984).

51. Lemons JE, and Lucas LC, "Properties of biomaterials", *J. Arthroplasty* **1** (2) 143-147 (1986).

52. Ducheyne P, and Hastings G, "The structure, properties, and functional behavior of biomaterials", in Ducheyne P, and Hastings G Eds., **Metal and Ceramic Biomaterials**, Vol. 1, CRC Press Inc., Boca Raton, Florida, pp.1-5 (1984).

53. Allan G, "Electronic structure of transition metal surfaces", in Dobrzynski L Ed., **Handbook of Surfaces and Interfaces**, Vol. 1, Garland STM Press, New York, pp.299-416 (1978).

54. Kasemo B, and Lausmaa J, "Surface science aspects on inorganic biomaterials", *CRC Critical Reviews in Biocompatibility* **2** (4) 335-380 (1986).

55. Adamson AW, **Physical Chemistry of Surfaces**, 4th Ed., John Wiley and Sons, New York, p.340 (1982).

56. Vander AJ, Sherman JH, and Luciano DS, **Human Physiology**, 3rd Ed., McGraw-Hill Inc., New York, pp.521-546 (1980).

57. Albrektsson T, and Albrektsson B, "Osseointegration of bone implants", *Acta Orthop. Scand.* **58** 567-587 (1987).

58. Boretos JW, "Bioceramics", *Chem. Tech.* April, 224-231 (1987).

59. Griss P, and Heimke G, "Biocompatibility of high density alumina and its application in orthopedic surgery", in Williams DF Ed., **Biocompatibility of Clinical Implant Materials**, CRC Press, Inc., Boca Raton, Florida (1981), pp.155-198.

60. Uchida A, Nade S, McCartney E, and Ching W, "Growth of bone marrow cells on porous ceramics in vitro", *J. Biomed. Mater. Res.* **21** 1-10 (1987).

61. Chien YW, **Novel Drug Delivery Systems**, Marcel Dekker, Inc., New York, pp.465-474 (1982).

62. Pennings ECM, and Grellner W, "Precise nondestructive determination of the density of porous ceramics", *J. Amer. Ceram. Soc.* **72** [7] 1268-1270 (1989).

63. Prewitt JM, "Comment on the characterization of porosity in PTFE-carbon composite implant materials by mercury porosimetry", *J. Biomed. Mater. Res.* **18** 123-125 (1984).

64. Cussler EL, **Diffusion: Mass Transport in Fluid Systems**, Cambridge University Press, New York (1986), pp.133-137.

65. Wickliffe B, and Entrekin DN, "Relation of pH to preservative effectiveness II", *J. Pharm. Sci.* **53** [7] 769-773 (1964).

66. Perry RH, and Chilton CH, **Chemical Engineer's Handbook**, 5th Ed., McGraw-Hill Book Co., New York (1973), p.3-235.

67. Reference 64, p.229.

68. Reference 64, pp.89-93.

69. Reference 31, p.52.

70. Reference 1, p.811.

71. Ezquerra TA, Mohammadi M, Kremer F, Vilgis T, and Wegner G, "On the percolative behaviour of polymeric insulator-conductor composites: Polyethylene oxide-polypyrrole", *J. Phys. C: Solid State Phys.* **21** [5] 927-941 (1988).

72. Lapidus GR, Lane AM, Ng KM, and Conner WC, "Interpretation of mercury porosimetry data using a pore-throat network model", *Chem. Eng. Commun.*, **38** 33-56 (1985).

73. Reference 64, pp.26-28.

74. Reference 64, pp.89-93.